A Rate-Pressure-Dependent Thermodynamically-Consistent Phase Field Model for the Description of Failure Patterns in Dynamic Brittle Fracture

Antonino Francesco Parrinello

Exeter College

University of Oxford

A thesis submitted for the degree of

Doctor of Philosophy

Hilary Term, 2017

"Only the educated are free"

cit. Epictetus

To Bartolo, Rita and Rossana

"The family is a heaven in a heartless world"

cit. Christopher Lasch

To the love of my life, Kristina – the persistent light of hope over the horizon, where my mind and my heart find their peace.

Their reason to exist.

"I've always believed in numbers, in equations, in logic and reason. But after a lifetime of such pursuits: I ask: What truly is logic? Who decides reason? My quest has taken me to the physical, the metaphysical, the delusional, and back. I have made the most important discovery of my career - the most important discovery of my life. It is only in the mysterious equations of love that any logic or reasons can be found.

I am only here today because of you."

John Nash, "A Beautiful Mind"

Acknowledgements

First and foremost, I would like to acknowledge the support and leadership provided by my supervisor, Prof. Nik Petrinic. His constant positivism and strive for science has motivated me to live my doctoral studies as a true life-embracing experience. To him I pay my gratitude for having put trust on me when I was chosen to be a new member of the Impact Engineering Laboratory. His constant guidance during this journey has reveled him to be not only an example of outstanding professionalism but also a comforting, genuine friend.

I also would like to extend my gratitude to my Professor Richard Todd whose advises greatly influenced the success of this work.

My most sincere obligation goes to Prof. Eliot Fried for having guided me throughout the efforts required to face this scientific challenge. His passion for mechanics and thorough appreciation for the field have inspired me greatly. His support during my visit at his research group is kindly acknowledged.

Moreover, I acknowledge the funding support received by the British Defense Science and Technology Laboratory which have enabled me to complete my doctoral studies.

A special thank is reserved for all my colleagues at the Impact Engineering Laboratory whose friendship and collaborative attitude have contributed to enrich my years in Oxford. In particular, I would like to thank Dr. Antonio Pellegrino for having contributed to my learning of the experimental techniques used in this work.

As all the life-overwhelming experiences, these years could not have been as delightful as they have been, without my friends Michele and Gabor. Their care, willingness to listen and, to always be there for me regardless of the circumstances, have truly remarked the profoundness of their souls and strengthened the endurance of our friendship.

Abstract

The investigation of failure in brittle materials, subjected to dynamic transient loading conditions, represents one of the ongoing challenges in the mechanics community. Progresses on this front are required to support the design of engineering components which are employed in applications involving extreme operational regimes. To this purpose, this thesis is devoted to the development of a framework which provides the capabilities to model how crack patterns form and evolve in brittle materials and how they affect the quantitative description of failure.

The proposed model is developed within the context of diffusive interfaces which are at the basis of a new class of theories named *phase field models*. In this work, a set of additional features is proposed to expand their domain of applicability to the modelling of (i) rate and (ii) pressure dependent effects. The path towards the achievement of the first goal has been traced on the desire to account for micro-inertia effects associated with high rates of loading. Pressure dependency has been addressed by postulating a mode-of-failure transition law whose scaling depends upon the local material triaxiality. The governing equations have been derived within a thermodynamically-consistent framework supplemented by the employment of a micro-forces balance approach. The numerical imple-

mentation has been carried out within an updated lagrangian finite element scheme with explicit time integration. A series of benchmarks will be provided to appraise the model capabilities in predicting rate-pressure-dependent crack initiation and propagation. Results will be compared against experimental evidences which closely resemble the boundary value problems examined in this work. Concurrently, the design and optimization of a complimentary, improved, experimental characterization platform, based on the split Hopkinson pressure bar, will be presented as a mean for further validation and calibration.

Contents

List of Figures

List of Tables

List of Symbols

σ_{ij} $[Pa]$	components of Cauchy stress tensor $[Pa]$
ε_{ij}	components of small strains tensor
E $[Pa]$	Young's modulus
ν $[Pa]$	Poisson's ratio
c $[m/s]$	dilatational speed of sound in the material
c_s $[m/s]$	shear speed of sound in the material
c_r $[m/s]$	Rayleigh wave speed
v_L $[m/s]$	limiting crack speed in Gao's model
$K_{I,II,III}$ $[Pa\sqrt{m}]$	quasi-static stress intensity factor (I, II and III refer to the different mode of fracture)
$K^{dyn}_{I,II,III}$ $[Pa\sqrt{m}]$	dynamic stress intensity factor
$\dot{K}_{I,II,III}$ $[Pa\sqrt{m}/s]$	rate of stress intensity factor
$K_{I,II,III,C}$ $[Pa\sqrt{m}]$	quasi-static critical stress intensity factor for crack propagation
$K^{dyn}_{I,II,III,C}$ $[Pa\sqrt{m}]$	dynamic critical stress intensity factor for crack propagation
$\dot{K}_{I,II,III,C}$ $[Pa\sqrt{m}/s]$	ratio between critical stress intensity factor at crack propagation initiation and time to trigger crack propagation initiation
v_m $[m/s]$	crack-tip speed at branching

$l(t)$ $[m]$	current crack length
$\sum_{ij}^{I}(\theta, v)$	family of non-dimensional functions to define stress components at the crack-tip
A in equation 2.2	area region around the crack-tip
Γ $[m^2]$	infinitesimal region around the crack-tip
R $[m]$	contour around the crack-tip
R_Γ $[m]$	contour of infinitesimal region around the crack-tip
$\dot{K}_I^{dyn}$	rate of dynamic stress intensity factor $[Pa\sqrt{m}/s]$
$\dot{E}_e$ $[J/s]$	rate of internal stored energy
$\dot{T}$ $[J/s]$	rate of kinetic energy
ρ $[Kg/m^3]$	density
$\dot{u}_i$	components of material time derivative of displacement
n_1	component of outward normal along the crack propagation path
F $[Js/mm]$	energy flux
γ $[J/mm^2]$	energy required to create a new crack surface
G $[J/mm^2]$ in equation 2.4	dynamic energy release rate
c_r	Rayleigh wave speed $[m/s]$
σ_S $[Pa]$ in equation 2.11a	unidimensional stress in the specimen obtained from strain recorded on transmitted wave during SHPB test
$\dot{\varepsilon}_S$ $[s^-1]$ in equation 2.11b	unidimensional strain rate in the specimen obtained from strain on reflected wave during SHPB test

$\dot{\varepsilon}$ in equation 2.11c	unidimensional strain in the specimen measured during SHPB
c_B $[m/s]$	speed of sound in the bar used in SHPB test
c_A $[m/s]$	speed of sound in the anvil used in SHPB test
c_S $[m/s]$	speed of sound in the specimen used in SHPB test
l_S $[m]$	length of specimen used in SHPB test
Z	acoustic impedance factor
t_{eq} $[s]$	time required to establish equilibrium in the specimen
v_{str} $[m/s]$	striker velocity in SHPB test
L_B $[m]$	length of input/output bar in SHPB test
D_B $[m]$	diameter of input/output bar in SHPB test
d_S $[m]$	diameter of specimen used in SHPB test
A_B $[m^2]$	cross section of input/out bar used in SHPB test
A_S $[m^2]$	cross section of specimen used in SHPB test
A_A $[m^2]$	cross section of anvil at the interface with the input/output bar used in SHPB test
J_S $[m^4]$	polar momentum of inertia of specimen used in SHPB test
ρ_B $[Kg/m^3]$	density of material of input/output bar in SHPB test
ρ_A $[Kg/m^3]$	density of material of anvils in SHPB test
ω_0 $[1/s]$	fundamental frequency of incident pulse in SHPB test
T $[s]$	period of incident pulse

c_P $[m/s]$	wave phase velocity of a given frequency component of the incident wave
Λ $[m]$	wavelength for a given wave component in the incident wave
ε_f	uni-dimensional strain-to-failure in the specimen during SHPB test
$\dot{\varepsilon}_f$ $[1/s]$	uni-dimensional strain rate at failure during SHPB test
D	damage variable
σ_{HEL} $[Pa]$	stress at Hugoniot elastic limit
σ_i^*	normalized strength of intact material in JH2 model
σ_f^*	normalized strength of fractured material in JH2 model
P^*	normalized pressure in JH2 model
T^*	normalized tensile strength in JH2 model
A, B, C, M, N, D_1, D_2	constant to be calibrated in JH2 model
K_1, K_2, K_3 $[Pa]$	constants to be calibrated in JH2 model
$\Delta\varepsilon^P$	increment of plastic strain in JH2 model
ε_f^P	plastic strain at fracture in JH2 model
ρ_0 $[Kg/m^3]$	initial density of intact material in JH2 model
μ_1	normalized density in JH2 model
ϕ	phase field parameter
$\kappa,\ D_\phi, a_1, b\mu_1, c_1$	constant to be calibrated in Aranson model
$g(\phi)$	degradation function
$\mathscr{F}$	free energy functional in Aranson model

$P(\phi)$	double-well potential in Aranson model
$V(\phi)$	double-wll potential in Hakim and Karma model
ψ_0^+ $[J/m^3]$	active part of reference strain energy functional in Miehe and Landis model
ψ_0^- $[J/m^3]$	passive part of reference strain energy functional in Miehe and Landis model
H $[J/m^2]$	compact history strain energy functional in Miehe and Landis model
e_0 $[J/m^3]$	specific internal energy
s_0 $[J/Km^3]$	specific entropy
θ $[K]$	temperature
P_{ij} $[Pa]$	components of first Piola-Kirchhoff stress
B_i $[N]$	components of body force
$\ddot{U}_i$ $[m/s^2]$	components of material point acceleration
ψ $[J/m^3]$	energy functional
$\psi_{F,a}^0$ $[J/m^3]$	active part of reference strain energy functional
$\psi_{F,p}^0$ $[J/m^3]$	passive part of reference strain energy functional
$\psi_0^{h^+}$ $[J/m^3]$	active part of reference volumetric strain energy functional
$\psi_0^{h^-}$ $[J/m^3]$	passive part of reference volumetric strain energy functional
ψ_c $[J/m^3]$	strain energy threshold
ψ_0^d $[J/m^3]$	deviatoric part of reference strain energy functional
$\Gamma_{\phi,2}$ $[J/m^3]$	phase field fracture energy functional

F_{ij}	components of deformation gradient tensor
L_{ij} $[1/s]$	components of velocity gradient tensor
D_{ij} $[1/s]$	components of rate of deformation tensor
W_{ij} $[1/s]$	components of spin tensor
$\ddot{F}_{ij}$ $[1/s^2]$	components of rate of rate of deformation tensor
$\dot{F}$ $[1/s]$	effective rate of deformation
$\ddot{F}$ $[1/s^2]$	effective rate of rate of deformation
χ_i $[Pa]$	components of micro-stress vector
π $[N]$	internal micro-force
γ $[N]$	external micro-force
λ $[N]$	micro-traction
G_c $[J/mm^2]$	mode-I critical energy release rate
$\tilde{G}_c$ $[J/mm^2]$	effective critical energy release rate
l_0 $[m]$	phase field diffusive zone
l $[m]$	micro-inertia length-scale
l_ϕ^0 $[m]$	initial constant value of the micro-inertia length scale
η $[Js/m^3]$	dynamic phase field viscosity
β	scaling parameter for critical energy release rate
χ	material triaxiality
χ_L	triaxiality lower bound of tri-linear critical energy release rate scaling law
χ_U	triaxiality upper bound of tri-linear critical energy release rate scaling law

σ_c^0 $[Pa]$	critical value of stress at softening, predicted according to quadratic formulation for the degradation function (equation 4.40)
σ_c $[Pa]$	stress at softening
ε_c^0	critical value of strain at softening, predicted according to quadratic formulation for the degradation function (equation 4.40)
$\sigma_{c,e}^0$ $[Pa]$	quasi-static tensile strength obtained from experiments
$\sigma_{c,e}$ $[Pa]$	rate-dependent tensile strength obtained from experiments
σ_1, σ_2, σ_3 $[Pa]$	principal stresses
$\tilde{\sigma}$	stress normalized by σ_c^0
σ_∞ $[Pa]$	remote applied stress
p $[Pa]$	pressure
$\sigma_{c,e,comp}^0$ $[Pa]$	quasi-static compressive strength obtained from experiments
σ' $[Pa]$	deviatoric stress
I_1, I_2, I_3	stress invariants
$\dot{\varepsilon}$ $[1/s]$	effective strain rate
$\dot{\varepsilon}_0$ $[1/s]$	critical strain rate for rate-dependent transition in exponential law in equation 4.45
$\dot{\varepsilon}_{0,c}$ $[1/s]$	critical strain rate for rate-dependent transition in compression
D_0 $[J/s]$	parameter used to normalize the rate of dissipation
T_0 $[s]$	parameter used to normalize time
dt $[s]$	history output time-step

Δt $[s]$	simulation time step
E_d $[J]$	energy dissipated due to phase field evolution
t_r $[s]$	rise time of applied load
t_d $[s]$	time at which unloading in the ideal incident pulse starts
t_{tot} $[s]$	total duration of incident pulse
n_2 in equation 4.45	constant to be calibrated for exponential law employed for the rate-dependent tensile strength
$\gamma_1, \gamma_2, \gamma_3, \gamma_4, \gamma_5, \gamma_6$	parameters to be calibrated in rate-dependent scaling laws for l and η

Chapter 1

Introduction

This chapter outlines the landscape which frames the challenges identified and subsequently addressed in this thesis. The engineering context, within which Impact Engineering represents a key discipline, shall be presented as the driver to set the research goals. A series of objectives and a strategy for their realization is proposed, along with a summary on the specific contributions presented in the subsequent chapters.

1.1 Background and motivation

Understanding the dynamic failure of materials plays an important role in the design of structural components employed in engineering applications involving impact and extreme loading conditions. Research initiatives have been undertaken to boost product development as well as improve safety and reliability under these regimes of operation. Research on this front has been traditionally motivated by leaders within the aerospace/defence and automotive industries, with implications to the civil engineering field and most recently embraced by researchers from the biomedical sector as well. Progress made on theories used to describe the phenomena of crack nucleation and propagation, now easier to observe, record and measure by means of improved experimental capabilities, have led to a more solid basis to build numerical tools able to simulate real-world scenarios. The employment of computational tools becomes of key importance in engineering design in which a more accurate and physics-based integration among virtual prototyping, testing and component optimization is sought. Improved numerical capabilities also contribute to a significant reduction in costs, development-cycle time and resources which should be allocated to optimize manufacturing processes and assess material behaviour over all life-stages of the component within which they are employed.

Governmental agencies such as the British Defence and Science Technology Laboratory (DSTL) have participated and directly funded a series of research campaigns, such as the MAST programme, with the aim of investigating the failure characteristics of several classes of materials – *e.g.* ceramic composites – identified as potential candidates to meet the desired requirements for ballistic performance. These efforts are especially intended to improve the reliability of protective armour systems as well as achieve a low-cost lightweight solution. These objectives translate into the need to improve the experimental capabilities to assess if the material shows any rate-dependent behaviour, potentially arising under these extreme regimes, as well as measure its relevant mechanical properties. The latter certainly assists the engineering design of the component and motivates development of constitutive theories and their implementation, within computational platforms. Advanced numerical methodologies therefore enable to study these phenomena and exploit the measured properties for their calibration and validation. It is certainly within this context that a fertile ground for scientific challenging endeavours can be found.

1.2 Aim and objectives

The research activities presented in this thesis have been driven by the desire of formulating a rigorous mathematical framework, based on continuum thermodynamics and recently developed phase field theories, to address specific challenges still remaining in the ability to simulate failure of materials showing a rate-pressure-dependent mechanical response. The achievement of this overall goal can be thought to be segmented in a sequence of objectives which can be stated as it follows:

- Review of the physical mechanisms associated with dynamic brittle failure and evaluation of current theoretical frameworks which have been developed for the description of these phenomena. Subsequently, it becomes crucial to appraise the benefits and limitations of the main existing numerical methodologies which exploit the underlying theoretical basis. In conjunction to this, a survey of the experimental characterization capabilities, which are needed to provide quantitative description, calibration and validation of these models, should be carried out;

- Detailed description of a class of theories, namely *phase field models*, which have been identified as a suitable candidate for the accomplishment of the project goal;

- Development and numerical implementation of an improved phase field model which enhances existing theories with the capability of predicting rate-pressure-dependent brittle failure as dictated by high-inertia effects and material confinement;

- Demonstration of newly developed capabilities based upon comparison of the obtained result against relevant benchmarks taken from the literature;
- Optimization of experimental characterization techniques which could be used to calibrate and validate the model as it is applied to study material behaviour under loading regimes resembling impact loading conditions in materials employed in armor applications.

1.3 Research strategy

The aim and objectives listed above have been set after a thorough review of the literature on the topic which also fall within the scope of interest of the funding body, here acknowledged as DSTL.

In this context, a research strategy based upon the requirement of building a thermodynamically-consistent framework, able to include rate and pressure dependent effects, has been proposed. The former has been addressed by deriving a new set of governing equations which now account for inertia contribution associated with a newly-introduced rate dependent length scale. As far as the latter requirement is concerned, a transitional mode-of-failure law, based on material triaxiality, has been explored. The derivation of the governing equations and constitutive laws has been carried out on the basis of classical continuum mechanics arguments combined with fundamentals of phase field theories for fracture. The numerical implementation of the newly-proposed framework has required the development of a in-house code which could overcome the limitations of available commercial platforms. Although finite element packages such as Abaqus and LS-DYNA have shown remarkable accuracy in modelling dynamic failure events, the flexibility they provide to the user in terms of ad-hoc development is still somewhat limited. The employment of user-material subroutines and/or user-element routines does not allow for improvement in the simulation methodologies when they require data management, solvers and or physics which do not align with their built-in infrastructure. These research activities have been conducted in parallel with the design and optimization of an experimental apparatus, based on the Split Hopkinson Pressure Bar technique. This will serve as a complementary capability to those available within DSTL and it is envisaged to suggest a calibration platform in support of the model presented in this thesis.

1.4 Thesis outline

The thesis is organized in eight chapters which present the research activities which have contributed to the development and enhancement of capabilities required to validation and calibrate a *Thermodynamically-Consistent Rate-Dependent Phase Field Model for the Description of Failure Pattern in Dynamic Brittle Fracture*. A review of research works which have attempted to describe the mechanisms of dynamic brittle fracture is presented in Chapter 2 along with a survey of the experimental and modelling approaches that have aimed to study these phenomena. Chapter 3 is dedicated to the presentation of the state-of-the-art of phase field theories with focus on their application to model fracture behaviour. This discussion provides a solid background to introduce the novelties at the basis of the proposed model, its implementation and capabilities in the subsequent chapters. In particular, derivation of the governing equations and constitutive relations based on micro-force balance and continuum thermodynamics are presented in Chapter 4. Therein, the implementation within a finite element framework is discussed along with a proposed numerical calibration strategy. Results on benchmarks related to loading conditions under which a single mode of fracture arises are provided in Chapter 5. Subsequently, the model predictions for loading cases which promote mixed-mode fracture and distinct mode of failure transition are assessed in Chapter 6. The development of an improved experimental technique for the validation and calibration of the model as applied to study the failure response of material containing distributed microdefects, such as ceramics, is reported in Chapter 7. Moreover, a brief discussion of the model performance under these conditions is provided. Results associated with the chosen benchmarks will be, whenever possible, compared against relevant experimental evidences taken form the literature. It must be noted that these comparisons are aimed to provide the reader with a mean to qualitatively link the results with the literature under the assumption that loading conditions and material behaviour are comparable to those employed in the simulations. In the last chapter, a recapitulation of the work presented in the thesis and a summary of the most relevant findings are outlined, along with recommendation for future research.

Chapter 2

Literature Review

This chapter introduces the wider literature needed to contextualize the field of dynamic fracture within which the material in this thesis has been developed in response to the aforementioned objectives. The theoretical foundations, as well as a description of the mechanisms through which dynamic brittle failure manifest itself, are discussed. Experimental characterization techniques for the quantitative assessment of these phenomena are reviewed with high regard to the split Hopkinson bar apparatus. The main computational models which have been developed in this realm are presented in order to identify their advantages and drawbacks.

2.1 Introduction

Brittle materials are largely employed in several applications, relevant to the defense and civil industries among others, which expose them to phenomena such as impact and blasting [1]. Representative examples include the use of ceramic tiles as armour protection [2], limestone rock for the manufacturing of sands [3] and amorphous or semi-crystalline polymers such polycarbonate (PC) and poly-methyl-methacrylate (PMMA) as a transparent protective substrate in windshields and lenses [4]. When subjected to high rates of loading these materials exhibit complex combinations of failure modes which involve dynamic microcracking, shearing and microplasticity which might lead to the formation of multiple fragments and comminution. The activation and progression of these processes are largely dependent upon the microstructure configuration of the material which might have pre-existing defects such as microcracks and porous as well as embedded second phase particles. Moreover, mode of failure transition can be observed if under certain operational conditions threshold levels for the confining pressure and temperature are exceeded.

Dynamic fracture mostly focuses on the studying of failure in materials which are subjected to loading regimes in which the nature of the waves propagation and their interaction, along with inertia effects, become relevant. These requirements suggest that classical theories, which however have succeeded in describing the motion of bodies containing cracks under either quasi-static or steady-state regimes, might present limitations and challenges which have yet to be addressed [5].

2.2 Dynamic fracture mechanics: principles and extension to crack-tip inertia effects

The analysis of the behavior of solids containing cracks within the framework of classical continuum dynamic fracture relies on the use of key principles of elastodynamics. This subject has been extensively treated in many monographs written on the topics [6].

It has been widely accepted that the dynamic mechanical fields around a crack-tip obey a square-root singular distribution as for the asymptotic solution for the case of quasi-static loading. For instance, under mode-I single opening loading conditions, the stress can be described by a leading singular component as it follows:

$$\sigma_{ij}(r,\theta) = \frac{K_I^{dyn}(t,v)}{\sqrt{2\pi r}} \sum_{ij}^{I}(\theta,v) \tag{2.1}$$

The stress magnitude is governed by the value assumed by the *dynamic stress intensity factor*, $K_I^{dyn}(t,v)$, which itself depends on the boundary value problem configuration and upon the loading time and the instantaneous crack-tip speed, which are indicated with t and v, respectively. The various components of the mechanical fields vary in a polar system, with coordinates r and θ, centred at the crack-tip, according to the non-dimensional functions $\sum_{ij}^{I}(\theta,v)$. It has to be noted that these expressions are valid as long as the crack-tip moves under steady state conditions. If the crack-tip is exposed to highly transient loads it becomes necessary to account for the loading history as it reflects on the time variation of the stress intensity factor, $\dot{K}_I^{dyn}(t,v)$. Asymptotic solutions for the crack-tip fields under these regimes have been reported by Freund [6] and later analysed for the case of crack-tips travelling at non-uniform speeds by Rosakis et.al. [7], Freund and Rosakis [8] and Liu and Rosakis [9]. If the stress at the crack-tip reaches a critical value, crack propagation initiation occurs, therefore requiring an energy balance equation which accounts for the dissipation associated with the crack growth in a Griffith-sense. The rate of energy balance can be written for a contour around the crack-tip, R, which excludes an infinitesimal region, Γ, within which the mechanical fields become singular:

$$\dot{E}_e + \dot{T} = \frac{d}{dt}\int_{R-R_\Gamma} \frac{1}{2}(\sigma_{ij}\varepsilon_{ij} + \rho\dot{u}_i\dot{u}_i)dA \tag{2.2}$$

where the terms $\dot{U}$ and $\dot{T}$ are the rate of the stored internal and kinetic energy, respectively. Application of the Ryenolds and divergence theorems leads to the definition of the energy flux, F, which represents the energy dissipated due to crack growth:

$$F = \int_{\Gamma} \left(\sigma_{ij} n_j \dot{u}_i + \frac{1}{2}(\rho u_i u_i + \sigma_{ij} u_{i,j}) v n_1 \right) ds \tag{2.3}$$

where n_1 is the component of the outward normal in the direction crack propagation path and v is the crack-tip velocity. The condition for crack propagation initiation therefore requires that the above quantity exceeds a critical material-dependent value which can be assumed to be the energy required to create a new crack surface, γ, proportional to crack-tip velocity. This allows to define a dynamic energy release rate as below:

$$G = v^{-1} F = \gamma \tag{2.4}$$

By substituting the explicit form for the crack-tip mechanical field, as reported in equation 2.1, leads to an energy balance equation from which an explicit law for the crack-tip velocity can be obtained [10]:

$$\frac{1-v^2}{E} A(v)(K_I^{dyn}(t,v))^2 = \gamma \tag{2.5}$$

where E is the Young's modulus and the other terms are calculated as:

$$A(v) = \frac{v^2 a_d}{(1-v)c_s^2 D} \tag{2.6a}$$

$$a_d = \sqrt{1 - v^2/c^2} \tag{2.6b}$$

$$a_s = \sqrt{1 - v^2/c_s^2} \tag{2.6c}$$

$$D = 4 a_d a_s - (1 + \alpha_s^2)^2 \tag{2.6d}$$

where c and c_s are the dilatational and shear wave speed of the material. It has to be noted that in Equation 2.5 a condition for crack propagation is provided along with one for crack arrest to occur, since a relation between the driving force and the crack velocity is established. Moreover, it can be noted that a theoretical upper bound for the crack velocity, correspondent to the surface Rayleigh wave speed, c_r, can be identified as the condition for singularity in the first term in equation 2.5. As it shall be discussed in the following section, this limiting value is seldom attained in experiments. Moreover, it has to pointed out that the expressions presented above, have been derived on the basis of assuming the crack-tip to be a *point* which does not contribute to the inertia of the system. In particular, the motion of the crack-tip, assumed unperturbed and traveling in an ideal infinite medium, has been described by an energy balance equation (2.5) in which the total dissipation is presumed to depend upon crack-tip velocity itself only. These approaches have shown remarkable effectiveness in the absence of instability and wave interactions with the crack surfaces. Few researchers have proposed extensions to LEFM theories, which drop out this assumption, in order to explain certain features of crack dynamics. Marder [11, 12] proposed an equation which considers crack-tip inertia as associated with time scales at which the interaction between crack surfaces and boundaries of the medium, and/or with any inhomogeneities encountered by the crack front [13], become significant. Therefore, Marder proposed an extension to second order rate effects of the equation of motion presented in 2.5 which reads as:

$$\gamma(v) = G(v, \dot{v}) \approx W\left(1 - \frac{b\dot{v}}{c^2}\left(1 - \frac{v^2}{c_r^2}\right)^{-2}\right) \tag{2.7}$$

As it can be seen, the proposed equation involves the contribution of a *mass-like* term associated with crack-tip inertia which scales with $(1 - v^2/c^2)^{-2}$. In the above, the supplied energy W is responsible for driving crack growth against the material resistance $\gamma(v)$ which assumes finite value as $v \to c_r$. This condition ensures that c_r is still the theoretical upper limiting value for the crack speed and that the mass term tends to a finite value as $\dot{v} \to 0$.

Bouchbinder [14, 15] proposed a *weakly nonlinear theory of fracture* in attempt to overcome some of the limitations associated the LEFM approach to describe the mechanical fields close to a moving crack-tip under high loading rates. As it was shown by Rice [16] and Langer and Lobkovsky [17], as the speed of crack propagation tends to c_r the ratio, $\sigma_{xx}(r,\theta=0)/\sigma_{yy}(r,\theta=0)$, between the stress components ahead of the tip increases. Bouchbinder showed that this leads to the rise of a compressive component of deformation, $\partial_y u_y(r,\theta=0,v)$, ahead of the crack-tip, when a characteristic speed is reached. In Bouchbinder's theory the body motion is described by a higher order strain energy functional which supplements the LEFM fields with a contribution due to nonlinear hyperelastic deformations which are governed by the choice of a proper third order elastic constants as proposed by Murnaghan [18]. The deformation gradient is therefore described as:

$$\nabla\mathbf{u} = \nabla\mathbf{u}^{(1)} + \nabla\mathbf{u}^{(2)} + \mathcal{O}(|\nabla\mathbf{u}|^{(3)}) \tag{2.8}$$

where the superscripts, 1 and 2, refer to the solution based on LEFM and higher order nonlinearities, respectively. According to Bouchbinder, the higher order deformation gradient term assumes the following generic form:

$$u_x^{(2)} \approx \frac{K_{I,II}^2}{\mu^2}(\log r + f_x^{I,II}(\theta,v)) \tag{2.9a}$$

$$u_y^{(2)} \approx \frac{K_{I,II}^2}{\mu^2} f_y^{I,II} \tag{2.9b}$$

It was shown that this solution retains the physical conditions of positive-opening for increasing crack velocity. Importantly, Bouchbinder et al. [19] argued the existence of an intrinsic, rate-dependent, limiting length scale at which the two solutions become comparable, *i.e.* $|\nabla \mathbf{u}^{(1)}| \simeq |\nabla \mathbf{u}^{(2)}|$. Hence, as this nonlinear region develops, the crack front can be thought to depart from its theoretical massless idealization. The contribution of this *inertia-like* terms depends nontrivially on the loading regimes, whose amplitude reflects on the size of this new length scale.

2.3 Rate-Dependent Brittle Failure

In the following discussion, a summary of evidence of rate-dependency in the mechanisms responsible for failure in brittle materials is provided.

Experimental investigations carried out by Ravi-Chandar and Knauss [20] on nominally unbounded Homalite-100 sheets under mode I loading conditions provided remarkable evidence of rate-dependent crack-initiation behaviour as well as of the existence of a material-dependent lower bound for the stress intensity factor at which crack arrests without prior deceleration. Conversely, crack deceleration was detected by Bradley and Kobayashi [21] in specimens in which wave reflection/interaction with the crack surfaces were allowed. Microstructural changes in the crack morphology were reported by Ravi-Chandar and Knauss [22], who showed that a transition from mirror to mist and then to hackle occurs as the rate of loading increases. The formation, growth, interaction, and progressive coalescence of micro-cracks emerging from a plane parallel to the main moving crack were observed. Depending on the rate of loading and specimen configuration, distinct macroscopic branching [23, 24] or multi-patterned frustrated micro-branching developed [25, 26], with angles between 15^0 and 45^0. Several experimental studies have shown that the crack speed tend to a maximum steady-state value close to 40% of the theoretical Rayleigh limit at which major unstable oscillations can be observed in conjunction with branching formation [27, 28]. These results highlighted differences with respect to the outcomes of theoretical analysis performed by Yoffe [29] in which, on the basis of an inertia dependency of the local stress fields, branching angle of 60^0 and a crack-speed threshold of 60–70% the Rayleigh wave speed were derived. Livne et al. [30] and Boué et al. [31] pointed out that perturbations associated with out-of-plane wave reflections could be the cause of micro-branching instability and lower maximum crack speed attained, therefore suggesting that the three-dimensional nature of the phenomenon should beconsidered. Washabaugh et al. [32] proved that crack speeds closer to the Rayleigh limit can be attained if the conditions for micro-branching instability are suppressed; similarly, as shown by Rosakis et al. [33], intersonic regimes can be achieved if weak interfaces are placed along the crack plane. Motivated by the discrepancy between theoretical and experimental results, Gao [34] proposed an analytical model based on the assumption that the crack-growth path, at lower scales, can be idealized as having a oscillatory – *wavy-like* – character. It was argued that the crack growth process involves a competition between inertial effects at two different scales, namely a high inertia near-crack-tip zone, which promotes instability, and a surrounding lower inertia field. Subsequently, Gao [35] used a nonlinear analysis based on a hyperelastic constitutive law to show that the limiting crack speed is affected by the local, near-crack-tip, material response in which dissipative effects due to inertia and reduced local lattice vibration might arise. A limiting value for the crack speed, v_L, was proposed as:

$$v_L = c_s \sqrt{\frac{\sigma_{max}}{\mu_L}} \tag{2.10}$$

where σ_{max} and μ_L are the biaxial bond strength and the local shear modulus, respectively. It was further argued that induced lattice vibration in the crack front can be responsible for further dissipation and therefore lower the crack-speed. These arguments were later supported by molecular dynamic simulations reported by Buehler and Gao [36, 37]. A cohesive zone model based on a phenomenological calibration of the dissipation contribution associated with high rates of energy supply into the material, which might result in crack-tip inertia effects, was proposed by Karedila and Reddy [38].

Although the above discussion as mainly concerned failure in brittle solids in which rate-dependent mechanisms arise under dynamic mode-I tensile loading conditions, a vast range of evidences of rate-dependent behaviour under compressive and confined loading conditions exist.

Pioneering research on this front has been carried out by Kalthoff and co-workers [39, 40]. Their investigations aimed at studying modes of fracture in elasto-plastic solids showing rate-pressure-dependent brittle-to-ductile failure transition. Experiments were mainly conducted on plates containing either a pre-existing notch or a sharp crack by means of the technique of loading crack by edge impact (LECEI). The experimental setup used by Kalthoff is presented in Figure 2.1. The setup consists of a specimen impacted by a projectile on the edge between two parallel cracks. Upon impact a compressive stress wave is generated which start travelling parallel to the crack plane. As the wave reaches the crack tips an initial nominal state of mode-II loading conditions, is established. The rest of the specimen is under stress-free conditions as long as no significant interaction between the stress-field around the crack-tip and the wave reflected from the opposite free-boundary occurs. Similar experimental conditions, however involving plates containing only one crack, hence resembling asymmetric impact conditions, have been employed by Ravi-Chandar et. al. [41, 42] and Kalthoff and B́urgel [43]. In particular, Ravi-Chandar et. al. [41]

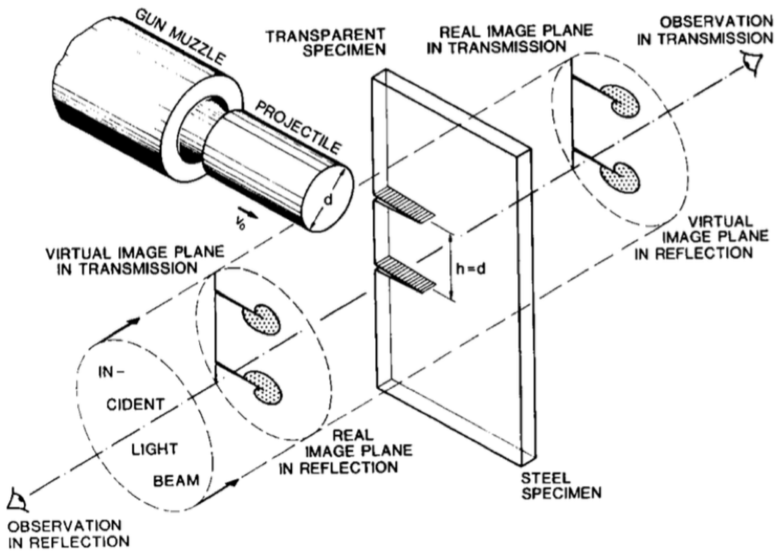

Figure 2.1: Schematic representation of experimental setup used by Kalthoff

showed that brittle polymers, such as PMMA, present a transition in the mode of failure which depends upon the loading rate. Their results revealed that under relatively low velocities the material fails by induced mode-I crack propagation which occurs in the form of an inclined kink propagating from the initial notch. As the rate is increased a transition to shear driven mode-II failure was observed. This result was explained by pointing out that, at these rates, a regime of high triaxiality is established at the crack-tip. This condition is responsible for the suppression of the opening mode and favours excessive material deformation along the line of maximum shear. Mode of failure transition driven by increasing triaxiality was also shown on PMMA plates, under dynamic biaxial compression, containing an inclined centred crack, by Broberg [44]. A similar rate-dependent behaviour was observed in PMMA compact compression specimens (CCS) loaded by means of the split Hopkinson pressure Bar

(SHPB) by Rittle and Maigre [45].

The studies examined above have been mainly concerning solids containing a primary dominant crack and assumed to be homogeneous elsewhere. If a population of pre-existing flaws, such as microcracks, is embedded in the medium, rate effects become more relevant; the process in which these defects are activated and interact dictates the macroscopic failure response. It has been extensively observed that failure under dynamic compression occurs as a result of the initiation of wing cracks which nucleate from the pre-existing inhomogeneity as a result of a local state of tensile stress [46]. The interaction and coalescence of these cracks eventually leads to macroscopic axial splitting along the direction of the applied load [47, 48]. If the material is subjected to increasing confinement a transition to failure due to plastic slip mechanisms at the mesoscale/microscale can occur [49].

2.4 Experimental Characterization

The appraisal and quantitative description of failure behaviour of brittle materials under high strain rate conditions requires the development of a wide range of characterization techniques able to capture phenomena which occur over time scales spanning from years (creep) to nanoseconds (shocks). An excellent review on this topic has been provided by Field et. el. [50]. A schematic representation of the different techniques and the domain within which they operate is proposed in Figure 2.2. While conventional servo-hydraulic machines can cover strain rates up to orders of 10 $[s^{-1}]$, ad-hoc techniques should be designed in order to cover higher loading regimes. Assessment and measurement of the strain rate-dependent nature of material failure properties, such as strength and strain-to-failure, can be carried out by

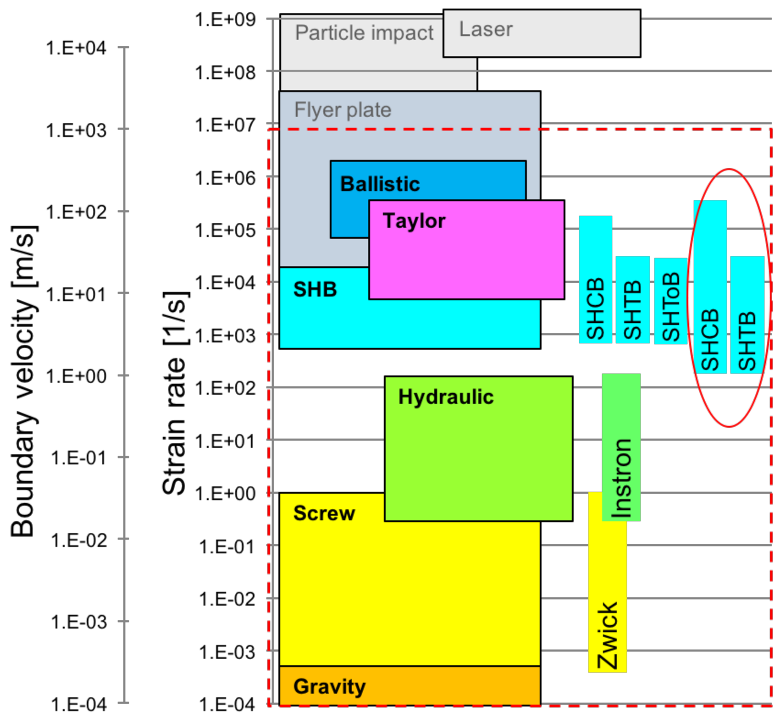

Figure 2.2: Experimental characterization techniques at different loading rate regimes

means of the split Hopkinson bar. This apparatus, can be designed and optimized in order to provide quantitative measurements within ranges of 10^1 - 10^4 $[s^{-1}]$. This methodology, as it is applied to measure the behaviour of brittle-hard materials under nominal compression, will be reviewed in details in the following section. Ballistic regimes, *i.e.* $10^5 - 10^6$ $[s^{-1}]$ can be attained by employing techniques such as the Taylor impact and the flyer impact test. These experiments consist in impacting a plate of the material whose properties ought to be measured with a rod or another plate at varying angle. Information on the inelastic deformation process can be obtained although no-direct link between what can be observed/recorded and common mechanical failure properties can be established. However, design variables such as depth of penetration (DoP), fragment size and distribution and shock quantities such as the Hugoniot elastic limit can be collected [51].

2.4.1 The split Hopkinson pressure bar apparatus

The development of the SHB technique has been originally attributed to the pioneering work of John Hopkinson [52, 53], who intended to study the effect of compressive stress wave generation and propagation on iron wires. Later, his son Bertram Hopkinson used a similar experimental setup, which included a ballistic galvanometer and a contact device measurement cell, to estimate the elongation of wires loaded by dynamic impulses [54, 55]. In 1948 Davies published a critical review of the apparatus as developed at that time [56] and highlighted some of the issues related to the wave dispersion occurring in finite rods due to Pochhammer-Chree frequency oscillations [57, 58]. Moreover, Davies proposed an analytical expression to calculate the pressure-time history from the electrically measured longitudinal and radial displacement of the impacted bar. Significant importance has been granted to Kolsky's contribution who first proposed the Split Hopkinson (or Kolsky) Pressure Bar (SHPB) as a technique to characterize the high strain rate behaviour of solids under compression [59]. In his work, he modified the original Davies' apparatus by inserting a thin disc-shaped specimen between the loaded bar and the extension bar. A set of analytical expressions were derived to obtain the sample stress-strain response from the data recorded on the bars by means of cylindrical condensers.

Throughout the years, researchers have modified the SHPB apparatus in order to account for other loading conditions such as tension [60, 61], shear [62] and torsion [63] as well as have attempted to study their combined effects[64]. In the following, a critical review of the SHPB is carried out with the aim of highlighting its operational conditions and requirements to be successfully employed to characterize hard-brittle materials such as ceramics, under nominal compression.

Operational principles of SHPB The schematic representation of the SHPB configuration adopted at the Impact Engineering Laboratory at University of Oxford is shown in Figure 2.3 and is described here.

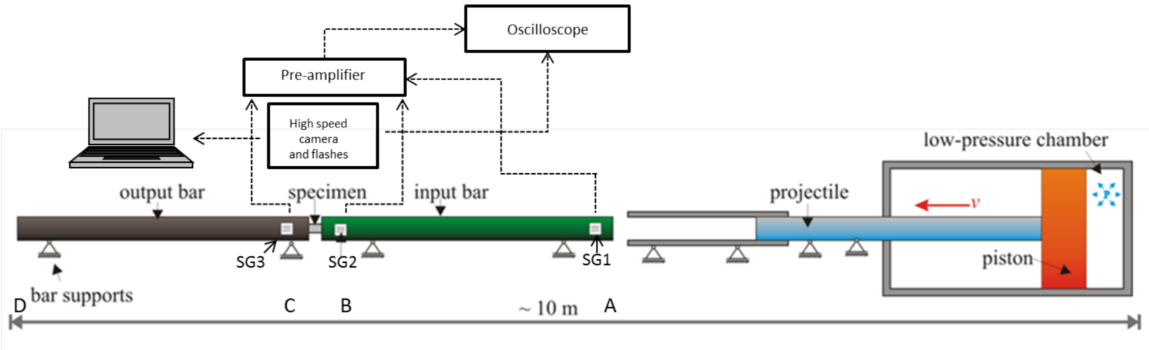

Figure 2.3: SHPB configuration

The apparatus consists of two cylindrical bars, namely the input bar (AB) and the output bar (CD) with the sample inserted in between (BC). The projectile is fired at a certain prescribed velocity by a pressurized container. Upon impact of the striker with the input bar, a planar compressive stress wave, which then starts traveling along the bars, is generated. When the wave reaches the input bar/specimen interface part of its content is reflected into the input bar while the rest passes through the specimen and transmits into the output bar after several reverberations. The impedance of the sample, defined as the product of the material characteristic wave speed (c), density (ρ) and cross sectional area (A) is usually lower than the one of the bar which in turn results in a tensile reflected wave. The loading apparatus is supported by a bearing system which ensures the alignment between the bars. Strain gauges are mounted on both the bars at stations indicated in Figure 2.3 as G1, G2 and G3 to record the incident, reflected and transmitted waves, respectively. The apparatus also includes data acquisition devices such as signal amplifier, oscilloscope and high speed camera. The strain gauges measurements can be used to perform a one-dimensional wave analysis which provides with expression for the stress, strain rate and strain in the specimen [65]:

$$\sigma_S(t) = \frac{A_B E_B \varepsilon_T(t)}{A_S} \tag{2.11a}$$

$$\dot{\varepsilon}_S = -\frac{2c_B \varepsilon_R(t)}{l_S} \tag{2.11b}$$

$$\varepsilon(t) = \int_0^t \dot{\varepsilon}_S(t) dt \tag{2.11c}$$

where the subscripts B and S refer to the bar and specimen respectively; the term E indicates the Young's modulus while l_s is the gauge length of the specimen. The quantity ε_R corresponds to the reflected pulse on the input bar (measured at G2) while ε_T is related to the transmitted signal on the output bar (measured at G3). It should be pointed out that the validity of the results obtained through the previous expressions depends on several requirements which are discussed in the next sections.

Dynamic equilibrium The condition of dynamic equilibrium requires that the stress state within the specimen is uniform. This can be ensured by applying a loading pulse which has a rise time long enough to ensure that several reverberations of the wave occur within the specimen. It is desired that the specimen does not reach the final uni-axial compressive strength before the *ring-up* time is elapsed. Ravichandran and Subhash [66] showed that this condition depends on the impedance mismatch between the specimen and the loading system defined as:

$$Z = \frac{A_B \rho_B c_B}{A_S \rho_S c_S} \tag{2.12}$$

They concluded that, for a range of different Z, results converge to a requirement on the total duration of the loading/unloading pulse reported below:

$$t_{eq} = \frac{4 l_S}{c_S} \tag{2.13}$$

Bars operating conditions It is assumed that the stress in the bars remains within the elastic limit and the ends in contact with the specimen surfaces maintain their flatness. The level of stress in the bar is proportional to the striking velocity:

$$\sigma_B = \alpha \rho_B c_B v_{str} \tag{2.14}$$

where v_{str} is the velocity at which the projectile is fired. The coefficient α depends on the projectile and input bar materials and cross section areas; for the case of two rods of the same material and cross section. Moreover, the stress applied on the bar is related to the maximum stress which is desired in the specimen; therefore, it could be lowered by reducing the sample cross section. However, as the sample dimensions decreases the probability of causing bars indentation increases; this is particularly crucial in the case of testing hard materials such as ceramics. Moreover, indentation at corners or asperities lead to a non-uniform distribution of stress in the proximity of the bar end, which negatively affects the results.

Wave dispersion It is assumed that the wave goes under minimal dispersion while it travels along the bar and reflects/transmits at the interfaces with the specimen. Dispersion occurs when the wavelength of the relevant frequency in the spectrum of the loading train is comparable to the bar diameter. Therefore, a non-uniform stress distribution along the cross section of the bar arises which in turn discourages reliance on surface measurement on the bar. However, if the duration of the incident pulse is sufficiently bigger than the time required for a wave to complete a transit along the bar diameter, then the dispersive effects are minimized [67]. Moreover, when a stress wave propagates in a slender bar, dispersion can occur longitudinally because of the different wave phase velocities present in the spectrum of the loading train. Therefore, if the wave does not conserve its content, positioning the strain gauge stations at a certain distance away from the specimen could lead to a misleading result. This class of dispersive effects can be minimized by controlling the ratio between the length and the diameter of the bar, L_B/D_B. In particular, Davies et. al. [56, 68] concluded that the ratio of the bar diameter to the wavelength of the predominant frequency, D_B/Λ, should be smaller than 0.1. This in turn results in a constraint on the bar dimensions such that $L_B/D_B \geq 20$.

The applied incident pulse fundamental frequency, ω_0, and its period, T, are related to each other through:

$$\omega_0 = \frac{2\pi}{T} \tag{2.15}$$

The wave phase velocity of each frequency component can be calculated as suggested by Follansbee and Frantz [67]

$$c_P = c_0\left(1 - c_B^2\pi^2\left(\frac{D_B}{2\Lambda}\right)^2\right) \tag{2.16}$$

Therefore, by imposing the constraint on D_B/Λ, it can be obtained that:

$$\left(\frac{c_0}{c_p}\right)\left(\frac{\omega}{\omega_0}\right) < 0.1 \tag{2.17}$$

Where Equation 2.15 can be rewritten in terms of the bar properties as:

$$\omega_0 = \frac{4\pi c_0}{d_B} \tag{2.18}$$

Given these relations, the value of the fundamental frequency can be calculated. This result can be then used to compute its period, *i.e.* by recalling Equation 2.15. For the case of linearly rising triangular incident pulse, its peak can be assumed to be reached at half of the entire period, T. Therefore, if a value for the strain-to-failure of the material, ε_f, is assumed, the associated strain rate can be estimated as below:

$$\dot{\varepsilon}_f = \frac{2\varepsilon_f}{T} \tag{2.19}$$

Dynamic Recovery Effects The objective of the present work is to investigate how the SHPB methodology can be applied to study the mechanical failure of brittle materials when subjected to a single dynamic compressive load. However, the SHPB traditional configuration favours the occurrence of repetitive loading on the sample because of the multiple wave reflections inside the input bar. Precisely, when the incident compressive stress wave reaches the specimen/input bar interface part of it reflects back as tensile and changes its sign again when it arrives at the free end where the original impact with the striker occurred. If the specimen does not fail completely under the application of the first compressive pulse, the aforementioned process results in a series of multiple reloading steps; in this circumstance the results computed by means of the expressions 2.11 are meaningless because the progressive accumulation of damage is not taken into account. Nemat-Nasser et. al. [69]suggested to revise the original configuration of the SHPB by incorporating a momentum-trap device at the input bar/striker interface such that the second reflection of the tensile wave travelling back toward the free end is avoided.

Anvils As discussed previously, the geometrical mismatch between the hard-brittle sample and the bars, usually made of steel or titanium, could cause damage to the equipment. This can be prevented by inserting a pair of anvils at the specimen/bars interface. A fundamental requirement is that their acoustic impedance matches the bar at which they are attached meaning that the content of the incident stress wave does not change significantly because of their insertion. The latter can be achieved by satisfying the following equality:

$$\rho_A c_A A_A = \rho_B c_B A_B \tag{2.20}$$

Sunny et. al. [70] proposed different anvil configurations based on tapered truncated-cone inserts and semi-dogbone shapes. In their work, a 2-dimensional finite element analyses showed that this class of anvils geometries mitigates the stress concentration at the specimen interface and leads to a more gradual loading of the material toward the dynamic equilibrium. Such a design could be also employed when experiments involving thermo-mechanical loads are performed. The area transition between the specimen/anvil interface and the anvil/bar interface would guarantee a smoother transition of the applied temperature on the bar, therefore limiting any possible damage. However, it is necessary to limit the effect of the anvils installation on the transmitted and reflected signals meaning that their mechanical deformation does not provide an artificial contribution to the sample response. Finite element simulations concerning this aspect have been carried out and their results presented in Section 7.2.3.

Pulse Shaping The crude impact between the striker and the input bar, in theory, generates a rectangular-shaped incident pulse. This step rising loading path is usually suitable to test metals because it imposes a fairly constant strain rate while they undergo plastic yielding. However, for the case of highly brittle materials, in which their nominally elastic behaviour up to failure is of most interest, the high energy content associated with the abrupt nature of the rectangular-shaped pulse might results in premature failure [71]. In turn, this implies that dynamic stress equilibrium might not be established within the specimen before failure occurs. Moreover, a sharp rising pulse leads to high frequency oscillations prior reaching the constant plateau because of the different wave phase velocities of the frequencies embedded in the spectrum. These issues can be overcome by employing a pulse shaper which consists of a dummy specimen placed between the striker and input bar. This topic has attracted the attention of several researchers who investigated the possibility to draw upon different designs, *i.e.* by varying geometry and material of the pulse shaper in order to obtain the desired incident pulse for the given material to test [72, 73, 74]. However, the choice of the proper pulse shaper requires an iterative optimization procedure consisting in experimental and numerical trials. Other methods to adjust the loading pulse were based on the use of pre-loaded bars or strikers with tapered sections.

Specimen Design A crucial role toward the accomplishment of a successful SHPB test is played by the choice of the specimen design. Several geometries have been adopted throughout the years and their limitations extensively discussed [75]. The different options usually refer to the use of dogbones, cylinders or miniaturized cubic samples; a summary of the different options used throughout the years has been provided by McCauley and Quinn [76] and reported in Figure 2.4. The main objectives

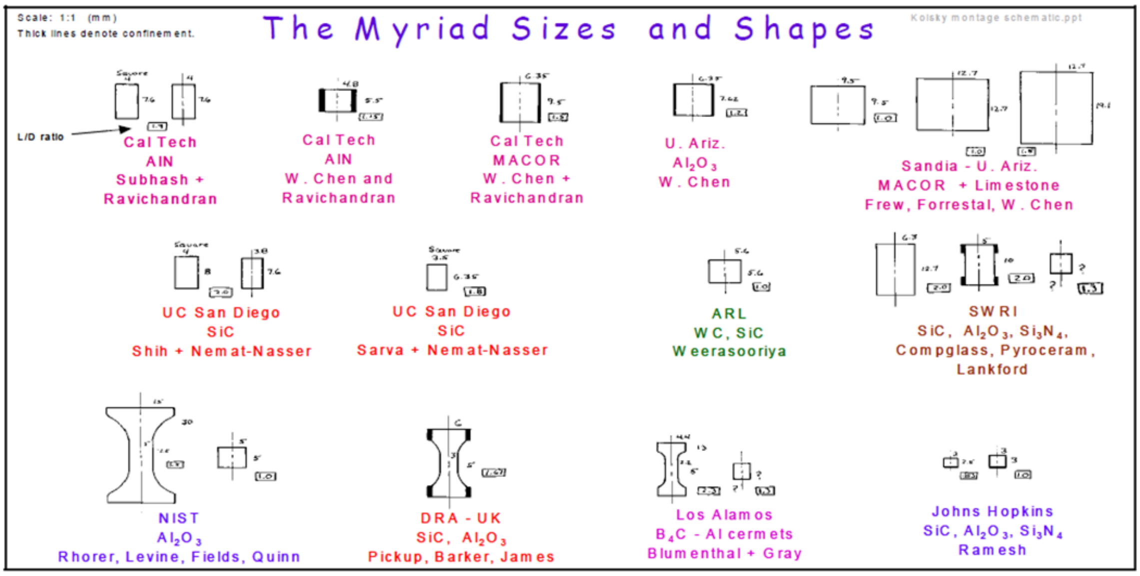

Figure 2.4: Schematic of different specimen geometries and dimensions for SHPB of ceramics

concern requirements to reduce the inertia-induced contributions associated with their finite size, minimal friction at the sample/bars interfaces as well as the evaluation of their manufacturing feasibility. The first requirement implies that the axial and radial inertia induced by particles acceleration within the specimen should represent a negligible portion of the actual stress flow in the material. Gorham [77] performed analytical derivations in order to study the effect of induced-inertia on cylindrical samples. In his work, it was demonstrated that the axial inertia appears in the form of higher order terms in the material flow stress expression and can be reduced if the following requirement on the ratio between specimen length and diameter is met:

$$0.5 \leq \frac{l_S}{d_S} \leq 0.1 \tag{2.21}$$

Davies and Hunter [68] proposed a more conservative expression in which the two opposite contributions of the axial and radial inertia are balanced by taking into account the Poisson's ratio of the material, ν_S:

$$\frac{l_S}{d_S} = \sqrt{\frac{3\nu_S}{4}} \tag{2.22}$$

Arguments along the same kind can also be used to estimate the bounds within which inertia effects in cubic samples under compression are theoretically eliminated. Tekalur and Sen [78] showed that the features of their characteristic cross-section have to be taken into account by considering the momentum of polar inertia, J. Their result is reported below:

$$1.4 \leq \frac{l_s}{\sqrt{\frac{J_S}{A_S}}} \leq 2.8 \tag{2.23}$$

Lu [79] showed how pressure dependent materials, such as ceramics, tested under multi-lateral confinement conditions, present a strain rate transition limit above which inertial effects become predominant Moreover, the chosen length of the specimen also regulates the maximum strain rate which can be attained in the material. If the density and distribution of critical flaws within the sample is the same, for a smaller gauge length (or thickness) it is possible to achieve an higher rate of strain prior to failure, $\dot{\varepsilon}_f$, estimated through:

$$\dot{\varepsilon}_f = \frac{\varepsilon_f c_S}{\alpha l_S} \tag{2.24}$$

Bertholf and Karnes [80] argued that a significant decrease in the specimen dimensions results in higher friction at the interface with the bars which in turn leads to artificially stiffened outputs from the strain gauge station. Follansbee [81] showed that friction can be minimized if the ratio between the length and the diameter of the specimen satisfies the constraint:

$$1.5 \leq \frac{l_S}{d_S} \leq 2 \tag{2.25}$$

This requirement is clearly in contrast with what reported in the inequalities 2.21 and 2.23 which assume that the measurement is friction free. However, interfacial friction seems to be more controllable by means of lubricants [82] as well as by improving the surface finish of the bars and sample which should be ideally asperities-free. A correction coefficient was proposed by Alves et. al. [83] based on analytical and numerical investigations of ductile rings under dynamic compression.

Another important issue is represented by the non-perfect parallelism of the faces of the specimen in contact with the bars. This is usually attributed to the difficulty of machining hard ceramics; non-perfect right-angle corners or round surfaces lead to a situation in which multi-axial loading acts on the material because of induced-bending.

Tracy suggested the use of dumb-bell-shaped specimen to test the uniaxial compression behaviour of different ceramics [84]. Although his original design was employed to perform quasi-static experiments, it was later used to also characterize ceramics under dynamic loading by means of the SHPB [85, 86]. Tracy observed that most of the specimens failed because of axial or radial cracks initiated close to end cups as a result of the several wave reflections occurring within the specimens; the stress distribution obtained by means of finite element calculations confirmed his observations. The use of the *dumb-bell-shaped* specimen presents some advantages as well as shortcomings which therefore make its use an ongoing open dispute. This design ensures a more gradual transmission of the stress wave when it reaches the bar/specimen interface which therefore leads to a more favourable condition to establish equilibrium within the material. However, different modes of failure could be registered because of the size effects associated with the choice of a specific feature of the geometry, i.e. fillet radius and cups dimensions. Moreover, the machining of such a sample is somehow still a challenge which requires different stages of abrasive grinding and high precision cutting. Furthermore, this manufacturing process increases the probability of introducing surface cracks, especially in the proximity of the cups, which affects the assessment of the mechanical response up to failure of the material.

In order to overcome this issue an extremely demanding polishing procedure is required to improve the quality of the surface finish. Another drawback associated with the use of the dumb-bell-shaped specimen concerns the measurement of the uniaxial strain. If the classical configuration with strain gauges mounted on the bars is used, the results might not be representative of the true material behaviour as registered in the gauge section of the specimen. The reflected stress wave signal is the result of an averaged response which, in this case, comprises the effect of the cups deformation as well [86]. An alternative way to obtain the strain history consists in mounting the strain gauges directly on the specimen surface. However, the high time consumption and the practical difficulties encountered during their installation lead to major drawbacks. The choice of a proper adhesive, which would not alter the signal measurement, involves non-trivial considerations along with the need to have an ad-hoc improved system of data acquisition, i.e. oscilloscope and amplifier.

Some researchers have suggested resorting on high speed imaging measurements, i.e. digital image correlation (DIC), which has shown potential success for measuring deformations in ductile metals [87]. However, performing full-field measurements in low-strain-to-failure brittle ceramics requires ultra-fast imaging sampling in order to capture the elastic limit of ceramics with very high wave propagation speed. Moreover, multi-cameras configurations are suggested to monitor the process of abrupt micro-cracking which could initiate in different locations of the material where the critical flaws exist. This implies that the view of a single plane in the tree-dimensional space does not provide enough accuracy regarding the time at which the material starts breaking. Moreover, efforts have to be made to improve the distribution of light around the sample in order to achieve the desired quality of the images; different strategies have to be adopted based on the transparency of the material.

2.5 Numerical Modelling

In the following a summary of constitutive models which have been developed to describe the rate-dependent failure of brittle materials is provided.

2.5.1 Phenomenological damage mechanics models

Continuum phenomenological models are based on classical damage mechanics in which the degradation of material strength due to damage evolution, associated with crack growth and coalescence, is described by a variable scalar parameter, D [88]. Among all, the models proposed by Johnson and Holmquist, (JH1-JH2) [89, 90], as well as that of Johnson et. al. [91] (JHB), have been extensively employed to simulate the failure response of brittle materials, such as ceramics [92, 93, 94], under impact loading conditions. In the following discussion a summary of the JH2 version is presented. The model accounts for progressive material softening as a result of damage evolution, *i.e.* $0 \leq D \leq 1$, which enables for a smooth interpolation of the current material strength, σ^* between the intact, σ_i^* and completely fractured, σ_f^* states:

$$\sigma^* = \sigma_i^* - D(\sigma_i^* - \sigma_f^*) \tag{2.26}$$

the superscript indicates that the quantities are normalized with respect to the Hugoniot elastic limit such that $\sigma^* = \sigma/\sigma_{HEL}$. The two strength-reference state obey a pressure-rate dependent Drucker-Prager [95] type of formulation:

$$\sigma_i^* = A(P^* + T^*)^N (1 + C\log(\dot{\varepsilon}^*)) \tag{2.27a}$$

$$\sigma_f^* = B(P^*)^M (1 + C\log(\dot{\varepsilon}^*)) \tag{2.27b}$$

In the above A, B, C, M and N are constants which have to be determined through a combined experimental-numerical calibration procedure. The normalized pressure and tensile strength have been defined with P^* and T^* respectively. In the spirit of an elastic-plastic constitutive response, the increment in the accumulated permanent strains within the element control volumes, $\Delta\varepsilon_p$, can be employed to obtain the current value of D through:

$$D = \frac{\Delta\varepsilon^P}{\varepsilon_f^P} \tag{2.28}$$

with the plastic strain at fracture under constant pressure defined as:

$$\varepsilon_f^P = D_1(P^* + T^*)^{D_2} \tag{2.29}$$

where D_1 and D_2 are constants to be calibrated. The pressure is calculated through:

$$P^* = \begin{cases} K_1\mu_1 + K_2\mu_1^2 + K_3\mu_1^3 + \Delta P & \mu \geq 0 \\ K_1\mu_1 + \Delta P & \mu_1 < 0 \end{cases} \tag{2.30}$$

where the measure of deformation is defined as the one resulting from an equation of state for the the density $\mu_1 = \rho/\rho_0 - 1$. The other material constants K_1 (bulk modulus), K_2 and K_3 have to be determined via experiments. Simha et. al. [96] proposed a modification in which the damage was calculated by means of the applied shear stress or principal stress for compression and tension respectively.

All these models require an extensive set of calibration parameters, which in turn implies the need for a demanding experimental campaign in support of an enhanced inverse modelling procedure. Even if a successful calibration is accomplished, the association of these constants to specific microstructural features and their physical interaction is hard to be found. Moreover, the framework is not built upon any requirement for thermodynamic consistency to describe the fracture nucleation mechanisms. The absence of any length scale or regularization often has resulted in a pronounced discretisation-dependency of the results. This has been somewhat addressed by Brannon et. al. [97] by proposing a revised-formulation in which the tensile strength is statistically perturbed.

2.5.2 Micro-mechanical models

Micro-mechanical models rely on employing classical fracture mechanics concepts combined with damage-type laws to describe the evolution of flaws density, *i.e.* growth and interaction of micro-cracks, which leads to material failure. Early approaches were based on averaging schemes in which the overall material response is calculated by means of homogenized elastic properties accounting for microstructural heterogeneities [99, 100]. Although brittle materials might present a wide range of types of defect nuclei, under compressive loading conditions, the material response can be represented by that one of a series of unit cells containing an isolated penny-shaped inclined crack with its surfaces subjected to frictional sliding [101, 102, 47, 103] as shown in

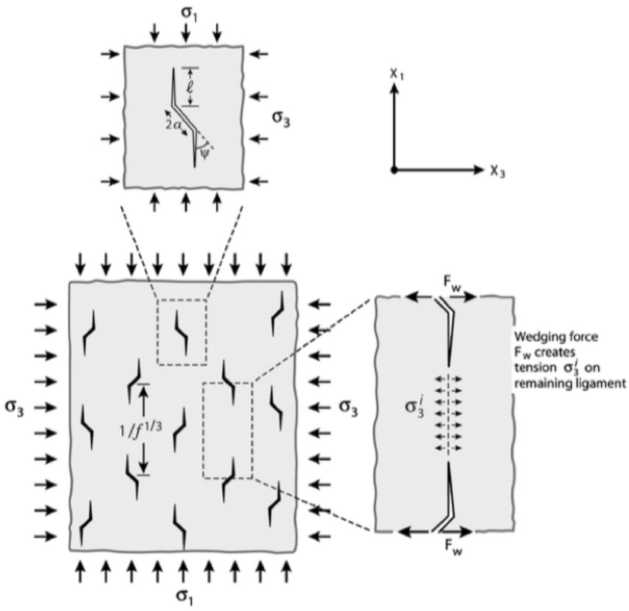

Figure 2.5: Schematic of wing-shaped micro-crack; reprinted from Deshpande and Evans [98]

Figure 2.5. The cracks grow starting from their tips and assume a wing shape with an angle of approximately 70^o [104] and further elongate in direction which maximize the mode-I stress intensity factor, K_I. As the load increases they tend to become straight and all aligned according to the direction of maximum principal compressive stress. However, the local crack-tip stress field also consists of tensile components that cause opening of the crack faces [102]. Several analytical and numerical works attempted to characterize the relative frictional sliding and interaction of both uniformly and randomly distributed populations of wing cracks under multi-axial remote loading conditions at different strain rates regimes [105, 106, 107, 108]. Nemat-Nasser and Deng [109] proposed a model in which the material strain rate dependency was expressed in terms of sensitivity of the crack-tip stress intensity factor upon the crack-tip velocity. Ravichandran and Subhash [110] did not include the effect of cracks interaction and assumed failure coincident with a critical value of cracks density. Huang et.

al. [111] followed closely the work on non-interacting pre-distributed cracks of Grady and Kipp [112] and assumed that material failure occurs when the rate of growth of damage approaches infinity. Paliwal and Ramesh [113] proposed a complex variables approach in which the contribution of the local stress fields associated with the mutual interaction of uniformly distributed cracks was taken into account [114, 115] to calculate the global damage evolution. Their results confirmed those previously obtained by Nemat-Nasser and Deng [109] in which it was shown that low flaws density leads to a lower limit for the strain rate dependent behaviour transition. Conversely, a higher flaw density favours mutual interaction for a lower extension of the crack wings, which in turn implies that the strain rate dependent behaviour transition occurs at higher strain rates and damage distributes more uniformly in the medium. Moreover, bigger flaws size results in a more pronounced accumulation of damage for relatively low strain rate loading conditions and in an overall decrease of the compressive strength at all the regimes. Deshpande and Evans [98] developed a three-dimensional model which generalizes the original work of Ashby and Sammis [108] for a distribution of randomly oriented wing cracks. In their model, the reduction of the elastic moduli is obtained from the evolution of the damage variable dictated by a crack growth law that employs stress intensity factor calculations. Given an expression for the Gibbs' free energy functional, the constitutive equations for the comminuted ceramic can be derived by recalling classical continuum thermodynamics arguments [116]. Their model included the effect of confining pressure which, based on the rate of loading, results in plastic deformation therefore assumed to be the driven mechanism for damage evolution. The fracture behaviour was divided into three regimes depending on the loading rate:

1. Quasi-static: the crack surfaces do not experience any relative sliding because the value of the applied load does not exceed the one required by the frictional resistance

2. Intermediate velocity: an increase in the remote load leads to nucleation and growth of wing cracks

3. High velocity: the stress field around the crack surfaces becomes predominantly tensile leading to crack opening.

Although most of the models summarized above succeed in describing the physic of the main fracture mechanisms, the crack growth laws are usually based on considering the crack-tip speed proportional to a power of the static crack-tip stress intensity factor according to Charles law [117]; however, this does not ensure that the material characteristics inherent to different loading rates are taken into account. Bhat et. al. [118] expanded the framework proposed by Deshpande and Evans [98] by employing a crack law which included the dynamic stress intensity factor. In their work, the fracture propagation initiation criterion was revised in order to take into account the effect of material inertia, which motivated the use of the critical dynamic stress intensity factor for initiation of crack propagation, K_{IC}^{D}. This implies that the time required to establish a K-dominant field in the proximity of the crack is assumed to be a rate dependent material property and can be related to the critical value at quasi-static loading conditions, K_{IC}^{SS}, through:

$$K_{IC}^{dyn} = f_D(\dot{K}_I) K_{IC} \tag{2.31a}$$

$$f_D(\dot{K}_I) = 1 + \left(\frac{\dot{K}_I}{K_{IC}}\right) * 2 * 10^{-5} \tag{2.31b}$$

Here $\dot{K}_I = \tilde{K}_{IC}/t_c$ is the parameter that characterizes the loading rate expressed through the ratio between the critical stress intensity factor at initiation of crack propagation, K_{IC}, and the time, t_c, required for the remote load, $P(t)$, to initiate crack propagation. Crack propagation was assumed to occur when the following condition on the dynamic stress intensity factor during propagation, $K_I^d(t)$, is met:

$$K_I^{dyn}(t) = K_I^{dyn}[l(t), v(t), P(t), t] = K_{IC}^{dyn}(v) \tag{2.32}$$

where

$$K_{IC}^{dyn} = K_{IC}\left(1 + \frac{(v/v_m)^5}{\sqrt{1-v/c}}\right) \tag{2.33}$$

Where, $l(t)$ is the current crack length and v_m is the branching speed, which has to be experimentally evaluated for each material. Although micromechanical-based models overcome some of the physical limitations of those based on phenomenological laws, they do not take into account any fracture nucleation mechanism. Moreover, they do not include the effect of cracks coalescence because failure is assumed to occur when cracks start interacting; similarly it can be argued that they suffer the interaction of complex three-dimensional crack patterns whose complexity weaken the numerical robustness.

2.5.3 Discrete interfaces-based models

Discrete approaches enable to explicitly account for the presence of discontinuities, *i.e.* cracks, in the material by employing special purposes interaction laws between elements boundaries based on cohesive zone models (CZM) [119, 120]. The path along which pre-existing defects are allocated and eventually evolve has to be designed a priori, which in turn requires a careful evaluation of the spatial discretisation strategy and consequent computational costs [121]. The interface response

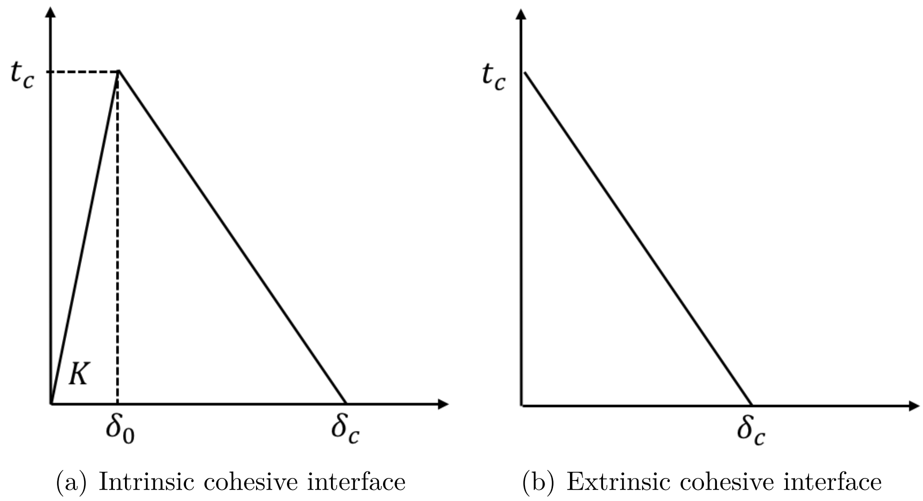

Figure 2.6: Elastic and initially rigid traction separation law

is usually described by a traction separation law (TSL), which relates the tractions, both normal and tangential, acting on the crack surfaces, to the correspondent displacement jump component. The TSL can be inferred by an appropriate choice of the interfacial potential [122] and designed such that additional complexities of the near-crack material behaviour, such as mode-mixity of failure and triaxiality conditions [123, 124] as well as rate dependency [125], are captured. Furthermore, attempts have been made towards including microscopic and thermo-mechanical effects within the description of the interface response [126, 127, 128]. CZMs are usually classified into two main types based on the shape of the TSL: intrinsic (or initially elastic) and extrinsic (or initially rigid) as respectively shown in Figure 2.6(a) and Figure 2.6(b) [129].

The cohesive interface starts softening when the critical value of the traction, t_c, is attained; when the crack surfaces are displaced apart of an amount equal to δ_c no more closure tractions act on the crack surfaces meaning that the total work for separation has been provided. The TSLs can also be distinguished between reversible and irreversible based on the way of designing the response for the case of unloading. The former implies that if unloading occurs the original state is recovered in a conservative-elastic fashion. The latter accounts for dissipated energy meaning that the tractions are ramped to zero directly from that point and any successive re-loading follows the unloading path. When an intrinsic model is employed, cohesive interfaces are usually placed in the material from the beginning and as the load increases their initial elastic response might contribute to the overall behaviour of the bulk. Relatively small values of K result in a loss of material stiffness, which in turn leads to a non-physical delay of the fracture propagation due to artificial decrease of the stress in the neighbour of the cohesive interface. Conversely, high values of K might cause an unrealistic increase in neighbour material elements stress leading to spurious cracking [130]. However, an effective design of the initial elastic loading path of the TSL can be achieved by estimating K as a scaled value of bulk Young's modulus with respect to the cohesive element characteristic length [131]. Early investigations on the use of intrinsic TSLs to simulate dynamic crack growth in brittle materials were carried out by Xu and Needleman [132, 133]. Espinoza et. al. [134] modelled a pre-defined distribution of different sizes of fragments; they used the multi-plane continuum model [135] to model the intra-fragment damage while a discrete contact-law, based on reversible intrinsic interfaces, which included thermal effects, was employed to simulate the inter-fragment failure. Their approach was strongly based on the experimental evidences of Espinosa and Brar [136] which showed that several grains can be grouped into one single larger fragment. They assumed that micro-cracks develop inside the grain and their coalescence does not lead to a macro-crack that propagates towards the fragment boundary. The same approach was employed to study the response of ceramic microstructures, generated by means of Voronoi tessellation, under multi-axial loading conditions and with stochastic distribution of grains orientation and flaws [137, 138]; in these two works an irreversible intrinsic TSL was used instead. Along the same lines, Nittur et. al [139] studied fragmentation in confined ceramic microstructures in which the nonlinear contribution due to intergranular friction as well as brittle to ductile transition due to suppression of lateral dilation was taken into account. As far as initially rigid cohesive elements are concerned, they do not populate the initial topology of the model, instead they are adaptively inserted according to a fracture-based criterion, *i.e.* the tensile strength, defined for the bulk material. The facets of the critical element are enriched with cohesive elements created by duplicating the nodes shared with the neighbour elements. They are more suitable for conditions in which the physical interface representing the crack path has a negligible elastic contribution compared to the characteristic length of any element in the model. Approaches based on initially rigid element were proposed by Camacho and Ortiz [140, 141] to simulate the fragmentation of brittle material subjected to dynamic loading conditions; in their study mixed mode interface behaviour has been addressed by introducing a weighting parameter between the normal and tangential displacement jumps. Later, Ortiz and Pandolfi along with other co-workers [142, 143, 144] expanded the original approach in order to simulate complex three-dimensional crack patterns. Zhang et. al. [145] followed closely this approach to study branching instability due to micro-cracking in brittle materials on the basis of the experimental observations reported by Ravi-Chandar and Yang [146]. Furthermore, extrinsic TSLs were employed to investigate the effect of microstructural properties distribution, i.e.

grain boundary configuration and cohesive strength, on the dynamic response of polycrystalline ceramics by Kraft et. al. [147, 148]. The sensitivity of one-dimensional dynamic fragmentation on the strain rate and on the flaw size has been investigated by means of initially rigid irreversible cohesive elements by Zhou et. al. [125]; later, Levy and Molinari [149] also accounted for the effect of defects distribution on the statistic of fragments generation in an expanding ring subjected to a dynamic radial pulse.

Despite the remarkable successes in the simulation of dynamic failure and fragmentation of brittle-like materials, it has been argued that initially rigid cohesive elements suffer numerical instability, if unloading occurs at the early stage, because the stiffness ideally tends to infinity, as well time discontinuities and traction locking effects [150]. Besides the numerical difficulties discussed above, one of the main drawbacks encountered in using cohesive-type approaches is that they are based on phenomenological laws, therefore implying that an extensive set of calibration efforts is required to adopt meaningful parameters in the TSL.

Chapter 3

State of the art: phase field theories

In this chapter the fundamentals of phase field theories for the description of fracture are reviewed. The framework of diffusive interfaces, upon which the derivation of the governing equation is based, is presented along with a comparative summary of the existing models reported in the literature.

3.1 Introduction

Phase-field models are based on the idea that sharp interfaces, associated with material heterogeneities such as a crack, can be described by a smooth, *i.e* diffusive, continuous field which maps the evolution of an order parameter, ϕ, between to reference states, *i.e.* intact material and fully developed crack. A schematic representation of this concept as applied to a general medium, Ω, containing a set of discrete interfaces Γ, is presented in Figure 3.1. The solution is regularized within a diffusive zone which has width $2l_0$. In contrast to approaches based on discrete interfaces, such the cohesive zone models and the extended finite element method, the crack is not explicitly introduced in the domain topology and there is no need for ad-hoc criteria to predict crack nucleation and propagation; the evolution of the phase field is naturally predicted as the solution of the governing equations. Although it does not fall within the scope of this work, it has to be noted that phase field models have been also largely employed in the material science community to model phase transformation and microsctructural evolution. In these models each phase/variant is described by an order parameter whose evolution is governed by a Landau-Ginzburg type of equation [151]. Some early works on phase field models for fracture have relied on

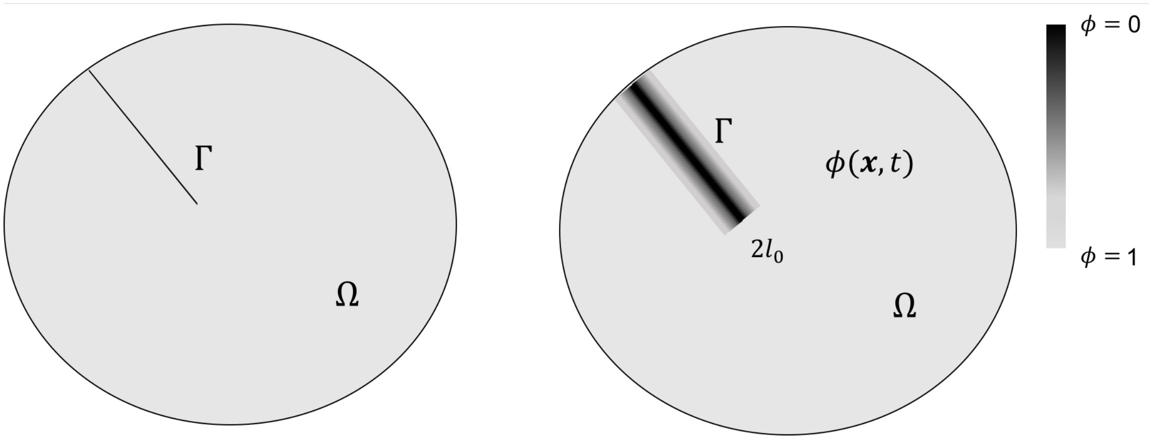

Figure 3.1: Schematic representation of phase field-based diffusive fracture

these types of formulation in contrast to those based on the regularized-variational approach as originally proposed by Francfort and Marigo [152] and Bourdin et. al. [153]. A review of some of the models concerning both approaches is provided in the following sections, along the lines of what presented in a recent paper by Ambati et. al. [154]. It has to be pointed out that the choice of how to define the correspondence between the two reference states and the bounds for ϕ varies among the models, although without changing the nature of solution. In the following it will be assumed that $\phi = 1$ and $\phi = 0$ correspond to intact and completely fractured materials, unless stated otherwise. Moreover, the deformation will be described in terms of the small strain tensor ε.

3.2 Models based on Landau-Ginzburg equation

One of the first attempt in applying phase field theories to model fracture by employing Landau-Ginzburg evolution equations [151] was proposed by Aranson et. al. [155]. In their model the classical elastodynamic equation is enriched by a damping term , η:

$$\rho \ddot{u}_i = \eta \Delta \dot{u}_i + \frac{\partial \sigma_{ij}}{\partial x_j} \tag{3.1}$$

$$\sigma_{ij} = \frac{E}{1+\nu}\left(\varepsilon_{ij} + \frac{\nu}{1-\nu}\varepsilon_{ii}\delta_{ij}\right) + \kappa\dot{\phi}\delta_{ij} \tag{3.2}$$

In the above E represents an effective stiffness which takes into account degradation due to phase field evolution and is defined as $E = E_0\phi$. In the constitutive equation 3.2 the term $\sim \kappa\dot{\phi}$ takes into account the effect of hydrostatic pressure resulting from crack formation only, *i.e.* excluding the effects associated with thermal expansion. This formulation was based on the argument provided by Fuller et. al. [156] that thermal equilibrium at the crack tip cannot be ensured. The evolution of the phase field evolution is obtained by postulating that the variational differentiation of a given free-energy functional, $\mathscr{F}$, relates to the rate of ϕ:

$$\dot{\phi} = \frac{\delta \mathscr{F}}{\delta \phi} \tag{3.3}$$

where $\mathscr{F}$ is adopted from the work of Landau [151] and is defined below:

$$\mathscr{F} \sim \int_{\Omega} P(\phi) + D_{\phi}|\nabla\phi|^2 d\Omega \tag{3.4}$$

The choice of the function P is dictated by the requirement that its minima are at $\phi = 0$ and $\phi = 1$. Adopting a generic polynomial form for P leads to the following evolution equation:

$$\dot{\phi} = D_\phi \Delta\phi - a_1\phi(1-\phi)F(\phi,\varepsilon_{ii}) + f(\phi)\frac{\partial\phi}{\partial x_i}\dot{u}_i \tag{3.5a}$$

$$F = 1-(b-\mu_1\varepsilon_{ii})\phi \tag{3.5b}$$

$$f(\phi) = c_1\phi(1-\phi) \tag{3.5c}$$

In the equation above the function $F(\phi,\varepsilon_{ii})$ provides the coupling between the phase field parameter and the mechanical solution. Its postulation relies upon the requirement that a zero, within the interpolation interval, has to exist at a critical value ϕ_c and its variation with respect to ϕ decreases monotonically, *i.e.* $\partial_\phi F(\phi=\phi_c,\varepsilon_{ii}) < 0$. Moreover, this form guarantees that crack evolution affects only the material under hydrostatic state of stress, however without distinction between tension and compression. The function $f(\phi)$ can be thought to be the so-called "double-well" potential whose minima are at $\phi=0$ and $\phi=1$. It was argued that this function has to act on the material velocity in order to retain the strain localization effect due to material motion. The model requires the calibration of the numerical parameters D, a_1, b and μ with the last two associated with fracture properties. The regularization length scale is embedded in the non-dimensional parameter c_1. The model was applied to simulate crack propagation in pre-notched rectangular strip under remote tensile loading conditions. Although novel at the time it was introduced, the model presented few limitations mostly due to the difficulties in linking physical aspect of fracture to the calibration parameters necessary to formulate the polynomial function P.

Later Karma et. al. [157] proposed a model along the same lines for the studying crack propagation under mode-III loading conditions which was subsequently extended to the three-dimensional case by Hakim and Karma [158]. Conversely than the original mode proposed by Aranson [155] the governing equations and constitutive relations have been derived by performing variational differentiation on a given free energy functional $F(\phi,\varepsilon_{ij})$ postulated as below:

$$F(\phi,\varepsilon_{ij}) = \int_{\Omega} g(\phi)\Big(\psi_0(\varepsilon_{ij}) - \psi_c\Big) + V(\phi) + \frac{1}{2}D_{\phi}|\nabla\phi|^2\Big)d\Omega \tag{3.6}$$

Few elements differ from the the original formulation of Aranson [155] and are highlighted in the following discussion. The function in equation 3.6 is constructed such that a reference form for the strain energy, ψ_0 is explicitly introduce. The coupling of the mechanical solution with the phase field is established through the function $g(\phi)$ which acts on the *effective* strain energy resulting from the evaluation against a threshold value ψ_c. This new feature, has allowed to obtain linear elastic response in a nominally brittle-sense with negligible phase field evolution prior reaching the critical threshold ψ_c. The function, $g(\phi)$, often referred as a damage function, is assumed to have a polynomial form of the type

$$g(\phi) = \sum_{\alpha=n}^{0} = s(\alpha_n\phi^{2+\alpha} + \alpha_{n-1}\phi^{2+\alpha-1}...).$$

So far the only requirement is that it is formulated such that $g(\phi) \to 0$ as $\phi \to 0$. The constant s assumes small values. A more detailed examination of the effect of this function on the solution will be provided in the next chapter. The term $V(\phi)$ represents the double-well potential and it is assumed to have the form:

$$V(\phi) = \frac{\phi^2(1-\phi)^2}{4} \tag{3.7}$$

this form ensures that the bulk state is bounded by the two minima $\phi = 1$ and $\phi = 0$. The contribution associated with the Laplacian term is scaled by a constant D_{ϕ} as in the model by Aranson et. al. [155]. By performing variational derivation on the functional $F(\phi, \varepsilon_{ij})$ with respect to the mechanical variable, a constitutive law for the stress can be obtained as:

$$\sigma_{ij} = g(\phi)\frac{\partial \psi_0(\varepsilon_{ij})}{\partial \varepsilon_{ij}} \tag{3.8}$$

The evolution of the phase field parameter is governed by a nonlinear diffusion equation with constant kinetic modulus, τ, or mobility as called in the context of phase field models for solidification, which leads to:

$$\tau\dot{\phi} = D_{\phi}\Delta\phi - V'(\phi) - g'(\phi)(\psi_0(\varepsilon_{ij}) - \psi_c) \tag{3.9}$$

Later, Henry and Lavine [159] applied a similar model to study crack propagation under biaxial loading conditions. In their work a modified formulation for the elastic reference energy was proposed:

$$\tilde{\psi}(\varepsilon) = \begin{cases} \psi_0(\varepsilon_{ij}), & \varepsilon_{ii} > 0 \\ \psi_0(\varepsilon_{ij}) - \frac{1}{2}\alpha K(\varepsilon_{ii})^2, & \varepsilon_{ii} < 0 \end{cases}$$

In the above a symmetry breaking feature is introduced for the case of pure compression with a scaling parameter, α acting on the deviatoric part of the strain energy. The bulk modulus is indicated with K.

Although this class of model has presented early successes in qualitatively capturing the configuration of crack pattern under dynamic fracture, their reliability is largely based on the calibration of the scaling parameters and on the postulation for the form of the double-well potential. Another approach for the derivation of the governing equations based on a variational formulation is reviewed in the following section.

3.3 Models based on variational approach

In the following a class of phase field models based on the *variational formulation of brittle fracture* as originally proposed by Francfort and Marigo [152], is reviewed. The fracture problem is therefore revised in terms of a minimization problem of a given energy functional, ψ, which includes the contributions associated with the elastic energy of the body, Ω, as well as the one related to the fracture process zone. The solution is sought such that the system finds its equilibrium in a state of minimum energy. Although this procedure does not necessarily find a solid connection with any thermodynamics requirement, it has been proven to be a useful postulate in describing several material processes such as austenitic-martensitic phase transformation [160] and damage evolution [161]. A generic form can be expressed as:

$$\psi(\varepsilon_{ij}, \Gamma) = \int_{\Omega} \psi_0(\varepsilon_{ij}) d\Omega + G_c \int_{\Gamma} ds \tag{3.10}$$

In the above ψ_0 is the reference elastic strain energy of the unfractured solid which is required to have a p-homogeneous, convex form without restriction to nonlinear cases. The critical energy release rate for crack initiation and propagation is indicated with G_c and is related to a subset of discrete cracks $\Gamma \subset \Omega$. In the regularization setting proposed by Bourdin et. al. [153, 162, 163] this functional can be further approximated as:

$$\psi(\varepsilon_{ij}, \phi) = \int_{\Omega} (g(\phi)\psi_0^{+}(\varepsilon_{ij}) - \psi_0^{-}) d\Omega + G_c \int_{\Omega} \Gamma_{\phi,2} d\Omega \tag{3.11a}$$

$$\Gamma_{\phi,2} = \left(\frac{1}{4l_0}(1-\phi^2) + l_0 |\nabla \phi|^2 \right) \tag{3.11b}$$

This framework has been adopted in a series of studies devoted to the investigation of dynamic fracture in nominally brittle materials [164, 165, 166, 167, 168] and the details are now discussed.

A functional associated with the fracture energy, $\Gamma_{\phi,2}$ has been introduced. Therefore, the fracture process is now described by a diffusive field with thickness which smears out locally the original sharp configuration over a region of thickness l_0. This convention varies from model to model as some of them assume l_0 to be the semi-thickness. This change would only reflect on the definition of the functional $\Gamma_{\phi,2}$. A scalar phase field parameter, $\phi(\mathbf{X},t)$, describes the continuous-smooth interpolation between the intact state, $\phi(\mathbf{X},t)=1$, and the fully fractured state, $\phi(\mathbf{X},t)=0$. This form for $\Gamma_{\phi,2}$ has been originally used in the context of image segmentation by Mumford and Shah [169] and later proposed in the context of variational mechanics by Ambrosio and Tortorelli [170]. This particular choice satisfies the requirement for Γ-*convergence* [171] meaning that for vanishing length scale l_0 the sharp crack setting is recovered and the dissipation due to fracture reduces to G_c as in the Griffth approach [172]. The second term is associated with a laplacian operator acting on ϕ which highlights the diffusive nature of the solution and the intrinsic ability of the framework to include higher order effects due to spatial variation similarly to strain-gradient based damage models [173]. A higher order formulation has been proposed by Bordern et.al [174], although its compliance with the Γ-*convergence* theorem is yet to be proven. The recovery of the sharp-crack limit setting for vanishing length scale has been also proven by means of matched asymptotic analysis for both the quasi-static and dynamic cases by Hakim and Karma [158] and da Silva et al. [175]. In particular, in the latter it has been shown that the configurational momentum balance at the moving crack-tip, as referred to the two-dimensional sharp-crack setting proposed by Gurtin and Podio-Guidugli [176], naturally arises within the context of phase field theories.

As in the model proposed by Karma et. al. [157] a damage function $g(\phi)$ is included in order to drive the degradation of the solid as the phase field parameter evolves. In the work of Bourdin et. al. [153] the following form was proposed similarly to the one used by Karma et. al. [157]:

$$g(\phi) = \phi^2 + \kappa_1 \tag{3.12}$$

the positive constant $\kappa_1 \ll 1$ provides a small residual stiffness to avoid ill-posedness of the solution as introduced by Ambrosio and Tortorelli [177]. Although this parameter has been employed in several studies [178, 179, 180, 181, 182, 183, 184] Braides [185] pointed out that Γ-convergence can be recovered even if it κ_1 is not included.

In order to ensure that ϕ does not evolve as a result of pure compression, Miehe et. al. [165] have proposed a tensile/compressive split of ψ_0:

$$\psi_0(\varepsilon_{ij}) = \psi_0^+(\varepsilon_{ij}) + \psi_0^-(\varepsilon_{ij}) \tag{3.13}$$

The two contribution can be calculated by means of a polar decomposition of the strain tensor and expressed in terms of its principal components:

$$\psi_0^\pm(\varepsilon_{ij}) := \lambda\langle\varepsilon_1 + \varepsilon_2 + \varepsilon_3\rangle_\pm^2/2 + \mu(\langle\varepsilon_1\rangle_\pm^2 + \langle\varepsilon_2\rangle_\pm^2 + \langle\varepsilon_3\rangle_\pm^2) \tag{3.14}$$

In the above λ and μ are the Lamé constants. It can be seen that the split between the two counterparts is achieved by employing two ramp functions $\langle x\rangle_+ := (|x| + x)/2$ and $\langle x\rangle_- := (|x| - x)/2$. The constitutive relations and the evolution equation for ϕ are derived in an Euler-sense by performing the variational derivatives with respect to ε_{ij} and ϕ on the functional in equation 3.11 and assume the following explicit form:

$$\frac{\partial \sigma_{ij}}{\partial x_j} = \rho \ddot{u}_i \tag{3.15a}$$

$$\left(\frac{4l_0(1-\kappa_1)\psi_0^+}{G_c} + 1\right)\phi - 4l_0^2 \frac{\partial^2 \phi}{\partial x_i^2} = 1 \tag{3.15b}$$

where the stress is defined as:

$$\sigma_{ij} = g(\phi)\frac{\partial \psi_0^+}{\partial \varepsilon_{ij}} + \frac{\partial \psi_0^-}{\partial \varepsilon_{ij}} \tag{3.16}$$

It has to be pointed out that, in most of these formulations ϕ is regarded as being a non-reversible quantity as it would be in more classical damage mechanics-sense. It has been therefore argued that thermodynamics consistency is ensured if a condition of monotonicity exists for the crack functional, *i.e.* $\Gamma(t) \subseteq \Gamma(t+\Delta t)$. Without other sources of dissipation this can be achieved by enforcing $\dot{\phi} \geq 0$. This further implies that the only energetic driving term, Φ_0^+, in equation 3.19b, has to grow and do not diminish in the case of unloading. Therefore, Miehe et. al. [186] proposed a formulation based on the so-called *operator-splits*. In particular, the considerations above have led to the definition of a *history strain energy functional*, H, which is defined according to the satisfaction of a set of Kuhn-Tucker conditions:

$$\psi_0^+ - H \leq 0, \quad \dot{H} \geq 0, \quad \dot{H}(\psi_0^+ - H) = 0 \tag{3.17}$$

These conditions can be further reduced to:

$$H = \begin{cases} \psi_0^+(\varepsilon_{ij}), & \psi_0^+(\varepsilon_{ij}) > H_n \\ H_n, & otherwise \end{cases}$$

where the subscript n refers to the stage of loading/unloading. The governing equations can be therefore rewritten as:

$$\frac{\partial \sigma_{ij}}{\partial x_j} = \rho \ddot{u}_i \tag{3.18a}$$

$$\left(\frac{4l_0(1-\kappa_1)H}{G_c}+1\right)\phi - 4l_0^2\frac{\partial^2\phi}{\partial x_i^2} = 1 \tag{3.18b}$$

In the spirit of the formulation proposed by Karma et. al. [157] Miehe et. al. [187] suggested that H (or ψ_0^+) can be thought as a driving force for phase field evolution and can be subjected to a transition rule based on a threshold. The employment of this formulation, however brings other benefits from the numerical implementation stand point of view which shall be now discussed.

The two governing equations 3.19, consist in a hyperbolic PDE for the linear momentum balance in which a non-zero inertia contribution has been considered (3.19a) coupled with an elliptic PDE for the evolution of phase field parameter (3.19b). This form suggests that a fully non-linear numerical implementation based on implicit Newton-Rapson algorithm is necessary in order to solve concurrently for the two system variables. However, this involves a difficult numerical treatment of the problem when highly non-linear conditions arise as in the case of dynamic loading. A way to overcome these difficulties is by employing a staggered algorithm which exploits the operator split procedure discussed earlier. The linear momentum equation is solved first and ψ_0^+ is calculated and compared against the stored strain energy functional H. Upon verification of the Kuhn-Tucker conditions (3.17) the phase field equation is then solved with either implicit or semi-implicit numerical integration schemes [154]. This two-steps procedure underlines a framework in which the two equations are numerically decoupled whilst maintaining the coupling in the physics.

A somewhat different approach has been proposed by Hofacker and Miehe [188] in which the Euler equations of the system have been derived from the *rate potential functional* equipped with an additional term associated with a *viscous extended* *dissipation functional.* This resulted in a slightly modified version of the equations which included the explicit dependency on the rate of the phase field parameter, $\dot{\phi}$. By inverting the convention of the fracture reference states, *i.e.* $\phi = 1 - \phi$ and on the width of the regularization zone, *i.e.* $l_0 = l_0/2$ as assumed in all the works by Miehe and co-workers the resulting equations proposed by Hofacker and Miehe [188], for the case of $\kappa_1 = 0$, reads as:

$$\frac{\partial \sigma_{ij}}{\partial x_j} = \rho \ddot{u}_i \tag{3.19a}$$

$$2(1-\phi)H - \frac{G_c}{l_0}\phi - G_c l_0 \frac{\partial^2 \phi}{\partial x_i^2} = \eta \dot{\phi} \tag{3.19b}$$

The constant η resembles the role of a viscosity term which is responsible for rate-dependent behaviour in the phase field evolution. However, a calibration for this contribution has not been provided although it has been shown that its variation affects the solution patterns.

Extensions of this type of phase field to ductile fracture and shear band formation has been also considered recently [189, 190, 191, 192, 193, 194], along with its suitability to study fracture under multiphysics conditions [195, 196].

Chapter 4

A thermodynamically-consistent rate-pressure-dependent phase field model for fracture

In this section, a formal description of the thermodynamics framework used to derive the governing equations and the constitutive relations is provided. The numerical implementation within an updated Lagrangian finite framework with explicit time integration is presented. Results pertaining the model response under various uniaxial loading conditions are examined along with a proposed scaling law for the newly-introduced length scale associated with micro-inertia effects.

4.1 Summary of contributions

The model proposed in this thesis expands upon those reviewed in the previous chapter with the aim of providing the following novel contributions:

- The phase field description of the brittle fracture process in enriched by the contribution associated with crack-tip inertia as discussed in chapter 2.2. This feature is included by defining a rate-dependent length scale which describes the region within which these effects arise.

- Previous models have focused on describing brittle failure which occurs predominantly in a single mode fashion, predominantly by mode-I fracture. In the newly-proposed model a scaling law, based on the material triaxiality, for the critical energy release rate for crack propagation is proposed to capture rate-dependent mode-of-failure transition.

- The framework developed in this work has enabled for a fully explicit time integration within a finite element scheme.

4.2 Diffusive interfaces

A schematic representation of a generic boundary value problem for a medium Ω subjected to both Neumann, $\partial\Omega_{n_i}$, and Dirichlet, $\partial\Omega_{d_i}$, boundary conditions is presented in Figure 4.1. The set, Γ, of discrete interfaces associated with the presence of a crack (top-left figure) is replaced by a diffusive field with total thickness $2l_0$ (top right figure) which smears out locally the original sharp configuration. A scalar phase field parameter, $\phi(\mathbf{X},t)$, describes the continuous-smooth interpolation between the intact state, $\phi(\mathbf{X},t) = 0$, and the fully fractured state, $\phi(\mathbf{X},t) = 1$. In this work the diffusive field setting is enriched of a new length scale, named l, which is assumed to resolve the spatial distribution of the inertia effects within the zone of localization (bottom figure). In this zone the phase field parameter evolution can be thought to follow an oscillatory path under high rate regimes. It is assumed that these effects extend within a region up to the thickness of the diffusive field, $2l_0$, associated with the overall macroscopic damage localization.

The following energy functional is assumed to describe the state of the medium;

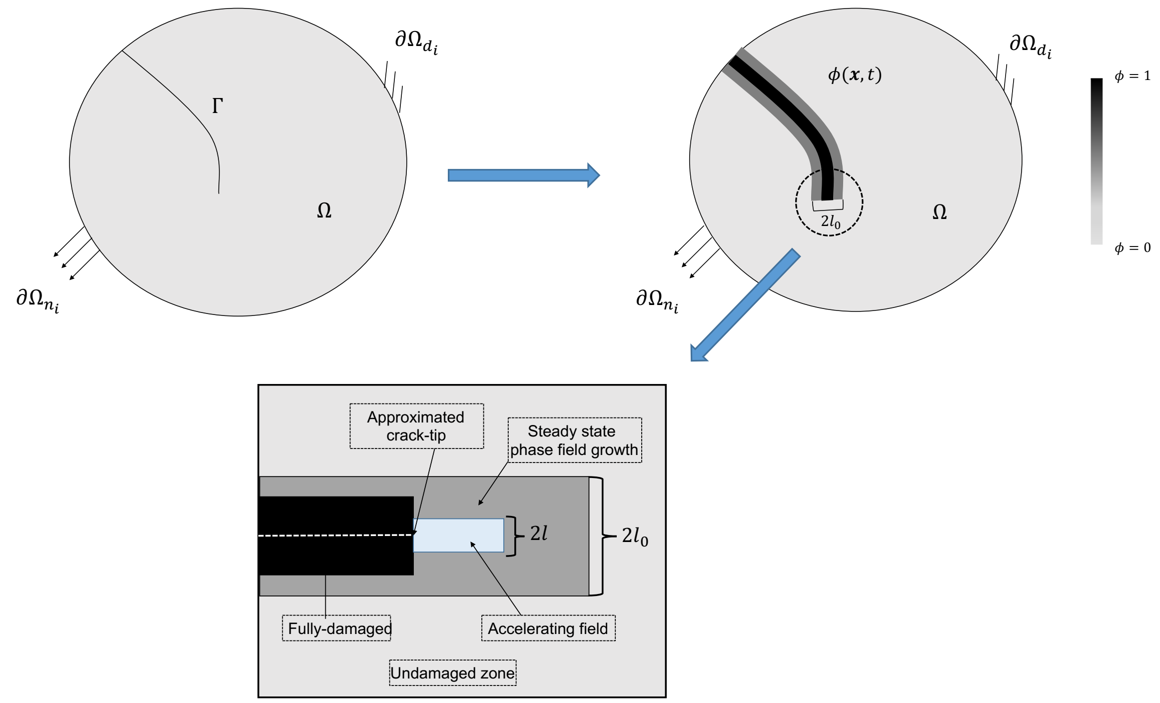

Figure 4.1: Schematic representation of embedded micro-inertia zone

standard indexed Einstein notation is used for all the tensorial quantities.

$$\psi = g(\phi)\psi^0_{F,a} + \psi^0_{F,p} + \Gamma_{\phi,2} \tag{4.1}$$

its terms are now discussed separately. In the proposed model formulation, the mechanical deformation is expressed in term of the deformation gradient F. The function $g(\phi)$ couples the evolution of the phase field parameter with the mechanical state of the medium, therefore resulting in material degradation leading to fracture. The quantities $\psi^0_{F,a}$, $\psi^0_{F,p}$ are the active and the passive counterparts of the reference strain energy for the intact material, respectively. The distinction between the two refers to the requirement that $g(\phi)$ should act upon only selected, physically-based components of deformation. In order to avoid unphysical occurrence of fracture under states of pure compression, a split based on decoupling volumetric, $\psi^h_0(F_{ij})$, and deviatoric, $\psi^d_0(F_{ij})$ contributions is adopted, as suggested by Amor et. al. [197] leading to the following definition for the active and *passive* contributions.

$$\psi^0_{F,a} = (\langle \psi_0^{h^+}(F_{ij})\rangle + \psi_0^d(F_{ij})) \tag{4.2a}$$

$$\psi^0_{F,p} = \psi_0^{h^-}(F_{ij}) \tag{4.2b}$$

The volumetric counterparts have been further divided into active, $\psi_0^{h^+}(F_{ij})$, and passive, $\psi_0^{h^-}(F_{ij})$, contribution which respectively refer to a state of positive and negative hydrostatic stress. This distinction can be formally described by using of the Macaulay brackets:

$$\langle \psi_0^{h^+}(F_{ij})\rangle = \begin{cases} \psi_0^{h^+}(F_{ij}), & \psi_0^h(F_{ij}) > 0 \\ 0, & \psi_0^h(F_{ij}) \leq 0 \end{cases}$$

Other approaches relied on an energy split based on a polar decomposition of the deformation tensor which equivalently ensures that degradation of material occurs only under tension [186]. The energy contribution associated with the diffusive evolution of the phase field parameter has been indicated with $\Gamma_{\phi,2}$. A second order formulation in ϕ will be used in the derivations which will follow:

$$\Gamma_{\phi,2} = \tilde{G}_c \left[\frac{1}{2l_0}\phi^2 + \frac{l_0}{2}|\nabla \phi^{\mathbf{X}}|^2 \right] \tag{4.3}$$

Here $\tilde{G}_c$ is a function associated with the critical energy release rate for crack propagation and its form will be explained shortly. This form for $\Gamma_{\phi,2}$ has been originally used in the context of fracture by Francfort and Marigo [152] and Bourdin et al. [163, 153, 162]. As previously discussed, this particular choice satisfies the requirement for Γ-*convergence* meaning that for vanishing length scale l_0 the sharp crack setting is recovered and the dissipation due to fracture reduces to $\tilde{G}_c$ as in the Griffth approach.

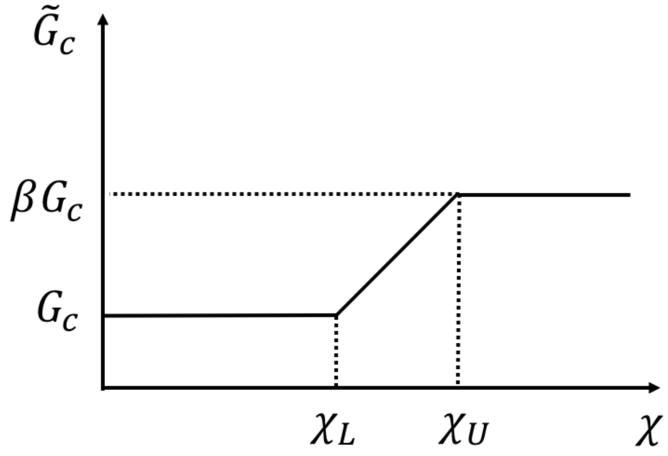

Figure 4.2: Schematic representation of mode of fracture transition trilinear law

4.3 Mode of fracture transition law

In this work the functional associated with the diffusive interface describing the phase field evolution is enriched with an adaptive critical energy release rate which depends upon the local state of triaxiality, χ, of the solid. This modification to previous models aims to capture the failure mode-transition which has been observed in brittle materials under high level of confinement as well increasing loading rates. This feature of the model has been postulated on the basis of experimental findings [198, 44] which have shown that a transition from predominantly extension fracture, mode-I, to shear-driven fracture, mode-II, occurs in brittle materials as the confining pressure increases. It has to be pointed out that no-plastic deformations are considered in this work and the effect of triaxiality has to be intended only in terms of condition for mode of fracture transition. A simple interpretation of what reported by Ramsey [198] resulted in assuming a tri-linear law to scale $\tilde{G}$ with the triaxiality; a schematic representation of this law is presented in Figure 4.2 where the triaxiality is calculated as:

$$\chi = -\frac{p}{\sigma^{eff}} \tag{4.4}$$

where p and σ^{eff} are the current hydrostatic pressure and Mises' stress defined in terms of principal components, σ_1, σ_2 and σ_3 as below:

$$p = \frac{\sigma_1 + \sigma_2 + \sigma_3}{3} \tag{4.5a}$$

$$\sigma^{eff} = \sqrt{\frac{1}{2}(\sigma_1 - \sigma_2)^2 + (\sigma_2 - \sigma_3)^2 + (\sigma_3 - \sigma_1)^2} \tag{4.5b}$$

The critical energy release rate for crack propagation under mode-I loading is indicated with G_c while β refers to the ratio between the critical energy release rate for crack propagation under mode-II and mode-I. Moreover, the two parameters χ_L and χ_U are associated with two bounds for the triaxiality within which a linear transition between mode-I and mode-II occurs. This law can be formally written as:

$$\tilde{G}(\chi) = \begin{cases} G_c, & \text{for } \chi \leq \chi_L \\ G_c + (\chi - \chi_L)\frac{(\beta-1)G_c}{\chi_U - \chi_L}, & \text{for } \chi_L < \chi < \chi_U \\ \beta G_c, & \text{for } \chi \geq \chi_U \end{cases} \tag{4.6}$$

Moreover, the proposed transition law allows to scale the crack resistance force accordingly when the deformation is driven solely by the deviatoric component of the reference strain energy. This feature compensates for the fact that the regularization zone, l_0, is usually chosen such that the resulting critical material stress corresponds to the tensile strength. Hence, the parameter β allows to re-scale critical fracture quantities such as, G_c, so that the critical stress resembles failure conditions under pure compression.

4.4 Thermodynamically-consistent derivation of the model and implementation

In the following, derivations of the governing equations and constitutive relations within the framework of continuum thermodynamics are reported. In this work a micro-force balance approach as firstly introduced by Fried and Gurtin [199, 200, 201] in the context of phase transitions, is used. Therefore, the phase field parameter is interpreted as a kinematical descriptor supplemented by its associated balance law. The chosen framework differs from other models in which a variational approach was used to derive the Euler equations of the system starting from a suitable choice of the energy functional such as the one assumed in equation 4.1.

Two fundamental balance laws are postulated as reported in equation 4.7 in their local version:

$$P_{ij,j} + B_i = \rho \ddot{U}_i \tag{4.7a}$$

$$\xi_{i,j} + \pi + \gamma = \rho l^2 \ddot{\phi} \tag{4.7b}$$

The equation in 4.7a refers to the standard linear momentum balance, where P_{ij} , B_i, ρ, $\ddot{U}_i$ are the first Piola-Kirchhoff stress, the body force, material density and material point acceleration, respectively. The micro-force balance is presented in equation 4.7b with ξ_i, π, γ defined as the corresponding micro-stress, internal micro-force and external micro-force, respectively. The newly introduced length scale, l, acts on the phase field parameter acceleration, $\ddot{\phi}$, whose evolution departs from steady-state conditions. In general, it can be assumed that the growth of this quantity obeys a rate-dependent law, here formally expressed as a function of the effective rate of deformation, $\dot{F}$:

$$l = \tilde{l}(\dot{F}) \tag{4.8}$$

where $\dot{F} = \sqrt{\frac{2}{3}\dot{F}_{ij}\dot{F}_{ij}}$. It is conceived that this law can be inferred either from the results of in-situ experimental measurements or numerically calibrated as shown in the next section. It has to be mentioned that a micro-inertia contribution was also considered in the pioneering work of Capriz [202] and Goodman and Cowin [203] in which a theory to describe the behaviour of solids with embedded heterogeneities, *i.e.* porous and dislocations, as described by a set of order parameters, similarly to phase field theories, was proposed. Moreover, it is assumed that this quantity dynamically evolves only if a local state of tension exists as motivated by the discussion on Gao's work proposed in Section 2.3. It is thought that under dominant deviatoric deformation conditions the dependence on the rate might be accompanied by other competitive local state quantities such as accumulated strain and temperature. This newly-introduced length scale might be then associated with the formation of a zone of shear banding driven by temperature-dependent dislocation motion. This requirement can be then summarized in the following formalism:

$$l = \begin{cases} l_\phi^0, & \chi \geq 0 \\ \tilde{l}(\dot{F}), & \chi < 0 \end{cases}$$

The parameter l_ϕ^0 is a constant which will be defined in the next section and depends on the material properties and problem discretization. In the following, the first law of thermodynamics is stated for a solid in the reference configuration, Ω_0, and internal energy per unit volume e_0. A micro-traction term, λ, is defined as equivalent to the micro-stress projection along the normal to the boundary surface:

$$\lambda = \xi_i N_i \tag{4.9}$$

The work conjugate quantity to the micro-force terms is assumed to be $\dot{\phi}$; therefore, the energy balance reads as it follows:

$$\begin{aligned} \frac{D}{Dt}\int_{\Omega_0}\left(\frac{1}{2}\rho\dot{U}_i\dot{U}_i+\frac{1}{2}\rho l^2\dot{\phi}\dot{\phi}+e_0\right)d\Omega_0 = \\ \int_{\partial\Omega_0}P_{ij}N_j\dot{U}_i d\partial\Omega_0+\int_{\Omega_0}B_i\dot{U}_i d\Omega_0+\int_{\partial\Omega_0}\lambda\dot{\phi}d\partial\Omega_0+\int_{\Omega_0}\gamma\dot{\phi}d\Omega_0 \end{aligned} \tag{4.10}$$

For the case of isothermal and adiabatic processes, as considered in this work, the second law of thermodynamics can be reduced to that which neglects heat exchange and temperature variation within the control volume

$$\frac{D}{Dt}\int_{\Omega_0}\theta\dot{s}_0 d\Omega_0 \geq 0 \tag{4.11}$$

Assuming a Legrende transformation between the Helmholtz strain energy, ψ, and the referential internal energy e_0

$$e_0=\psi+\theta s_0 \tag{4.12}$$

the second law reduces to the following dissipation inequality:

$$\Rightarrow \dot{\psi}\leq\dot{e}_0 \tag{4.13}$$

By employing the Gauss theorem on the boundary quantities in 4.10 along with the local form for the balance laws in equation 4.7 the explicit form for the dissipation can be obtained:

$$\int_{\Omega_0}\dot{\psi}d\Omega_0\leq\int_{\Omega_0}(P_{ij}\dot{F}_{ij}+\xi_i\dot{\phi}_{,i}-\pi\dot{\phi}-\rho l l'\dot{\phi}\dot{\phi})d\Omega_0 \tag{4.14}$$

The energy functional in equation 4.1 is assumed to have dependency on F, ϕ, ϕ_j and $\dot{\phi}$, therefore by subsequently applying the chain rule the dissipation inequality can be further decomposed:

$$\int_{\Omega_0}\Big(\frac{\partial\psi}{\partial F_{ij}}\dot{F}_{ij}+\frac{\partial\psi}{\partial\phi}\dot{\phi}+\frac{\partial\psi}{\partial\phi_{,i}}\dot{\phi}_{,i}+\frac{\partial\psi}{\partial\dot{\phi}}\ddot{\phi}\Big)d\Omega_0\leq \int_{\Omega_0}(P_{ij}\dot{F}_{ij}+\xi_i\dot{\phi}_{,i}-\pi\dot{\phi}-\rho ll'\dot{\phi}\dot{\phi})d\Omega_0 \tag{4.15}$$

Application of the Coleman-Noll procedure [204] leads to the following constitutive relations:

$$\frac{\partial\psi}{\partial F_{ij}}=P_{ij} \tag{4.16a}$$

$$\frac{\partial\psi}{\partial\dot{\phi}}=0 \tag{4.16b}$$

$$\frac{\partial\psi}{\partial\phi_{,i}}=\xi_i \tag{4.16c}$$

$$\frac{\partial\psi}{\partial\phi}+\pi\leq 0\rightarrow\frac{\partial\psi}{\partial\phi}=-\pi-\eta\dot{\phi} \tag{4.16d}$$

where η collects the remaining terms acting on the rate of growth of the phase field parameter and can be assumed to be a function of the rate of deformation as well as its acceleration:

$$\eta=\rho ll'\Rightarrow\eta=\tilde{\eta}(\dot{F}_{ij},\ddot{F}_{ij}) \tag{4.17}$$

Having postulated these constitutive relations implies that the source of dissipation reduces to η which therefore has to assume positive values in order to satisfy inequality 4.15. This further implies that $l'\geq 0$ has to be enforced. Substituting the constitutive relations into the balance laws leads to the following governing equations:

$$P_{ij,j}+B_i=\rho\ddot{U}_i \tag{4.18a}$$

$$g'\psi^0_{F,a}-\frac{\tilde{G}_c}{l_0}\phi-\tilde{G}_c l_0\Delta\phi-\eta\dot{\phi}=\rho l^2\ddot{\phi} \tag{4.18b}$$

The boundary value problem is governed by two hyperbolic equations, in which equation 4.18b is treated as one having low stiffness, *i.e* the contribution of the Laplacian operator scaled by the factor $\tilde{G}_c l_0$ is small compared to the other terms. Given these conditions, an updated-Lagrangian framework with classical Galerkin-type of spacial discretization and explicit time integration, based on an energy-conserving leap-frog algorithm, has been implemented within the in-house code DEST. It has to be pointed out that previous contributions had to rely on the use of implicit solvers to solve the coupled system in view of the linear momentum and the phase field equations presenting a hyperbolic (elliptic for the quasi-static case) and elliptic form, respectively. Numerical implementation strategies based upon the use of an operator split with strain energy history functional have allowed to decouple the equations and reduce the numerical complexity. However, the thermodynamic consistency of this methodology has not been proven yet. Therefore, stress and deformation measures are redefined in terms of their respective equivalent in the current configuration. The first Piola-Kirchhoff stress is transformed into the true-Cauchy counterpart using the classical relation:

$$\sigma_{ij} = J^{-1} F_{ik} P_{kj} \tag{4.19}$$

where J^{-1} is the Jacobian determinant which allows to transform between the two configurations. Moreover, it can be pointed out that the constitutive equation for the stress obtained from the employment of the functional in equation 4.1 are of grade zero. This implies that the stress can be computed from the state of deformation without having to further consider any dependency on its own history. This allows to employ a hypoelastic-incremental law to integrate the stress given that the solution is computed for small increments in the deformation [205]. The kinematics can be interpreted in terms of the velocity gradient, L_{ij}, with its symmetric and antisymmetric counterparts defined as the rate of deformation, D_{ij}, and spin tensor, W_{ij}, respectively. Their definitions are reported below:

$$L_{ij} = \dot{F}_{ik} F^{-1}_{kj} \tag{4.20a}$$

$$D_{ij} = \frac{1}{2}\Big(L_{ij} + L_{ji}\Big) \tag{4.20b}$$

$$W_{ij} = \frac{1}{2}\Big(L_{ij} - L_{ji}\Big) \tag{4.20c}$$

A hypoelastic constitutive law, with incremental objective stress update, can be generally expressed in terms of rate of deformation and stress at the previous increment:

$$\overset{\triangledown}{\sigma}_{ij} = f(\sigma_{ij}, D_{ij}) \tag{4.21}$$

where $\overset{\triangledown}{\sigma}_{ij}$ is the objective Jaumann rate of the Cauchy stress computed as:

$$\overset{\triangledown}{\sigma}_{ij} = \frac{D\sigma_{ij}}{Dt} - W_{ik}\sigma_{kj} - \sigma_{ik}W^{T}_{kj} \tag{4.22}$$

The objective rate of the rate of deformation tensor is calculated according to the Jaumann analogue as defined in the work of Stolarski and Belytschko [206] which is valid for any arbitrary strain formulation:

$$\ddot{F}_{ij} = D^{0}_{ij} = sym(\nabla a_{ij}) - L_{ik}D_{kj} + L^{T}_{ik}W_{kj} \tag{4.23}$$

4.5 Numerical Implementation

In this section derivations of the discretized equations are presented in the spirit of standard arguments of the Galerkin method. Later, the time integration scheme will be discussed. The two governing equations 4.18 are integrated within the domain and pre-multiplied by generic test functions, δw_j and δq for the momentum and phase field equations respectively, as below:

$$\int_{\Omega} \delta w_i(\sigma_{ij,j} + B_i - \rho \ddot{U}_i) d\Omega = 0; \tag{4.24a}$$

$$\int_{\Omega} \delta q(g' \psi^0_{F,a} - \frac{\tilde{G}_c}{l_0}\phi - \tilde{G}_c l_0 \Delta\phi - \eta\dot{\phi} - \rho l^2 \ddot{\phi}) d\Omega = 0 \tag{4.24b}$$

After carrying out the integration by parts where necessary, the following weak form of the coupled system of equations can be obtained:

$$\int_{\Omega} (\frac{\partial(\delta w_i)}{\partial x_j}\sigma_{ij} + \delta w_i B_i + \delta w_i \rho \ddot{U}_i) d\Omega - \int_{\partial\Omega_{t_i}} \delta w_i \bar{t} d\partial\Omega = 0 \tag{4.25a}$$

$$\int_{\Omega} (\delta q(g' \psi^0_{F,a} - \frac{\tilde{G}_c}{l_0}\phi - \eta\dot{\phi} - \rho l^2 \ddot{\phi}) - \tilde{G}_c l_0 \frac{\partial \delta q}{\partial x_i}\frac{\partial \phi}{\partial x_i}) d\Omega + \int_{\partial\Omega} \delta q \frac{\partial \phi}{\partial x_i} n_i d\partial\Omega = 0 \tag{4.25b}$$

It has to be noted that the boundary integral in Equation 4.25a is interpreted as contributing to the set of external forces in the spirit of classical nonlinear finite element and will be employed to construct the solver. The boundary term in Equation 4.25b refers to condition on the flux of the phase field parameter and will be assumed equal to zero as treated by Borden et. al. [164]. The unknowns, U_i and ϕ as well as the weight functions δw_i and δq_i can be expressed in their explicit form in terms of basis functions, shape functions $N_i(x_i)$ and control variables u_I, ϕ_I, δw_i, δq_i respectively and as concisely expressed below:

$$\delta w_i = \sum_I^{n_D} N_I(x_i)\delta w_{iI} \quad (4.26a) \qquad \delta q = \sum_I^{n_D} N_I(x_i)\delta q_I \quad (4.26b)$$

$$u_i = \sum_I^{n_D} N_I(x_i) u_{iI} \quad (4.27a) \qquad \phi = \sum_I^{n_D} N_I(x_i)\phi_I \quad (4.27b)$$

where n_D is the number of nodes in the spatial discretization. Substitution of these relations into Equations 4.25 and by assuming that equilibrium is satisfied for any arbitrary choice of δw and δq, the following set of discrete terms can be defined:

$$f_{iI}^{int,U} = \int_{\Omega_\xi} \frac{\partial N_I}{\partial x_j} \sigma_{ij} J_\xi d\Omega_\xi \tag{4.28a}$$

$$f_I^{int,\phi} = \int_{\Omega_\xi} \frac{1}{l^2} \Big(N_I \Big(g' \psi_{F,a}^0 - \frac{\tilde{G}_c}{l_0} \phi - \eta \dot{\phi} - \rho l^2 \ddot{\phi} \Big) - \tilde{G}_c l_0 \frac{\partial N_I}{\partial x_i} \frac{\partial N_I}{\partial x_i} \phi \Big) J_\xi d\Omega_\xi \tag{4.28b}$$

$$f_{iI}^{ext,U} = \int_{\Omega_\xi} N_I \rho b_i J_\xi d\Omega_\xi + \int_{\partial\Omega_\xi} N_I \bar{t}(x_{i,\xi} \times x_{j,\eta}) d\xi d\zeta \tag{4.28c}$$

$$M_{ijIJ}^U = \delta_{ij} \int_{\Omega_\xi} \rho N_I N_J J_\xi^0 d\Omega_\xi \tag{4.28d}$$

$$M_{IJ}^\phi = \delta_{IJ} \int_{\Omega_\xi} \rho N_I N_J J_\xi^0 d\Omega_\xi \tag{4.28e}$$

In the above, as it will be in the following, the superscripts U and ϕ refer to quantities associated with the displacement and phase field parameter respectively. Therefore, $f_{iI}^{int,U}$ and $f_{iI}^{int,\phi}$ are the internal forces. The external force $f_{iI}^{ext,U}$ comprises any boundary traction, $\bar{t}$, and body force b_i which will be assumed absent, *i.e.* $b_i = 0$. The mass matrix M_{ijIJ}^U and M_{IJ}^ϕ are diagonal. The integration is carried out over the parent element domain Ω_ξ with mapping to the current configuration described by the determinant of the Jacobian, J_ξ. As in most of the standard nonlinear finite element procedure, integration of the mass-related quantities is carried out over the initial configuration. Having defined these quantities allows to reduce the governing equation to the following set of discrete equations:

$$f_{iI}^{int,U} + M_{ijIJ}^U \ddot{u}_{iI} = f_{iI}^{ext,U} \tag{4.29a}$$

$$f_I^{int,\phi} - M_{IJ}^\phi \ddot{\phi}_I = 0 \tag{4.29b}$$

the solution will be computed incrementally by means of a leap-frog algorithm with time step dictated by the Courant condition, *i.e.* $\Delta t \leq h^*/c$, where h^* is the current characteristic element length. This condition on predominant time step as dictated by the linear momentum equation has been assumed on the basis that both the driving force and l are calculated as a result of quantities associated with the mechanical solution.

4.5.1 Implementation within in-house code

In the following, the numerical implementation within the finite element code DEST, developed within the impact engineering laboratory, is presented. The code is written in C and currently based on a single processor solver. The geometry and the mesh for all the benchmarks which will follow have been created in Abaqus, whilst postprocessing of the results has been carried out in Paraview. The time step is indicated with the superscript n which refers to the current iteration, whilst the first iteration in the analysis is indicated with n_0. The process flow consists of the main steps reported below, which are listed according to the routine (*e.g name*.c) or function (*e.g* F_*name*) which they refer to.

1. dbase.c: allocation of space for database structure;
   1.1. F_dbase_init(db): initialization of variables: geometry, forces, initial conditions and prescribed conditions;
2. analyser.c: allocate memory for solution data structure
   2.1. F_start_data_read(db): read input file
   2.2. F_analyse: set steps for solution and invoke function *F_solve*
3. solve.c: execution of phase loop and initialization of paraview and history output files.

3.1. F_solve_increments: solution management articulated in the following functions for discrete equations assembling and integration.

4. F_assinit: imposition of initial conditions ($n = n_0$) on $\dot{u}_i^{n_0}$, $u_i^{n_0}$, $\dot{\phi}^{n_0}$, ϕ^{n_0}, $\sigma_{ij}^{n_0}$

5. F_assrld (in assrld.c): assembly of internal forces $f_{iI}^{int,U}$ and $f_{iI}^{int,\phi}$.

6. F_elstatupd (in el_s3831pf): evaluation of internal forces for the specific element formulation. In this work, three-dimensional linear (8 nodes), reduced integration (single Gauss-point) hexahedronal elements are employed. The total amount of elements in the mesh are grouped in clusters of 32 elements per subgroup. This is operation is required as part of the 32-bit architecture of the code and aimed at improving the memory allocation management. The operations listed below are performed for each element in the subgroup.

   6.1. extract current nodal coordinates and nodal velocities at time step *n-1/2*.

   6.2. F_geom: compute shape functions. This function includes the calculation of the Jacobian of each element and characteristic length of the element for time-step update.

   6.3. F_rate: calculate L_{ij}^n, D_{ij}^n, W_{ij}^n, $\dot{F}^n$, ϕ^n and $g(\phi)^n$.

   - The value of the phase field parameter, ϕ is calculated at the Gauss-point by interpolating its nodal values, *i.e.* $\phi^n = \sum_{I=1}^{8} N_I \phi_I^n$
   - The degradation function is calculated at the Gauss-point from the phase field parameter. Different forms for $g(\phi)$ will be discussed in the following section.

7. F_matstaupd: calculate deformation-related quantities such as stress and reference strain energy functional.

   7.1. rotate undamaged stress: $\overset{\triangledown}{\sigma}{}_{ij}^{0,n-1} = \sigma_{ij}^{0,n-1} + \sigma_{ik}^{0,n-1} W_{jk}^n - W_{ik}^n \sigma_{kj}^{0,n-1}$. For the sake of simplicity the symbol $\triangledown$ is dropped and the stress, already rotated, will be indicated in standard notation as $\sigma_{ij}^{0,n-1}$.

   7.2. calculate hydrostatic, p, and deviatoric, σ'_{ij} counterparts of the undamaged stress respectively obtained as: $p^{0,n-1} = \frac{1}{3}\sigma_{kk}^{0,n-1}$ and $\sigma'_{ij} = \sigma_{ij} - \frac{1}{3}\delta_{ij}\sigma_{kk}\sigma_{ij}^{0,n}$.

   7.3. split of hydrostatic pressure to calculate active and passive contribution to crack driving force.

   $$\begin{cases} p^{0,n-1,h+} = p^{0,n-1}, & p^{0,n-1,h-} = 0; \qquad if \quad p^{0,n-1} > 0 \\ p^{0,n-1,h+} = 0, & p^{0,n-1,h-} = p^{0,n-1}; \qquad if \quad p^{0,n-1} \leq 0 \end{cases}$$

   7.4. incremental update of stress components: $\sigma_{ij}^{0,n} = \sigma_{ij}^{0,n-1} + \Delta(2\mu D_{ij}^n + \delta_{ij}\lambda D_{kk}^n)$

   7.5. calculate hydrostatic and deviatoric counterparts of the stress tensor as in 7.2. for the updated stress at step n and active/passive components as in 7.3..

   7.6. calculate damaged stress components: $\sigma_{ij}^n = p^{0,n,h^-} + g(\phi)^n \left(p^{0,n,h^+} + \sigma_{ij}^{\prime,0,n}\right)$

   7.7. calculate stress invariants: $I_1^n = \sigma_{kk}^n$, $I_2^n = \frac{1}{2}\left((\sigma_{kk}^n)^2 - \sigma_{ij}^n\sigma_{ij}^n\right)$ and $I_3^n = \epsilon_{ijm}\sigma_{i1}^n\sigma_{j2}^n\sigma_{m3}^n$

   7.8. calculate principal stresses:

$$\sigma_1^n = \frac{I_1^n}{3} + \frac{2}{3}\left(\sqrt{(I_1^n)^2 - 3I_2^n}\right) cos\theta \tag{4.30a}$$

$$\sigma_2^n = \frac{I_1^n}{3} + \frac{2}{3}\left(\sqrt{(I_1^n)^2 - 3I_2^n}\right) cos\left(\theta - \frac{2\pi}{3}\right) \tag{4.30b}$$

$$\sigma_3^n = \frac{I_1^n}{3} + \frac{2}{3}\Big(\sqrt{(I_1^n)^2 - 3I_2^n}\Big)cos\Big(\theta - \frac{4\pi}{3}\Big) \tag{4.30c}$$

where

$$\theta = \frac{1}{3}cos^{-1}\left(\frac{2(I_1^n)^3 - 9I_1^n I_2^n + 27I_3^n}{2\Big((I_2^n)^2 - 3I_2^n\Big)^{3/2}}\right) \tag{4.31}$$

7.9. calculate current triaxiality (equation 4.4:

$$\chi^n = -\frac{\sigma_1^n + \sigma_2^n + \sigma_3^n}{3\sqrt{1/2\Big((\sigma_1^n - \sigma_2^n)^2 + (\sigma_2^n - \sigma_3)^2 + (\sigma_3^n - \sigma_1^n)^2\Big)}} \tag{4.32}$$

7.10. calculate active reference strain energy associated with crack driving force:

$$\psi_a^{0,n} = \psi_a^{0,n-1} + \tfrac{1}{2}\Big(\Big(p^{0,n-1,h^+} + p^{0,n,h^+}\Big)D_{kk}^n \Delta t + \Big(\sigma_{ij}^{\prime,0,n-1} + \sigma_{ij}^{\prime,0,n}\Big)D_{ij}^{\prime,n}\Delta t\Big)$$

8. F_mass (in el _s3831pf): calculate mass in equations 4.28d and 4.28e. This operation is performed only at $n = n_0$ as the mass it is assumed to be constant. The mass matrix is diagonal, therefore allowing for direct inversion in the explicit time integration;

9. F_asseld (in asseld.c): calculate external forces in equation 4.28c;

10. F_asspld (in asspld.c): assign prescribed kinematic (*i.e* displacement and velocity) and phase field nodal values;

11. F_frc (in el _s3831pf): calculate internal forces. In this routine a series of operations are performed in order to compute all the terms in equations 4.28b.

    11.1. calculate effective critical energy release rate, $\tilde{G}_c^n$, based on current triaxiality, χ^n as postulated in equation 4.6;

    11.2. calculate gradient and laplacian contribution of the phase field parameter.

11.3. calculate components of rate of rate of deformation, $\dot{D}^n_{ij}$ and effective con-tribution $\sqrt{2/3\dot{D}^n_{ij}\dot{D}^n_{ij}}$

11.4. calculate rate-dependent micro-inertia length scale, l, and adaptive viscos-ity, η. Explicit forms for these quantities will be reported in equations 4.46 and 4.48 along with a detailed explanation on their derivation and associated calibration therein;

11.5. calculate internal forces according to equations 4.28a and 4.28b;

12. F_solve (in solve.c): explicit-time integration of the governing equations based on leap-frog algorithm. In the following description, displacement and phase field parameter are indicated as a generic variable, d_k, with velocity and ac-celeration v_k and a_k respectively. The internal forces, external forces, traction and mass are uniquely indicated with f^{int}_{kI}, f^{ext}_{kI}, $\bar{t}_{kI}$ and M_{klIJ}. The indexes k and l go from 1 to 4 which is the total number of degrees of freedom per node (*i.e.* first 3 associated with the displacement and the remaining with the phase field parameter). It has to be noted that $\bar{t}$ relates to the surface traction whilst there is no comparable quantity in the phase field. Moreover, it was required to introduce a coefficient α_1 to ensure that ϕ remains positive during the ana-lysis, *i.e.* $\phi \geq 0$ for any $n \geq n_0$, given that any contribution to external forces associated with the phase field has been assumed to be zero, as discussed in the previous section. This formalism can be expressed in a compact form as below:

$$\begin{cases} k = 1,2,3 \;\; a^n_k = \ddot{u}^n_i, \;\; v^n_k = \dot{u}^n_i \;\; a^n_k = u^n_i \\ \\ k = 4 \qquad a^n_k = \ddot{\phi}^n_i, \;\; v^n_k = \dot{\phi}^n_i \;\; a^n_k = \phi^n_i \end{cases}$$

$$\begin{cases} k,l=1,2,3 \;\; \alpha_1 = 1, \;\; f_{kI}^{int,n} = f_{iI}^{int,U,n} \;\; f_{kI}^{ext,n} = f_{iI}^{ext,U,n}, \;\; \bar{t}_{iI} \neq 0, \;\; M_{klIJ}^{n} = M_{klIJ}^{U,n} \\ k,l=4 \qquad \alpha_1 = -1, \;\; f_{kI}^{int,n} = f_{I}^{int,\phi,n} \;\; f_{kI}^{ext,n} = f_{I}^{ext,\phi,n}, \;\; \bar{t}_{iI} = 0, \;\; M_{klIJ}^{n} = M_{IJ}^{\phi,n} \end{cases}$$

The numerical integration steps differ depending on the type of kinematic support assigned to the node at which the equations are being solved. The different cases are reported below and represent the core architecture of the solver in DEST. The relations listed for each case are computed as in the sequence here reported.

- Free node (no support condition assigned):

$$a_{kI}^{n} = \frac{(f_{kI}^{ext,n} - \alpha_1 f_{kI}^{int,n})}{M_{klIJ}^{n_0}} \tag{4.33a}$$

$$v_{kI}^{n} = v_{k}^{n-1} + a_{k}^{n}\left(\frac{\Delta t^{n} + \Delta t^{n-1}}{2}\right) \tag{4.33b}$$

$$d_{kI}^{n} = d_{kI}^{n-1} + v_{kI}^{n}\Delta t^{n} \tag{4.33c}$$

- Prescribed d_{kI}:

$$\Delta d_{kI}^{n} = d_{kI}^{n} - d_{kI}^{n-1} \tag{4.34a}$$

$$v_{kI}^{n} = \frac{\Delta d_{kI}^{n}}{\Delta t^{n}} \tag{4.34b}$$

$$a_{kI}^{n} = \frac{2(v_{kI}^{n} - v_{kI}^{n-1})}{\left(\Delta t^{n} + \Delta t^{n-1}\right)} \tag{4.34c}$$

$$v_{kI}^{n-1} = v_{kI}^{n} - a_{kI}^{n}\Delta t^{n} \tag{4.34d}$$

$$\bar{t}_{kI}^{n} = M_{klIJ}^{n} a_{kI}^{n} + f_{kI}^{int,n} - f_{kl}^{ext,n} \tag{4.34e}$$

$$f_{kl}^{ext,n} = \sum_{n} \bar{t}_{kI}^{n} \tag{4.34f}$$

- prescribed v_{kI}^n:

$$a_{kI}^n = \frac{2(v_{kI}^n - v_{kI}^{n-1})}{\left(\Delta t^n + \Delta t^{n-1}\right)} \tag{4.35a}$$

$$v_{kI}^{n-1} = v_{kI}^n - a_{kI}^n \Delta t^n \tag{4.35b}$$

$$d_{kI}^n = d_{kI}^{n-1} + v_{kI}^n \Delta t^n \tag{4.35c}$$

$$\bar{t}_{kI}^n = M_{klIJ}^n a_{kI}^n + f_{kI}^{int,n} - f_{kl}^{ext,n} \tag{4.35d}$$

$$f_{kl}^{ext,n} = \sum_n \bar{t}_{kI}^n \tag{4.35e}$$

- prescribed a_{kI}^n

$$v_{kI}^n = v_k^{n-1} + a_k^n \left(\frac{\Delta t^n + \Delta t^{n-1}}{2}\right) \tag{4.36a}$$

$$d_{kI}^n = d_{kI}^{n-1} + v_{kI}^n \Delta t^n \tag{4.36b}$$

$$\bar{t}_{kI}^n = M_{klIJ}^n a_{kI}^n + f_{kI}^{int,n} - f_{kl}^{ext,n} \tag{4.36c}$$

$$f_{kl}^{ext,n} = \sum_n \bar{t}_{kI}^n \tag{4.36d}$$

4.6 Uniaxial response

In this section, the model response, for the case of uniaxial dynamic tensile loading conditions, is examined. The problem is reduced to a single element calculation with one Gaussian point and zero Poisson ratio. All material properties are assigned unitary values. The model parameters required to define the mode of failure transition law do not play any role under these conditions and their effects will be examined in the following chapters. A small value for the viscosity, $\eta = 1^{-10}$ [Kg s^{-1}m^{-1}] , is chosen to maintain the rate-dependent nature of the model. Strain rate and total strain measures are computed as:

$$\dot{\varepsilon} = \sqrt{\frac{2}{3} D_{ij} D_{ij}} \qquad (4.37a) \qquad\qquad \varepsilon = \int_0^t \dot{\varepsilon} dt \qquad (4.37b)$$

It has to be noted that the strain is not involved anywhere in the formulation and subsequent implementation. The above quantity only indicates the accumulated, total strain, which preserves its accuracy for small increments in the deformation. In the first instance, the micro-inertia length scale is considered to be a constant. Assuming that in the limit of ϕ reaching unity within a time step, dimensional analysis considerations on equation 4.24b suggest a limiting lower bound, l_{ϕ}^{0}, below which the simulations become unstable:

$$l_{\phi}^{0} = \sqrt{\frac{G_c}{l_0 \rho}} \Delta t \tag{4.38}$$

A value of $l_{\phi}^{0}/l_0 = 10^{-7}$, controlled by the time-step, has been used in the one-dimensional simulations which follow, unless stated otherwise. Firstly, results pertaining the use of different forms for the degradation function, $g(\phi)$, are compared. The choice of the degradation function, usually of a polynomial type, is crucial for properly coupling the evolution of phase field parameter and the mechanical response of the material. It is required that at fracture, *i.e* $\phi = 1$, the material has reached the limit for load-carrying capacity; on the contrary for $\phi = 0$ the mechanical response should not be affected. The phase field parameter used to compute $g(\phi)$ is the maximum attained at that time in the simulation and indicated with ϕ^*; this strategy allows to avoid unphysical recovery of material stiffness in case of post-peak unloading. Moreover, its derivative should be a monotonic decreasing function for increasing

ϕ [173]. These requirements can be summarized as below:

$$\begin{cases} g(\phi^*) : [0,1], & \phi^* : [0,1] \\ g(0) = 1, & g(1) = 0 \\ g'(\phi^*) < 0 \\ g'(1) = 0 \end{cases} \tag{4.39}$$

In the literature, functions with a quadratic dependence on the phase field parameter have been often employed and assume the following form:

$$g(\phi) = (1 - \phi^*)^2 \tag{4.40}$$

Substituting this function in equation 4.24b leads to two critical values for the uniaxial stress/strain at which softening should begin under quasi-static loading conditions [164]

$$\sigma_c^0 = \frac{9}{16}\sqrt{\frac{G_c E}{3l_0}} \tag{4.41a}$$

$$\varepsilon_c^0 = \sqrt{\frac{G_c}{3El_0}} \tag{4.41b}$$

The mechanical response resulting from employing this function is evaluated against the one which uses a cubic one [207] of the type reported below:

$$g(\phi) = s((1 - \phi^*)^3 - (1 - \phi^*)^2) + 3(1 - \phi^*)^2 - 2(1 - \phi^*)^3, \tag{4.42}$$

where s is a constant. It is aimed to model the material response as the one corresponding to a brittle material exhibiting post-peak strain softening - *i.e.* semi-brittle - associated with the progressive formation, growth and coalescence of microcracks upon reaching of the critical load bearing capacity. This behaviour has been observed in several materials which do not develop significant macroscopic plastic deformation therefore referred as brittle. Examples of the tensile response under quasi-static loading conditions are reported in Figure 4.3. Results in Figure 4.4 pertain to low rate

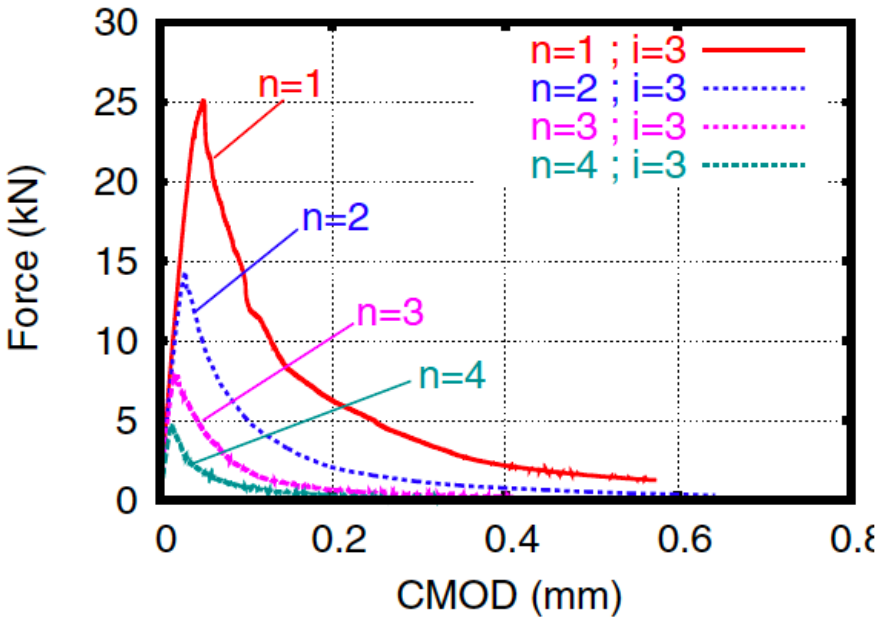

(a) Averaged load vs. CMOD response for unnotched concrete samples of different sizes n - reprinted from Gregoire et. al. [208]. The index i refers to the unnotched geometry as indicated in Figure 4 in Gregoire et. al. [208]

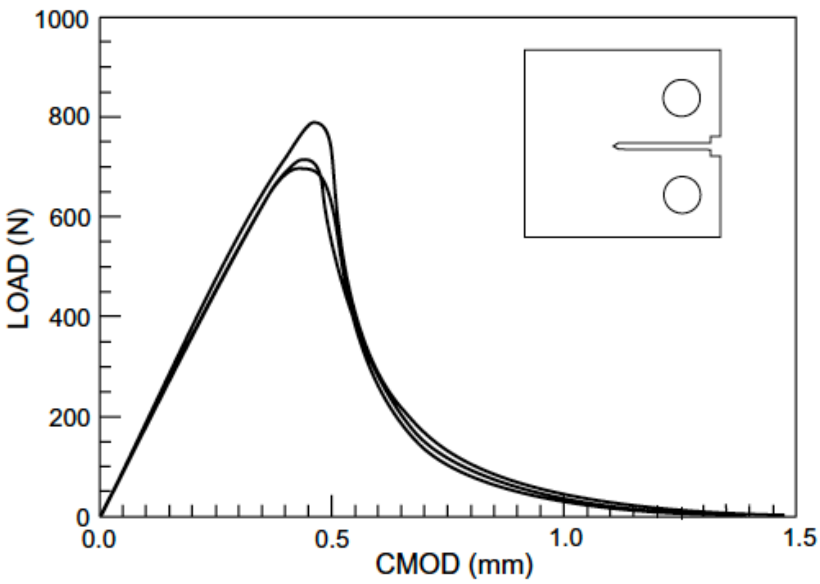

(b) Averaged load vs. CMOD response for notched PMMA CT samples repeated on samples with minor difference notch depth - reprinted from Gomez at. al [209]

Figure 4.3: Representative load-displacement response for typical semi-brittle materials under tension exhibiting post-peak strain softening. The displacement is indicated in terms of the crack mouth opening displacement (CMOD) while the load refers to the remote force applied to the sample.

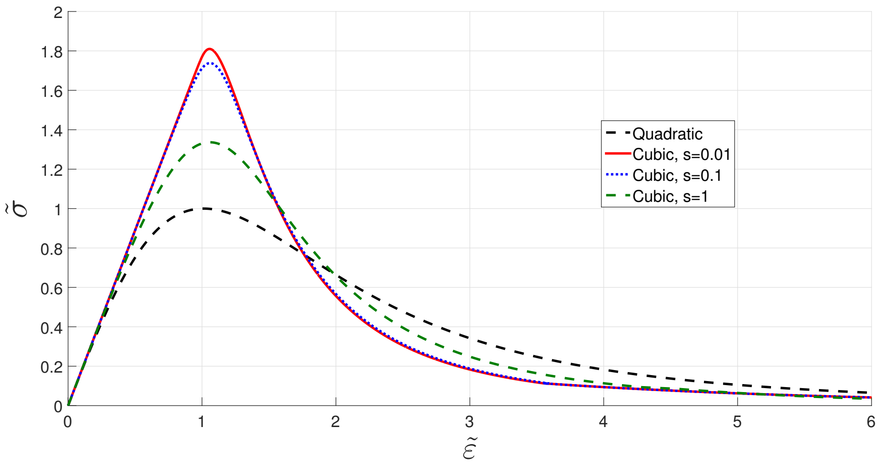

Figure 4.4: Comparison between the uniaxial response for the case of quadratic and cubic degradation function. Stress and strain are normalized by the theoretical scaling proposed in $\tilde{\sigma} = \sigma/\sigma_c^0$, $\tilde{\varepsilon} = \varepsilon/\varepsilon_c^0$

loading conditions, $\dot{\varepsilon} = 0.1$ $[ms^{-1}]$; therefore, macro-inertia effects on the mechanical response can be considered reasonably negligible or absent. It can be noticed that, for the case of quadratic degradation function, the model presents a softening response starting after the critical values in equation 4.41 have been attained. However, this choice leads to an undesired non-linear behaviour even in the elastic regime. Conversely, a cubic dependence on ϕ progressively overcomes this issue, as smaller values for s are assumed. Moreover, an increase in the peak stress is registered as it varies from the analytical estimates in equation 4.41a, along with a sharper softening decay. The reason for these differences can be explained by examining the correspondent evolution for ϕ presented in Figure 4.5. It is shown that for the case of quadratic degradation function, the phase field parameter grows even before the peak stress is reached at a correspondent value of $\phi \approx 0.25$ which is responsible for the change from the linear elastic behaviour. Instead, the cubic degradation function ensures little variation in ϕ prior to softening. Therefore, in the simulations carried out in this work a cubic degradation function formulation, with $s = 0.01$ will be employed. As far as the mechanical response under increasing loading rates is concerned, no changes have been observed for very small values of l as it has been initially chosen. However, for increasing value of l, implying that inertia effects in the evolution of the phase field parameter become more predominant, distinct variations are observed as reported in Figure 4.6. The chosen micro-inertia length scale corresponds to $l/l_0 = 10^{-3}$. It is observed that for increasing rates higher values for the peak stress are attained and a sharper softening decay is registered. Importantly, the softening plateau presents oscillations both in the stress and ϕ, as clearly noticeable in Figure 4.7. This behaviour implies the occurrence of cycling unloading/reloading due to the harmonic-oscillating nature of phase field equation. However, the degradation of the material stiffness is preserved as the slope of the reloading path in the stress-strain decreases at every oscillation. Moreover, as shown in Figure 4.8 the total rate of dissipation remains positive despite the oscillating behaviour, therefore ensuring that thermodynamical consistency is retained. Rate of dissipation and time have been normalized by two reference values defined as:

$$D_0 = \frac{G_c B L}{dt} \qquad (4.43a) \qquad\qquad T_0 = t_r + \sqrt{\frac{5\rho L^2}{2\mu}} \qquad (4.43b)$$

where B, L, μ are the thickness, characteristic size of the model and the shear modulus, respectively. The normalization accounts for any rise time, t_r that might have been used to ramp the applied load. It has to be pointed out that the amplitude of the oscillations also depend upon the value of l_ϕ^0 as it is calculated by means of relation 4.38. In particular, it can be observed that for $l_\phi^0 \to 0$ the loading rate required to

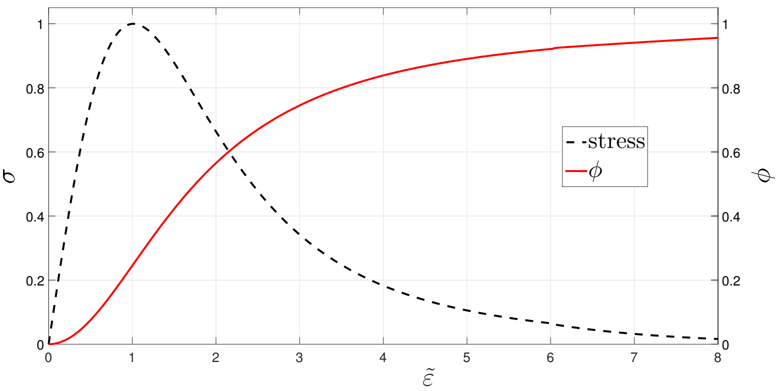

(a) Stress and phase field repose for the case of quadratic degradation function

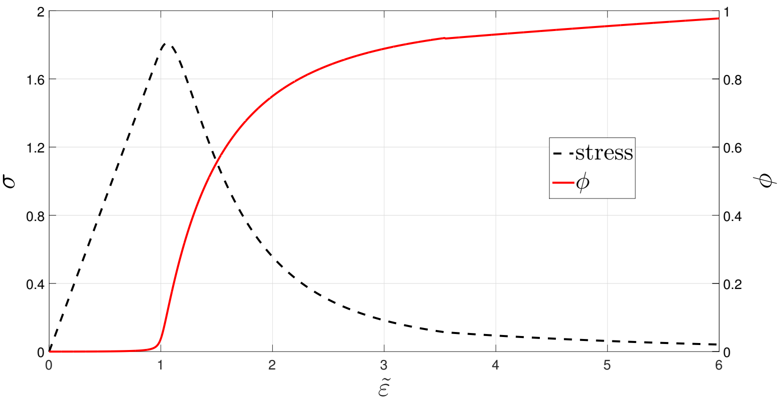

(b) Stress and phase field repose for the case of cubic degradation function

Figure 4.5: Comparison of phase field evolution over the uniaxial mechanical response. Stress and strain have been normalized by their respective values prior softening.

trigger oscillations increases. In turn, this implies that for $\Delta t \to 0$ oscillations would be theoretically of infinitesimal amplitude and possibly suppressed. Physically, this would mean that the discretization would have to be comparable to the atomic spacing which however would dictate the smallest length scale. Moreover, the oscillating behaviour is observed only in the softening plateau, *i.e.* associated with bond breakage, which suggests that it could be reduced by employing an adaptive time-stepping procedure. This issue will be addressed in future work along with methodologies to perform dynamic, adaptive re-meshing.

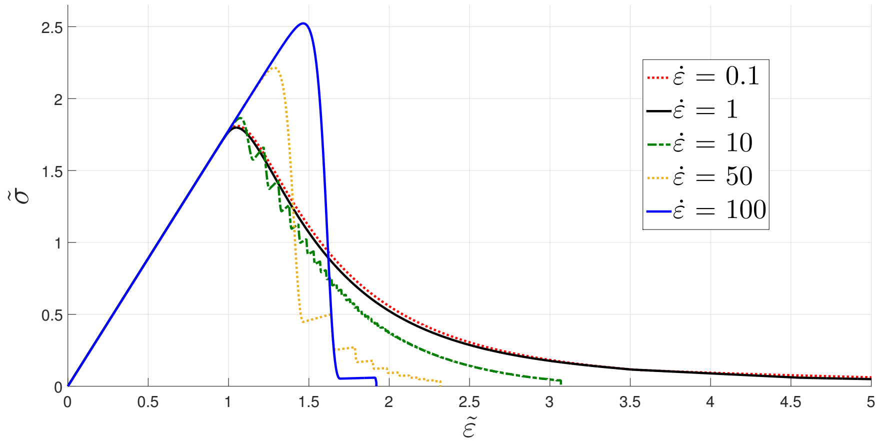

Figure 4.6: Uniaxial response for different loading rates

Next, the effect of the combined variation of the micro-inertia length scale and of the loading rate is analysed. Results are presented in terms of maximum peak stress attained for varying l as well as nominally imposed loading rate $\dot{\varepsilon}$ and reported in Figure 4.9. It is shown that for increasing rates, higher magnitudes for the peak stress are registered. Similarly, given a loading regime, an increase in l/l_0 results in higher thresholds for the start of softening. These results suggest that larger values of l are associated with an additional dissipative mechanism in which the *mass* of material confined with this zone, in the proximity of the crack-path, provide a toughening-like effect responsible for higher resistance to crack failure initiation. Therefore, it can be noticed that the model presents an inherent sensitivity with respect to the variation of these parameters which can be thought to obey the following law:

$$\frac{\sigma_c}{\sigma_c^0} = (\alpha \ln(\dot{\varepsilon}) + \gamma_2)\left(\frac{l}{l_0}\right)^{\gamma_1} \tag{4.44}$$

This law can be further manipulated in order to calibrate the response of the model such that the critical stress for softening corresponds to that obtained through experiments. As a first *phenomenological* approximation, this quantity can be conceived to

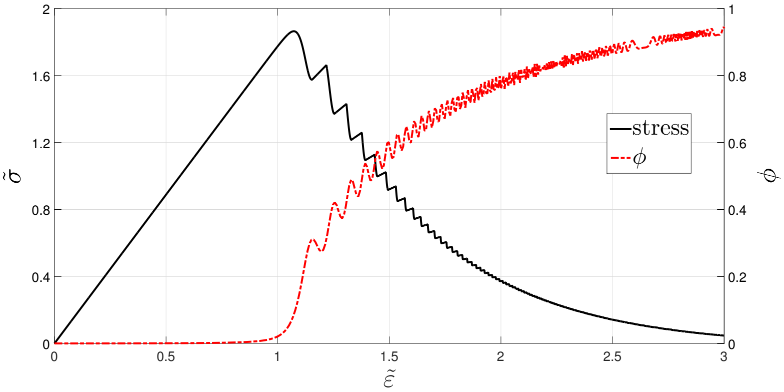

(a) Stress and phase field response for the case $\dot{\varepsilon} = 10\ ms^{-1}$

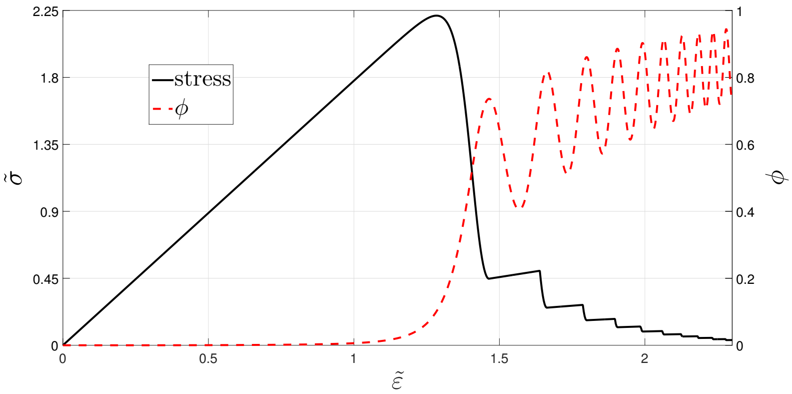

(b) Stress and phase field response for the case $\dot{\varepsilon} = 50\ ms^{-1}$

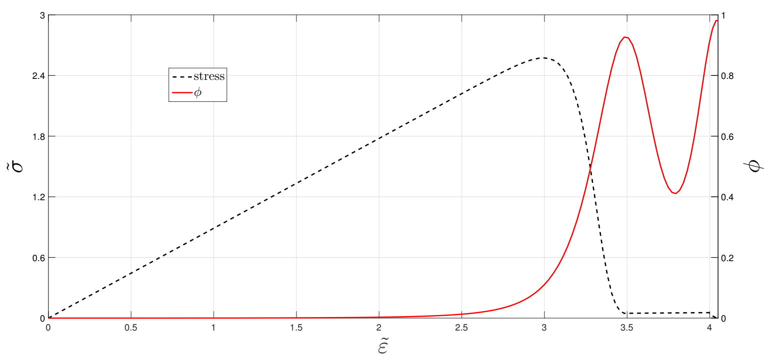

(c) Stress and phase field response for the case $\dot{\varepsilon} = 100\ ms^{-1}$

Figure 4.7: Comparison of phase field evolution over the uniaxial mechanical response. Stress and strain have been normalized by their respective values prior softening.

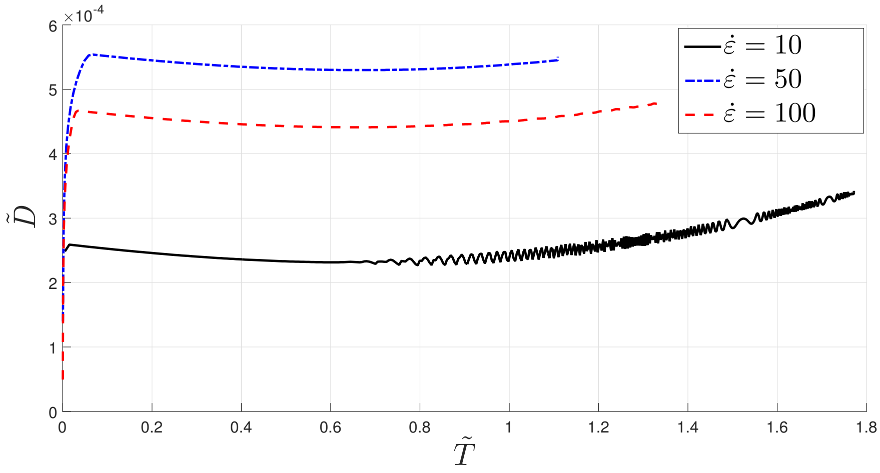

Figure 4.8: Total dissipation rate of dissipation normalized by $(GcBL)/dt$

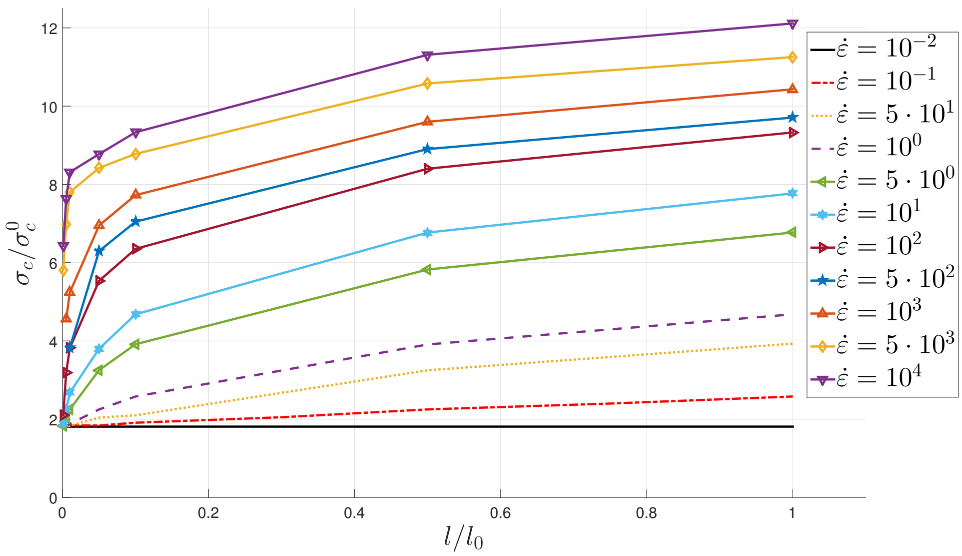

Figure 4.9: Peak stress attained at softening as a function of l for different rate of loading in $[ms^{-1}]$

be the macroscopic strength of the material. In this context, the strength is assumed to be the maximum load-carrying capacity which proceeds irreversible material degradation due to excessive micro-cracking. In this work, the scaling law proposed by Grady and Lipkin [112] for an isolated crack under remote tensile loading is employed:

$$\sigma_{c,e} = \sigma_{c,e}^{0}\left(1 + \left(\frac{\dot{\varepsilon}}{\dot{\varepsilon}_0}\right)^{n_2}\right) \tag{4.45}$$

where $\sigma_{c,e}$ and $\sigma_{c,e}^0$ are the experimentally measured strength values at dynamic and quasi-static loading conditions, respectively. The reference strain rate $\dot{\varepsilon}_0$ is associated with the threshold for the transition between the two loading regimes. Therefore, a comparative calibration between the model proposed in this work and the experimentally derived scaling law can be assumed such that $\sigma_{c,e} \approx \sigma_c$. By making use of this assumption, a dynamic scaling law for the micro-inertia length scale can be obtained:

$$l = l_0 \left(\frac{\sigma_{c,e}^0}{\alpha \sigma_c^0} \left(1 + \left(\frac{\dot{\varepsilon}}{\dot{\varepsilon}_0} \right)^{n_1} \right) \right)^{\frac{1}{\gamma_1}} \tag{4.46}$$

where the the function α is defined as:

$$\alpha = f(\dot{\varepsilon}) \ln(\dot{\varepsilon}) + \gamma_2 \tag{4.47a}$$

$$f = (\gamma_3 \dot{\varepsilon} + \gamma_4) \frac{\langle \dot{\varepsilon}_0 - \dot{\varepsilon} \rangle}{(\dot{\varepsilon}_0 - \dot{\varepsilon})} + (\gamma_5 \ln(\dot{\varepsilon}) + \gamma_6) \frac{\langle \dot{\varepsilon} - \dot{\varepsilon}_0 \rangle}{(\dot{\varepsilon} - \dot{\varepsilon}_0)} \tag{4.47b}$$

Given this non-trivial rate-dependent law, an equivalent for the dynamic viscosity in equation 4.17 can be obtained:

$$\eta = l_0 \sigma_{c,e}^0 \frac{((g_1 - g_2) g_3) g_4}{g_5} \tag{4.48}$$

with the explicit forms for the sub-functions g_i reported below:

$$g_1 = \frac{n_2 \ddot{\varepsilon} \frac{\dot{\varepsilon}}{\dot{\varepsilon}_0} (f \cdot \ln(\dot{\varepsilon}) + \gamma_2)}{\dot{\varepsilon}} \tag{4.49a}$$

$$g_2 = \left(\frac{\dot{\varepsilon}}{\dot{\varepsilon}_0} \right)_2^n + 1.0 \tag{4.49b}$$

$$g_3 = f' \ln(\dot{\varepsilon}) + \frac{f \ddot{\varepsilon}}{\dot{\varepsilon}} \tag{4.49c}$$

$$g_4 = \left(\frac{g_3 \sigma_{c,e}^0}{\alpha \sigma_c^0} \right)^{\frac{1}{\gamma_1} - 1} \tag{4.49d}$$

$$g_5 = \sigma_c^0 \gamma_1 \alpha^2 \tag{4.49e}$$

Material Parameter	Value
E	32 [GPa]
ν	0.2
ρ	$2.4 \cdot 10^{-6}$ [Kg $\cdot$ mm^{-3}]
G_c	$2 \cdot 10^{-6}$ [J $\cdot$ mm^{-2}]
l_0	$5 \cdot 10^{-3}$ [mm]
$\sigma^0_{c,e}$	$5 \cdot 10^{-2}$ [GPa]
n_2	0.33
$\dot{\varepsilon}_0$	1000 [s^{-1}]
β	9
χ_L	0.3
χ_U	0.6

Table 4.1: Material parameters used in the simulations

A calibration procedure for the full-defined set of parameters is now carried out on the basis of pseudo-realistic material properties representative of the mechanical behaviour of PMMA.

The regularization zone l_0 is here interpreted as an approximation of the macroscopic length scale at which irreversible damage due coalescence of micro-cracking occurs. In absence of direct measurements the scaling law proposed by Bazant [210] can be employed as a first order approximation:

$$l_0 \approx \frac{EG_c}{2(\sigma^0_{c,e})^2} \tag{4.50}$$

In particular the quantities strictly related to fracture are scaled such that the macroscopic damage regularization zone, l_0, is much smaller than any length scale governing the problem such as the characteristic length of the specimen, *e.g.* $L = 1mm$. In the following analysis, it is assumed that $l_0 \leq 0.01L$. In this study, the main fracture quantity which is considered dictated by experiments is the strength $\sigma^0_{c,e}$ with the Young's modulus, E and critical energy release rate, G_c, scaled such that the condition on l_0 is met. Therefore, the material properties used in the simulations are listed in table 4.1. It should pointed out that the assumed values closely follow those employed by Borden et. al. [164]. The value for β has been assumed on the basis of the results provided by Archer and Lesser [211] who pointed out that the ratio between the mode-II and mode-I fracture toughness in PMMA varies between $2.5 \leq K_{II_c}/K_{I_c} \leq 6$. The triaxiality bounds for the mode of failure transition have been extrapolated from the findings reported by Broberg [44].

Next, the sensitivity of the model on the variation of the parameters involved in the definition of the rate-dependent functions l and η is investigated. Simulations are carried out for different rates of loading and the strength compared, on a logarithmic scale, to the experimental baseline used for calibration.

Firstly, the effect of the parameters invariant with respect to the strain rate transition is discussed and results are presented in Figure 4.10. It is observed in Figure 4.10(a) that for decreasing values of γ_1 a lower value of the strength is obtained at loading rates above $\dot{\varepsilon}_0$ with a less step exponential increase. Conversely, a decrease in γ_2 does not alter significantly the exponential behaviour while shifts down the computed values for the strength by an almost constant quantity. The effect of the variation of the parameters which scale differently depending on the rate, used to calculate the function α, is now analysed and results reported in Figure 4.11. It can be seen that a decrease in the values of γ_3 and γ_5 results in higher strength values under high rates. Moreover, a decrease in γ_4 and γ_6 leads to lower strength, although a change in the exponential behaviour is also noticed.

This analysis will serve as a basis to set the model parameters used in the following chapters.

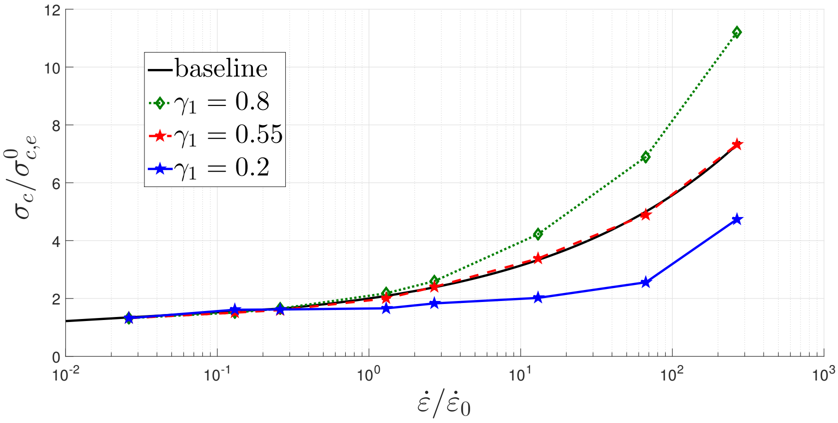

(a) Effect of variation of micro-inertia length scale exponent γ_1

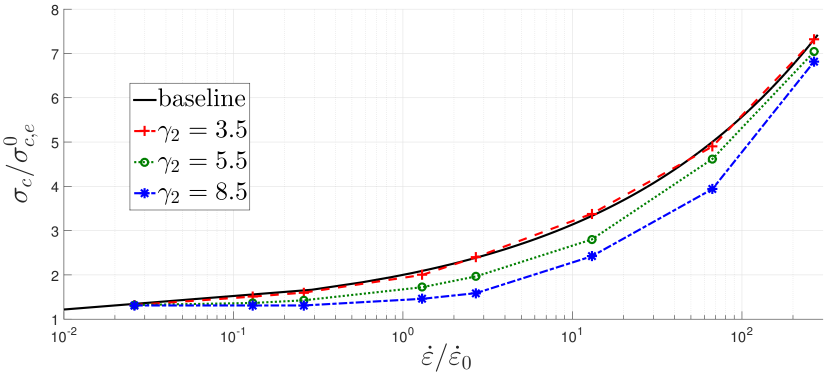

(b) Effect of variation of offset parameter γ_2

Figure 4.10: Rate-dependent behaviour of fracture normalized peak stress for parameters insensitive to rate-transition.

4.7 Model Calibration

In the following discussion, a procedure for the model calibration is provided. The aim of the proposed strategy is to guide the choice of the parameters needed to describe the pressure-rate-dependent response. The step-by-step data gathering can be summarized as follows:

1. Collection of elastic properties, *i.e.* Young's modulus E and Poisson's ratio ν

2. Collection of fracture properties:

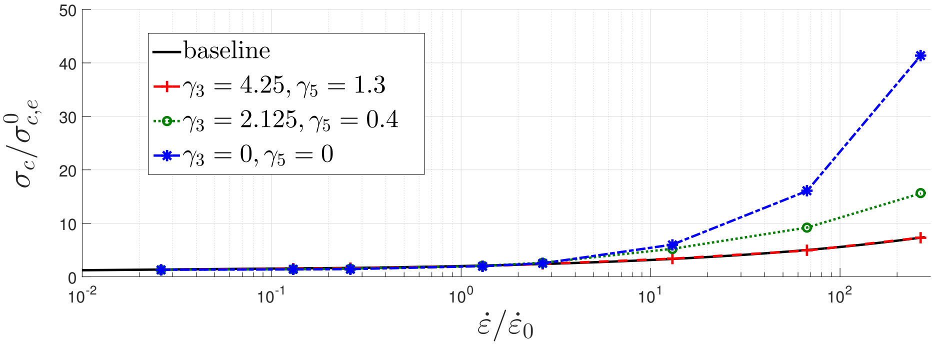

(a) Effect of variation of rate conjugate parameters of logarithm scaling function, γ_3, γ_5

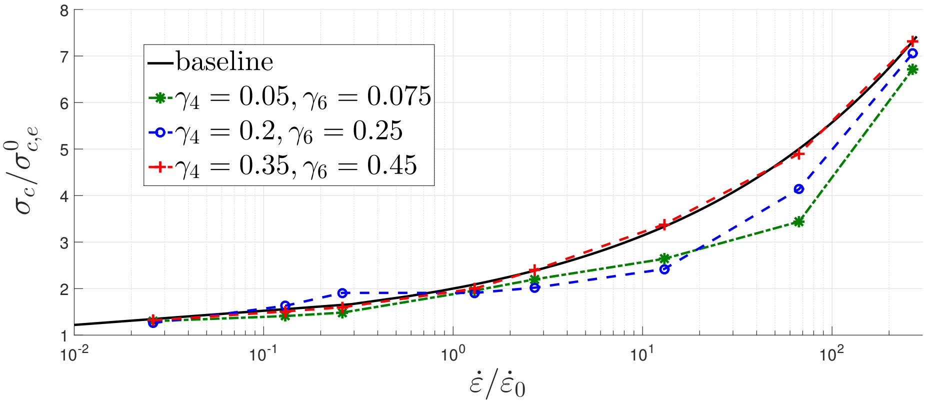

(b) Effect of variation of offset parameters on logarithm scaling function, γ_4, γ_6

Figure 4.11: Rate-dependent behaviour of fracture normalized peak stress for parameters scaled with rate.

- The mode-I critical energy release rate, G_c, associated with the energy required to create a new crack surface, can be estimated by performing fracture toughness tests on pre-cracked samples. These tests allow to obtain the corresponding mode-I critical stress intensity factor, $K_{I,C}$, which depends upon loading conditions and sample geometry. Under the assumption of small scale yielding conditions, *i.e.* plastic deformations are confined within a zone around the crack-tip which is significantly smaller than the initial crack, principles of LEFM can be employed. Therefore, the critical energy release rate can be calculated through:

$$G_c = \frac{K_{I,C}^2}{\tilde{E}} \tag{4.51}$$

where $\tilde{E} = E$ under plane stress or $\tilde{E} = E/(1-\nu^2)$ plain strain conditions.

- The quasi-static tensile strength, $\sigma_{c,e}^0$, can be obtained by measuring the stress-at-rupture in dogbone samples during uniaxial tests. Alternatively, the notch-scaled maximum load bearing capacity achieved prior softening in pre-cracked samples, such as compact tension specimens, subjected to remote tensile loading, can be measured (*e.g.* figures 4.3(a) and 4.3(b)).

3. Estimate of characteristic length scale: the width of the regularization zone, l_0, is assumed to be dictated by the requirement to resolve the most critical length scale governing the problem. In the case of a samples with a macroscopic pre-existing crack, l_0 can be assigned to be at least one order of magnitude smaller than the size of the initial crack segment. In cases in which the medium presents detectable microstructural features such as distributed microcracks or second phase particles, which can be assumed as locations in which crack propagation is likely to initiate, l_0 can be rather dictated by the requirement to be comparable to the characteristic size of these features. If in the idealized problem discrete heterogeneities are absent, relation 4.50 can be employed to estimate the size of the fracture process zone in the spirit of a semi-brittle failure assumption.

   In general, these requirements imply that the damage zone occupies a narrow region within which the increment in the crack surfaces occurs as the idealization of a process involving the creation and coalescence of multiple microcracks ahead of the existing crack-tip(s). This setting for crack propagation aligns with the assumption of small-scale yielding which is often employed when crack propagation in elastic-plastic solids is described by LEFM principles; in that respect, it is assumed that plastic deformations develop within a small region around the moving crack-tip and cleavage is the main macroscopic failure mechanism. Under these assumption, brittle fracture is therefore governed *K-dominant*-field and the main fracture parameter is the critical energy release rate.

If plastic deformations are taken into account, the choice of l_0 can be carried out by estimating its value as comparable to the characteristic size of the plastic region, *e.g.* the width of the shear band.

4. As mentioned in Section 3., if l_0 is fixed by microstructural requirements and the value for fracture strength is available, relation 4.50 is employed to scale G_c accordingly. If the problem does not suggest any requirement for l_0 then relation 4.50 is employed to estimate its value given $\sigma^0_{c,e}$, G_c and E.

5. It is necessary to carry out a sensitivity analysis on the variation of both the rate of loading and l in order to postulate a rate-dependent scaling law for the stress at softening such as the one proposed in equation 4.44.

6. A rate-dependent scaling law for the tensile strength, such as the one in equation 4.45, has to be obtained through experiments, *e.g.* by means of the split Hopkinson bar, and employed as a calibration baseline to obtain the correspondent scaling for l and η such as those in equations 4.46, 4.48, respectively. It has to be pointed out that if an exponential form for this rate dependent-law is assumed, often the only parameter which has to be measured is $\dot{\varepsilon}_0$ as it is generally found that $n_2 = 0.33$ applies to many brittle material systems.

7. A sensitivity analysis of the model response under various tensile loading rates has to be carried out in order to find the set of γ_i parameters which provide the closest fit to the experimentally-derived scaling law for the fracture strength. It has to be pointed out that this quantitative assessment is provided in terms of maximum stress measured at softening during the simulations, which is assumed to correspond to the strength of the material.

8. A rate-dependent scaling law for the compressive strength has to be obtained. The split Hopkinson pressure bar can be employed as a valuable experimental platform as it has been discussed in section 2.4.1 and will be later demonstrated in section 7.4.1.

9. A sensitivity analysis of the effect of the variation of β on the stress at softening in representative volume elements subjected to compressive load at different rates has to be performed. This allows to obtained a scaling law for the maximum compressive stress with respect to β. It has to be pointed out that the postulation of the law for β might also involve statistical considerations associated the defects distribution, *i.e.* density, mean-spacing and characteristic size.

10. Depending on the complexity of the law postulated for β, a further calibration and validation procedure might have to be carried out such as that proposed in point 7.

11. The triaxiality-based law for the description of the mode of failure transition as introduced in equation 4.6 can be obtained by performing experiments on samples under varying levels of confinement. If a tri-linear scaling law for G_c is

assumed, these experiments reduce to the estimation of the parameters χ_L and χ_U.

It has to be pointed out that in the benchmarks which will follow, the calibration steps 9.-10. have not been included as this would have required the capability of accounting for contact detection between the crack surfaces. However, the effect of the variation of β on the crack patterns and on the measured compressive fracture strength will be shown on the basis of a qualitative analysis.

Chapter 5

Single-mode dynamic fracture

In this section, the ability of the model to capture the rate-dependent failure response under mode-I transient loading conditions is discussed. Results pertaining crack nucleation under remote tension and due to spallation-induced fracture are presented. Moreover, predictions of the rate-dependent failure patterns in a single-edge notched specimen under remote applied surface traction are provided.

5.1 Introduction

Although the model has been developed and implemented with no limitations in simulating fully three-dimensional cases, plane strain conditions are assumed in the following studies in order to reduce the computational costs. It has to be noted that the parameter γ_2 has been chosen equal to 15; variation of this parameter shifts the rate-dependent strength without altering its shape. It has been observed that in a multiple elements setting, higher values of γ_2 provide improved numerical stability as the Laplacian operator assumes non-zero values. The mesh design strategy has been chosen on the basis of the requirement to resolve the regularization length scale l_0 as attempting to resolving the length scale associated with the micro-inertia would require a much finer discretization. Instead, recalling the work of Karedila and Reddy

Parameter	Value
γ_1	0.55
γ_2	15
γ_3	4.25
γ_4	0.35
γ_5	1.3
γ_6	0.45

Table 5.1: Rate-dependent parameters chosen for the simulations

[38], micro-inertia effects are thought to contribute only in the form of additional dissipation. However, it is envisaged that a higher order for the spatial resolution might enable to capture more detailed features of the failure morphology. A mesh sensitivity study will be presented in section 5.3. dedicated to crack propagation.

5.2 Crack Nucleation

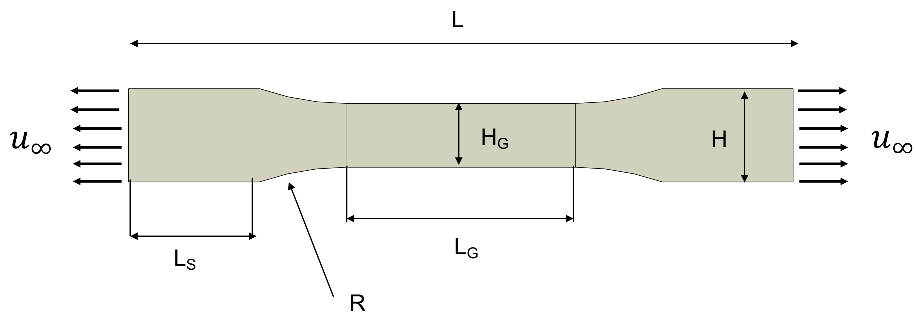

Figure 5.1: Geometry dogbone sample and schematic of loading conditions

In the following, crack nucleation is analysed in a dogbone specimen under remote dynamic tensile loading. The specimen is designed according to ASTM D638 standard for tensile tests and dimensions are listed in table 5.2. The boundary conditions are of the displacement control-type in which the boundaries of the specimen are pulled with linearly increasing magnitude up to a maximum of $u_\infty = 0.1L$. The rate is varied by changing the rise time, t_r, *i.e.* higher rates correspond to smaller rise time. The mesh is designed such that the regularization zone l_0 is discretized by 4 elements. It has been assessed that this choice ensures high resolution in capturing strain localization and phase field evolution as the crack nucleates, along with a convergence in the stress computations. The rate at which the specimen is loaded can be estimated, assuming that a state of reasonable strain/stress homogeneity in the gauge section is established prior to failure initiation, through the relation $u_\infty/(t_r L_G)$. The crack nucleation pattern for different loading rate conditions are presented in Figure 5.2(a). It can be observed that low rates result in phase field growth localizing in the middle of the gauge length within a narrow *damage* zone. As the loading rate is increased the zone of localization widens which physically can be explained by inferring that more micro-cracks are formed in the proximity of the region of highest tensile stress concentration. Upon further increase of the loading rate multiple cracks form at location symmetrically-placed with respect to the main crack in the middle of the gauge section. This is due to multiple stress waves interactions between the loading wave, the existing boundaries and the newly-formed crack surfaces which act as fully reflective boundaries. A rate-dependent evolution in the crack patterns formation was also observed by Klepaczko et. al. [212] in PMMA samples under varying loading rate conditions as reported in Figure 5.2(b). However, in Klepaczko et. al. the sample was fixed at the lower end which therefore leads to the crack to nucleate locations different than those depicted in Figure 5.2(a). It is also observed that the geometry employed by Kepaczko et. al. differs from the one considered here. Nevertheless, the model captures qualitatively the process of first widening of the damage zone and multiple cracking upon further increase in the loading rate.

Parameter	Value [mm]
L	1
H	0.11
L_G	0.34
H_G	0.078
L_S	0.22
R	0.46

Table 5.2: Dogbone specimen dimensions

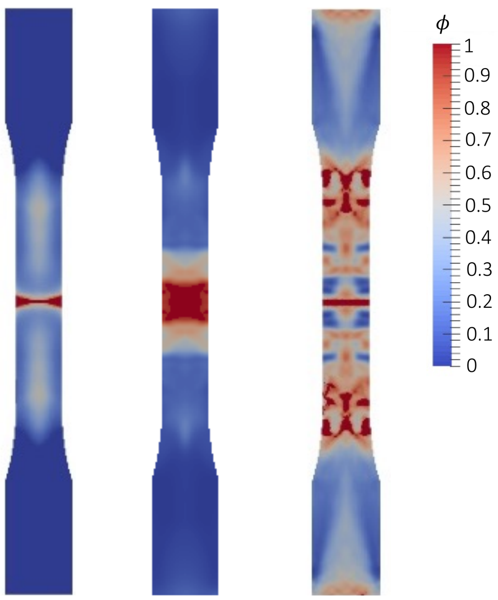

(a) Crack nucleation patterns under various strain rate conditions: $\dot{\varepsilon}_\infty = 0.5ms^{-1}$ (left), $\dot{\varepsilon}_\infty = 10ms^{-1}$ (center), $\dot{\varepsilon}_\infty = 55ms^{-1}$ (right)

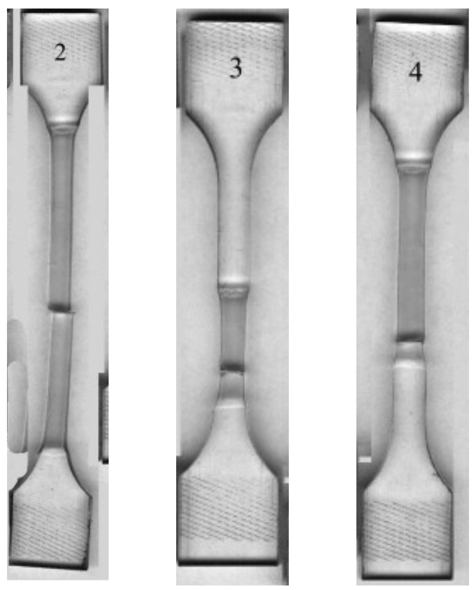

(b) Crack nucleation patterns for PMMA samples under increasing loading rates - reprinted from [212]

Figure 5.2: Crack nucleation in dobgone samples

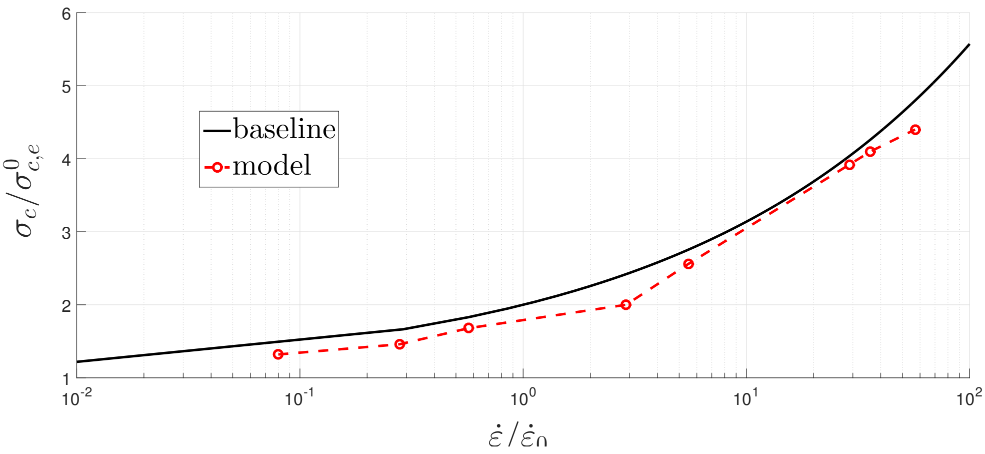

Figure 5.3: Average failure stress in gauge section for several remote strain rate conditions

The strength is measured as the average of the stress component aligned with the loading direction, across the section of the specimen in which failure occurs. Results have been recorded for a series of simulations under different loading rates and they are presented in Figure 5.3. Agreement with the baseline for calibration is observed, therefore suggesting that the model provides quantitative prediction of failure initiation. It has to be noted that the model has been calibrated against the basic assumption that a macroscopic, averaged quantity such as the strength can be associated with a quantitative description of failure locally in the continuum. Nevertheless, the model could be employed to predict more complex crack nucleation scenarios in heterogeneous media, or at lower scales, provided that microstructural effects are included in the adopted formulation for the functions l and η.

Crack nucleation is also simulated in a slender bar with square cross section, subjected to an ideal trapezoidal impulsive load as schematically represented in Figure 5.4. The load is applied in terms of particle velocity on the boundary v_∞, which

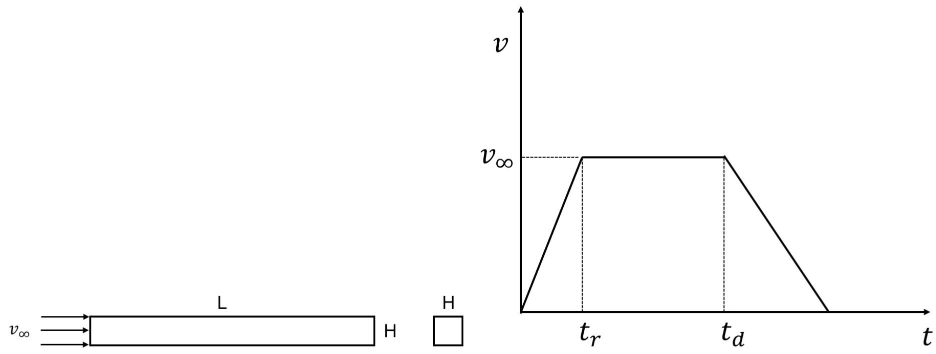

(a) Bar geometry (b) Ideal trapezoidal pulse

Figure 5.4: Boundary value problem for bar subjected to compressive trapezoidal pulse

generates an ideal applied compressive stress wave of magnitude σ_∞:

$$\sigma_\infty = \rho c v_\infty \tag{5.1}$$

This relation refers to the analytical solution for the resultant particle velocity upon passing of an ideal, dispersion-free, elastic-stress wave. The pulse is designed such that the load increases to its maximum amplitude with a rise $t_r = 10^{-6}\ ms^{-1}$, holding this value until unloading begins at time t_d. This is the idealization for a plane impact between the bar and a projectile of length $2(t_d - t_r)c$, made of the same material and cross section. In particular the time t_d corresponds to the instant in which the wave traveling inside the projectile reflects as a tensile from the boundary opposite to the bar/projectile interface causing the contact between the two to cease. The maximum amplitude is assumed such that premature failure - *e.g.* due to local buckling - does not develop. As it can be seen in Figure 5.5(a) as the compressive wave is reflected from the free boundary, spallation due to excessive tensile stress occurs. The location of fracture in the bar is dependent on the length of the pulse as in the proximity of the free boundary the reflected tensile stress has to compete and balance with the original compressive wave, therefore lowering the effective stress level. The time history for

(a) Crack pattern due to spallation

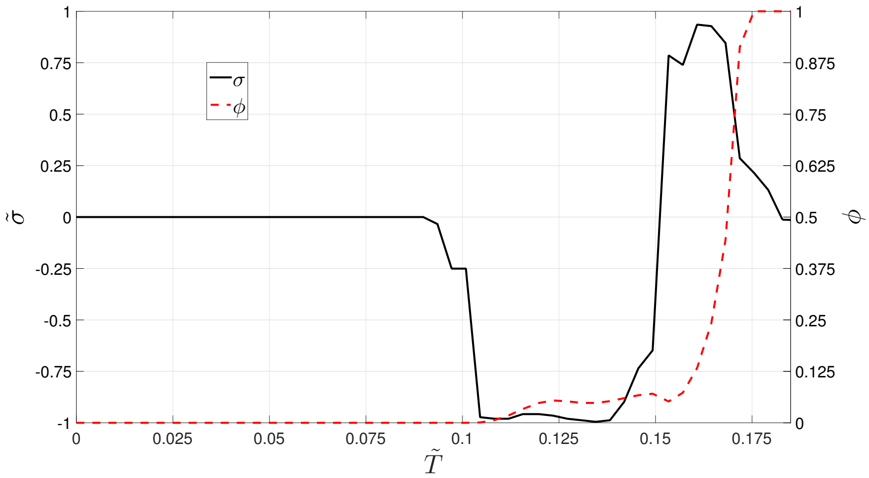

(b) Stress and phase field parameter history at the location of spallation

Figure 5.5: Dynamic spallation for $\tilde{\sigma} = 3.6$

the stress along the loading direction, in the cross section at the location in which spallation occurs is presented in Figure 5.5(b) and compared to its correspondent phase field parameter growth. The stress has been normalized with respect to the correspondent applied σ_∞. It can be seen that as the first train of compressive wave passes through, the stress level rises up to σ_∞ and stays almost constant implying that no significant dissipation effects, due to radial inertia are registered. This result further implies that the slenderness of the bar ensures that the one-dimensional behaviour of the wave propagation is retained. As the wave is reflected from the free end stress unloading and sign reversal is observed. A tensile state of the stress is established which reaches a peak value suitable to trigger the growth of the phase field parameter and correspondent after-peak softening and distinct crack nucleation. This result aligns with several experimental findings such as those reported on alumina-ceramics

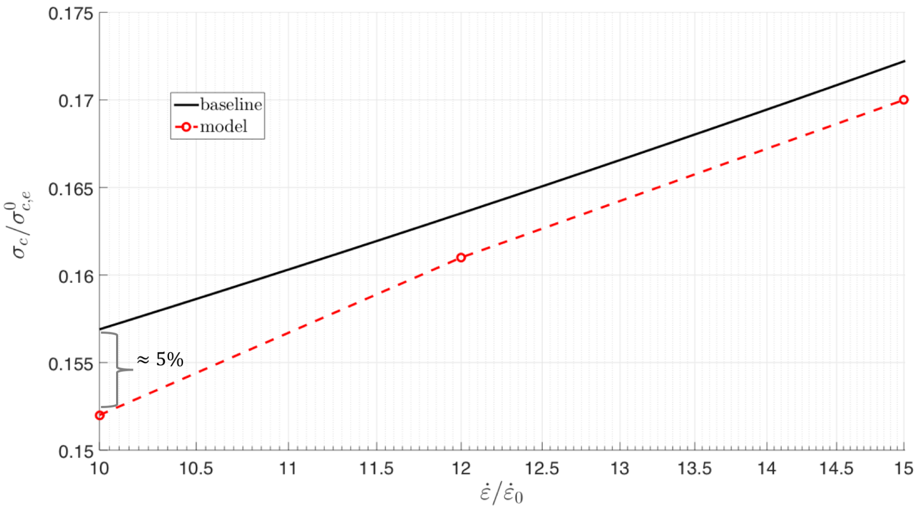

Figure 5.6: Rate-dependent behaviour of stress at softening due to spallation

by Gomez del Rio and Rodriguez Perez [213]. Simulations under different applied boundary velocities v_∞ have been performed and results associated with the peak stress registered at spallation at the correspondent averaged attained strain rate are presented in Figure 5.6. As in the previous benchmark on the dogbone specimen, it is observed that the rate-dependent strength behaviour follows closely the analytical calibration law proposed in Equation 4.45.

5.3 Dynamic Crack Branching

In this section the proposed model is employed to study the dynamics of crack propagation. A pre-notched plate under mode-I, loading conditions is analysed; a schematic of the boundary value problem is presented in Figure 5.7. The choice of this benchmark resembles the testing conditions at the basis of several of the experimental findings, mostly on PMMA, discussed previously; it was remarked how this configuration favours the occurrence of crack branching and inertia instabilities. The boundary conditions are applied in terms of remote traction which ramps over a

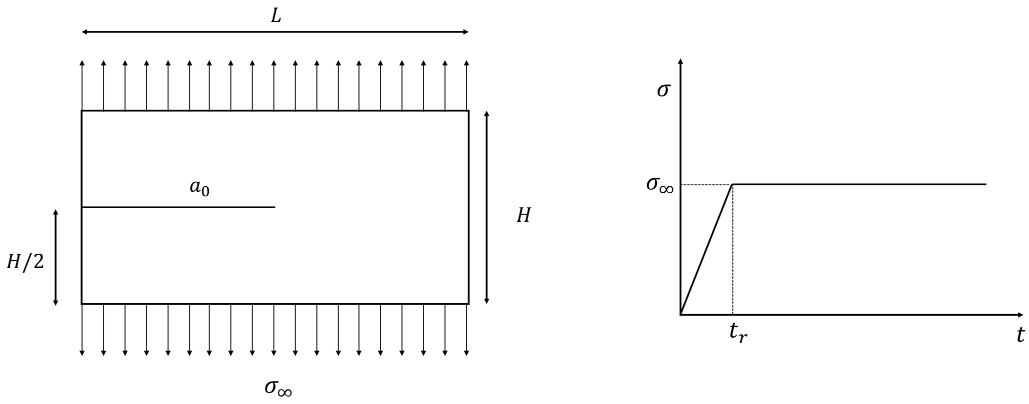

Figure 5.7: Boundary value problem

rising time, t_r, from zero to a constant value, σ_∞. The plate dimensions are chosen to be $L = 1$ [mm], $H = 0.4L$ and $a_0 = 0.5L$. A mesh sensitivity study is carried out for the

	Refinement
Mesh1	h/l_0=0.25
Mesh2	h/l_0=0.5
Mesh3	h/l_0=1

Table 5.3: Meshes with different characteristic element size h

case of loading rate at which crack branching is expected to occur; crack propagation patterns for three different structured meshes (Table 5.3) are compared in Figure 6.2. The main features of crack propagation and bifurcation from the pre-existing crack are captured in all the three cases. However, coarser meshes tend to result in wider phase field localization zones with limited smoothing away from the crack surfaces. The sensitivity of the model on the spatial discretization can be assessed also in terms of recorded crack speed as presented in Figure 5.9(a). Coarser meshes tend to limit the crack speed as also observed in Borden et al. [164]. However, all the three cases present an average drop in the crack speed in the interval in which crack branching occurs, along with maximum attained speed falling below the theoretical

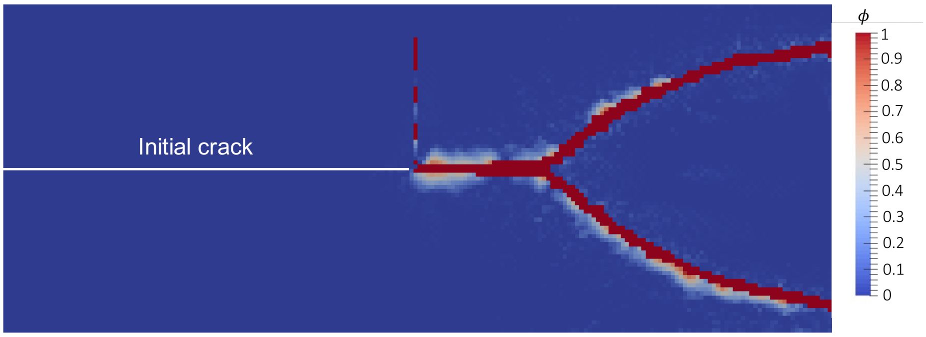

(a) Crack branching for mesh3 at $\tilde{T} = 0.73$

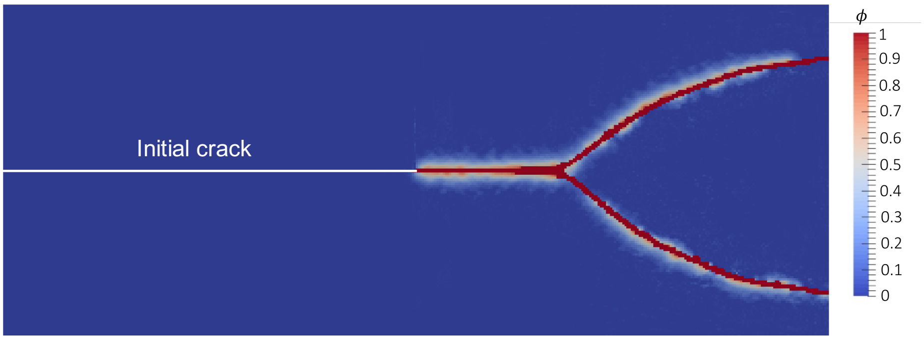

(b) Crack branching for mesh2 at $\tilde{T} = 0.69$

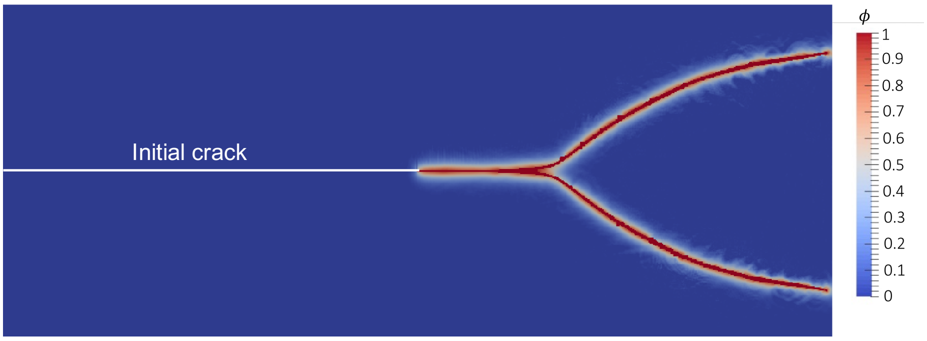

(c) Crack branching for mesh1 at $\tilde{T} = 0.536491$

Figure 5.8: Effect of mesh discretization resolution

limit of 60% the Rayleigh speed. The crack branches fail to reach the boundaries at the same time, with the latter decreasing as a finer discretization is employed. The total energy dissipated, E_d, which includes the contribution due to fracture and viscosity is calculated as:

$$E_d = \int_{\Omega} (\Gamma_{\phi,2} + \eta \dot{\phi}^2) d\Omega \tag{5.2}$$

The computed values are per unit of thickness and have been normalized by a reference value, $G_c L$; this normalisation allows to compare the model against the sharp limit for ideal brittle Griffth fracture. Results for the three different meshes are presented in Figure 5.9(b) and report an increasing dissipation rate corresponding to time intervals in which the crack-tip accelerates from its original position at rest. Concurrently, a lower rate of increase in the dissipation is observed while the crack travels at seemingly steady state conditions with values oscillating around its maximum. The crack branching angle is highlighted in Figure 5.10, showing an approximate value of 36^o consistent with experimental evidences as well numerical simulations on this geometry at this loading rates. The discrepancy with respect to the theoretical value of 60^o obtained by Yoffe [29] could be explained by recalling that in this case a finite geometry, *i.e.* bounded medium, has been considered in contrast to the assumed unbounded conditions in the analysis of Yoffe. These conditions favours the development of a finite, higher order term in the crack-tip stress field, referred as $T - stress$, which acts parallel to the crack plane. The magnitude of this term depends on the distance of the boundaries from the current crack plane as well as on the loading rate. Both these factors dictate the process of stress waves interaction and re-arrangement of the mechanical fields around the crack-tip [23, 214, 215]. The effect of the loading rate is now analysed for the case of $h/l_0 = 0.25$ by keeping t_r fixed and varying the amplitude of the traction on the boundaries. It can be seen that for low rates 5.11(a), with $\sigma_\infty = 0.02\sigma_c$, the propagation path lays along the plane of the initial crack. The loading regime is such that no-significant dynamic instability is developed, otherwise required to promote crack branching. This result aligns with the qualitative behaviour observed in PMMA nothed CT specimens by Murphy et.

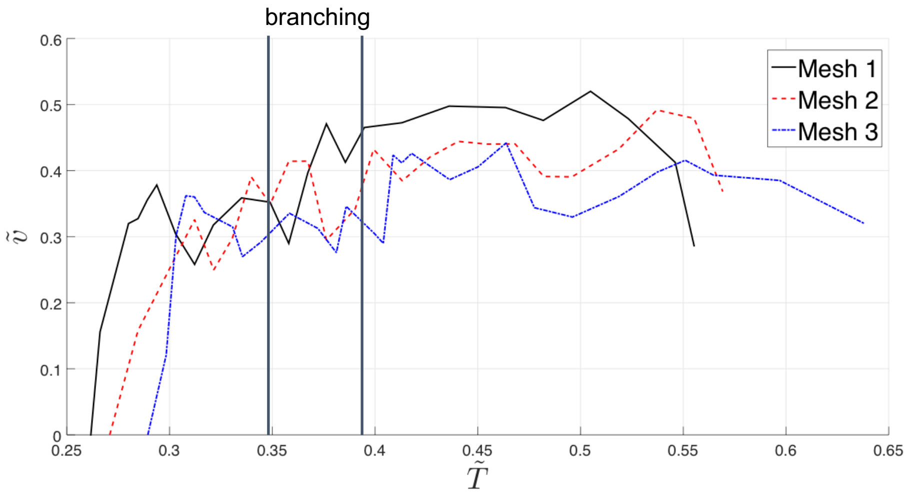

(a) Recorded crack-tip velocities for different meshes. Results have been normalized by a reference value for the Rayleigh wave speed, $v_r = 2125$ mm/ms

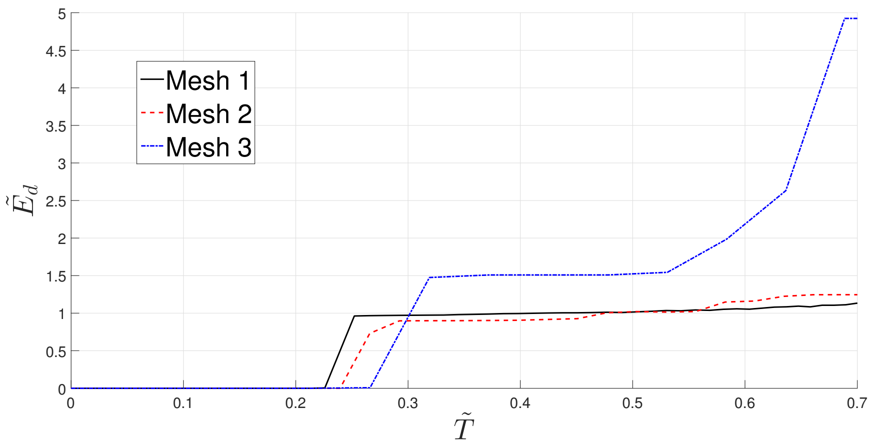

(b) Energy dissipated due to phase field evolution for different meshes.

Figure 5.9: Recorded crack speed and dissipated energy

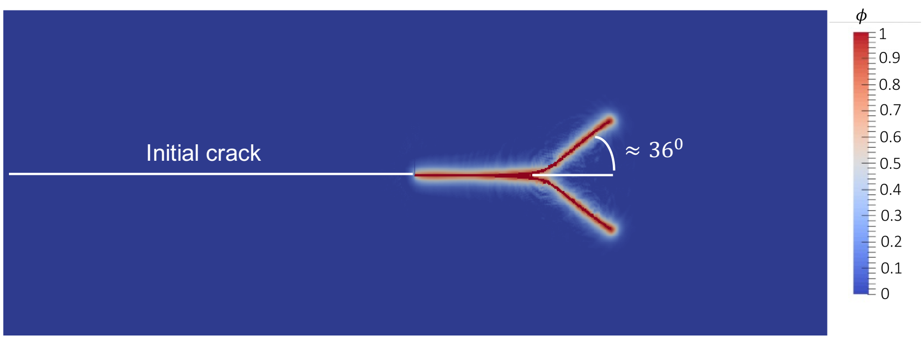

Figure 5.10: Branching angle for mesh1 at $\tilde{T} = 0.4138$

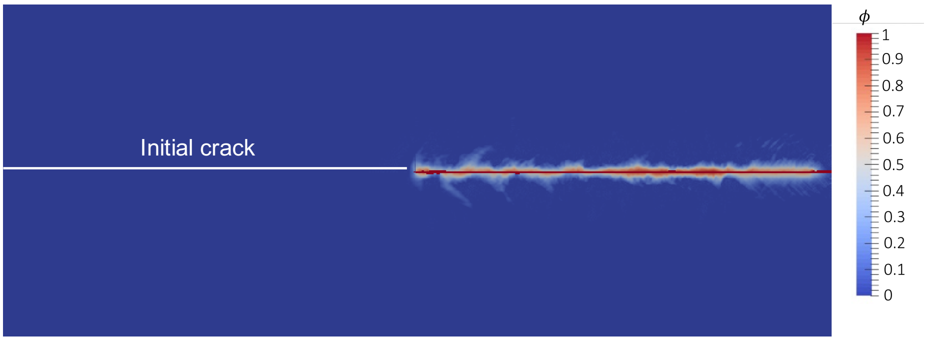

(a) Flat crack pattern (*i.e.* absence of branching under $\sigma_\infty = 0.02\sigma_c^0$ at $\tilde{T} = 1.1728$

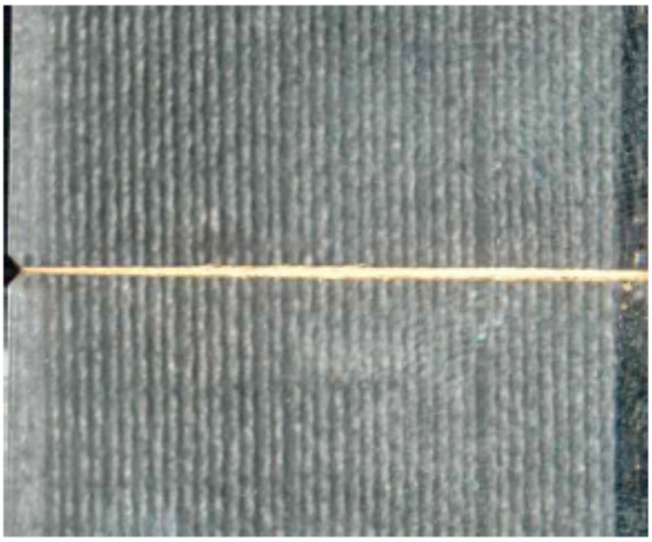

(b) Experimental evidence of flat crack pattern under quasi-static loading conditions in PMMA, SENT specimens - reprinted from Murphy et. al. [216]

Figure 5.11: Crack patterns under seemingly quasi-static loading conditions

al. as reported in Figure 5.11(b). As the rate of loading is increased, by imposing an

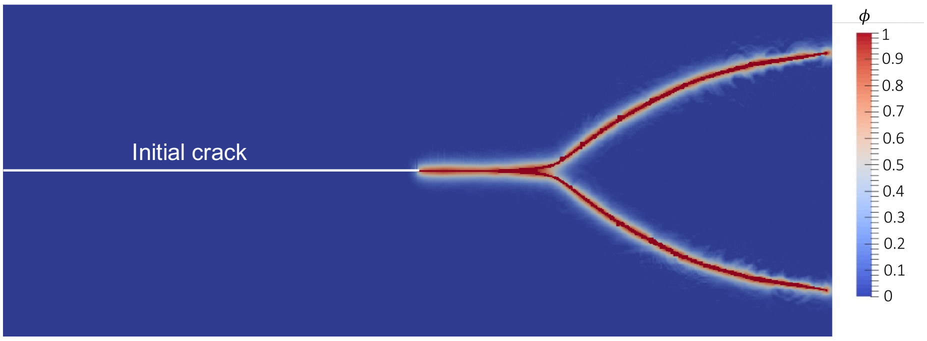

(a) Crack branching under $\sigma_\infty = 0.2\sigma_c^0$ at $\tilde{T} = 0.536491$

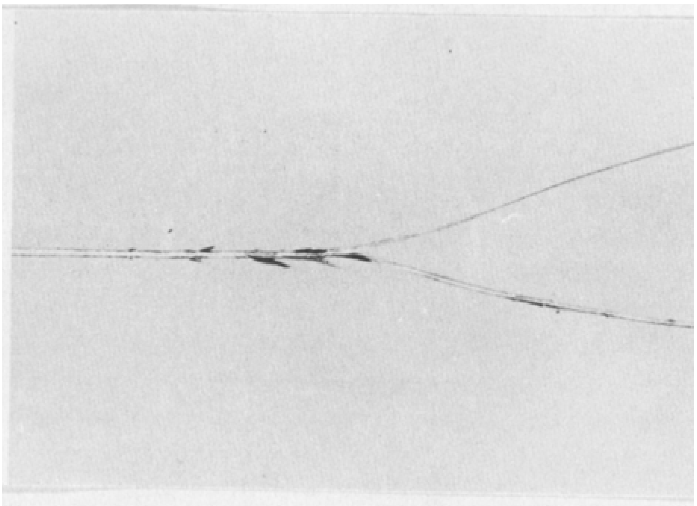

(b) Zoom-in of graph reporting crack branching under *intermediate* loading rate conditions favourable for branching formation in PMMA, SENT specimen - reprinted from Ramulu and Kobayashi [23]

Figure 5.12: Crack patterns under loading rates promoting primary, macroscopic branching

higher traction magnitude, two macroscopic branches are formed as presented in Figure 5.12(a). The branching pattern qualitatively agrees with the pioneering findings of Ramulu and Kobayashi reported in Figure 5.12(b) and closely follows the results obtained by considering this specimen configuration and similar loading conditions by Borden at al. [164] and Schulter at. al. [217]. Upon further increase of the loading rate the formation of distinct macroscopic branching is accompanied by the formation

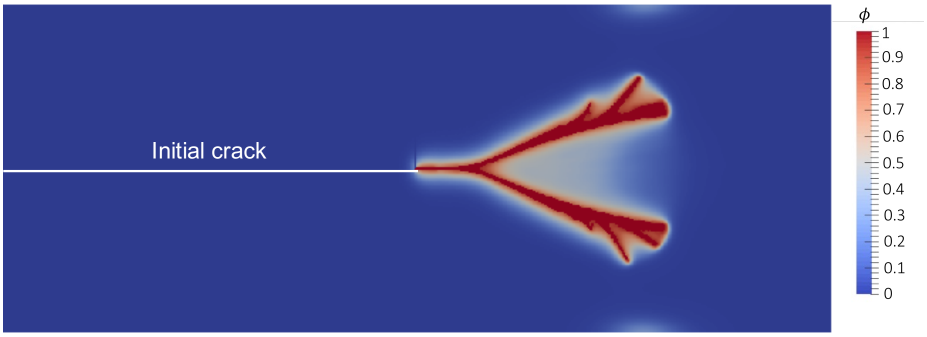

(a) Crack branching under $\sigma_\infty = 0.5\sigma_c^0$ at $\tilde{T} = 0.36$

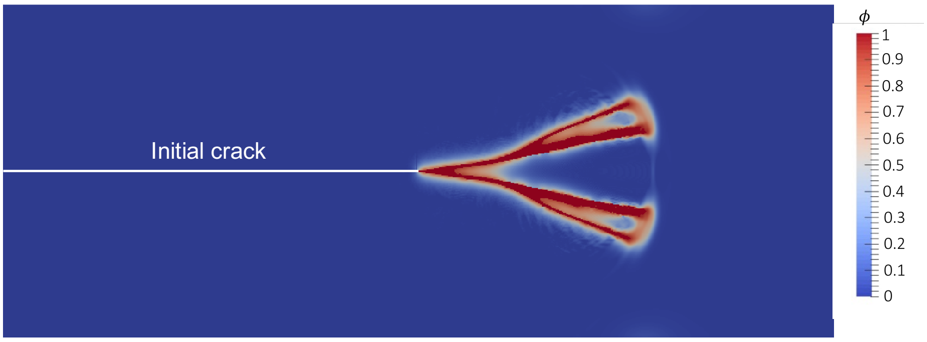

(b) Crack branching under $\sigma_\infty = \sigma_c^0$ at $\tilde{T} = 0.212$

Figure 5.13: Crach patterns under different loading rates

of secondary, smaller in size, branches which diverge from the main propagation path and point towards the upper boundaries in a seemingly symmetric fashion (Figure 5.13(a)). Higher loading regimes lead to an immediate branching formation from the original crack-tip position as reported in Figure 5.13(b). Another pair of macroscopic branches is formed with angle constant with respect to the primary branches while maintaining their respective crack-tip(s) traveling almost at the same speed. These results qualitatively align with the experimental findings reported by Murphy et. al. [216] as reported in Figure. 5.14. A comparison between the model prediction for the case of rate-dependent, as governed by Equation 4.46, and constant, $l = l_\phi^0$, micro-inertia length scale is provided for a case loading rate corresponding to σ_c^0 at $\tilde{T} = 0.212$ and presented in Figure 5.15. It has to be pointed out that the model retains its rate-

Figure 5.14: Example of multiple branching formation under increasing loading rate - reprinted from Murphy et. al. [216]

dependent nature as both l and η assume no-zero values. It can be seen that assuming $l = l_{\phi}^{0}$ does not lead to distinct multiple branching formation with rather a widening of the phase field localization zone (5.15(b)). It can be inferred that, as compared to the case in which l assumes a rate-dependent form (Figure 5.15(a)), high-inertia effects around the moving crack-tips cannot be captured and the only visible failure pattern resembles the situation in which coalescence of multiple micro-cracks, forming around the main branches, occurs.

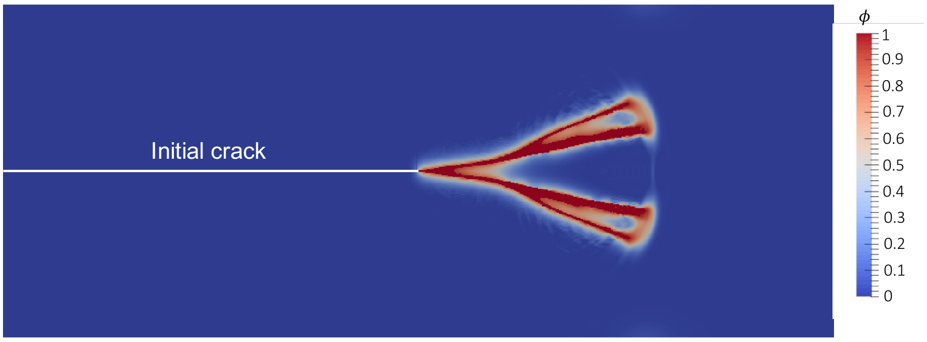

(a) Crack patterns for rate-dependent micro-inertia length scale

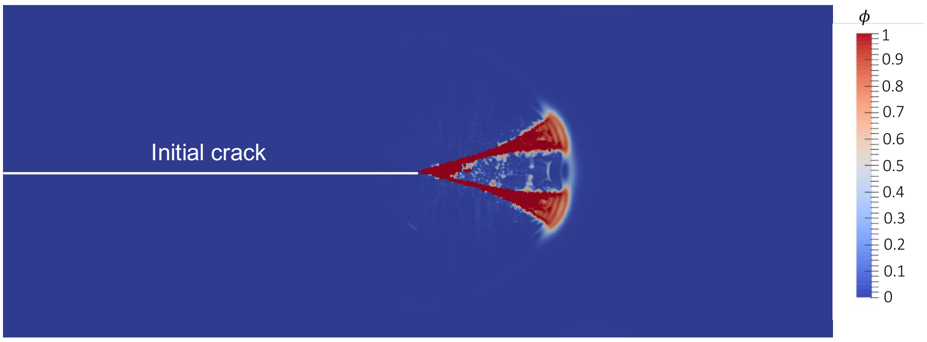

(b) Crack patterns for constant micro-inertia length scale

Figure 5.15: Crack propagation pattern for the case of constant and rate-dependent micro-inertia length scale, under $\sigma_\infty = \sigma_c^0$ at $\tilde{T} = 0.212$

Chapter 6

Mixed-mode dynamic fracture

In this chapter the model is employed to study the fracture behaviour of brittle materials containing pre-existing flaws and subjected to remote dynamic compressive loads. Rate and pressure sensitive mode-of-failure transition is discussed along with the effect of remote confining pressure.

6.1 Introduction

Two benchmark problems are considered to test the ability of the model to simulate crack initiation and propagation under single mode-I compression-induced tensile fracture as well as capture the transition to mode-II fracture under increasing confining pressure. First the model prediction for a single edge notched plate under shear loading is investigated followed by the analysis of a plate containing a centred inclined open flaw subjected to biaxial compression. Plain strain conditions are assumed in the simulations by constraining the deformations of the sample in the out-of-plane loading direction. The material properties are the same as those assumed in the previous chapter (Table 4.1).

6.2 Impact on asymmetric edge-notched plate

6.2.1 Boundary value problem

The problem discussed in this section refers to the experiments performed by Kalthoff and co-workers [39, 40] and discussed in section 2.3. A scaled version of the sample used by Kalthoff [39] and the idealized boundary conditions are schematically represented in Figure 6.1. The dimension of the sample are $H = 0.125mm$, $a_0 = 0.25mm$ and $L = 0.5mm$. It has to be noted that a projectile impact would result in a trapezoidal loading pulse in which the load on the edge is ramped down to zero when the contact between the projectile and the plate ceases to persist. However, in the analysis presented in this section, the load is kept constant after the initial rising time, t_r, as similarly assumed in Borden et. al. [164] and Hofacker and Miehe [188]. It can be recalled that these loading conditions ideally resemble a situation in which the projectile length is much longer than the plate width and closely follow the analysis performed by Mason et. al. [218]. The rising time, t_r is chosen to be L/v_d where v_d is the dilational wave speed of the assumed material. A sensitivity analysis will be discussed on the basis of scaling the applied velocity with respect to the theoretical, *i.e* analytical, critical value for stress at softening, σ_c^0 (equation 4.41a). The equation in 5.1 can be therefore employed. The symmetry of the problem is exploited such that the model is reduced to a plate containing a crack with the lower edged fixed along the vertical direction. The finite element discretization is designed such that $h/l_0 = 4$ where h is the characteristic element size. The material properties are those employed in the benchmark regarding crack branching under mode-I tensile loading conditions discussed in the previous chapter.

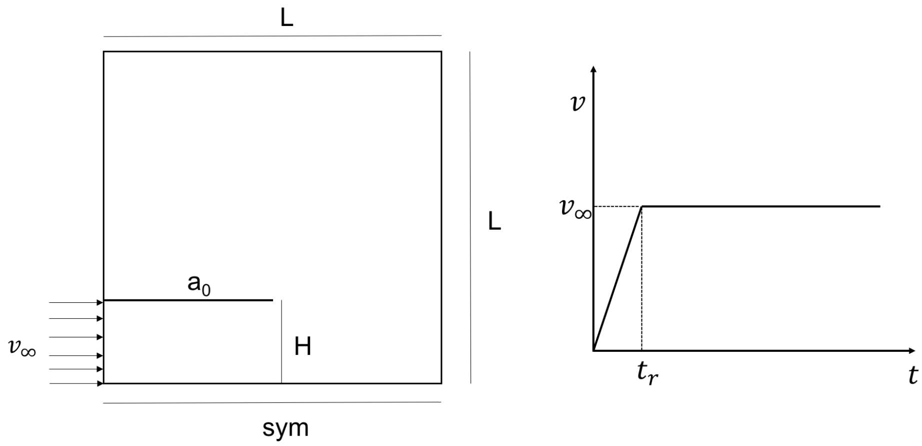

Figure 6.1: Boundary value problem for edge-on impact experiment

6.2.2 Results

Results pertaining the model prediction under different loading rate regimes are now discussed. In this analysis a coefficient of mode-mixity $\beta = 9$ is assumed and the effect of its variation shall be addressed later in the chapter. Results will be commented in terms of applied remote stress although the boundary conditions are applied in terms of nodal velocities. The simulations are considered valid until the pre-exiting crack surfaces come into contact due to multiple wave reflection within the medium. This condition would otherwise have required a numerical platform able to deal with contact detection. At rates lower than $\sigma_\infty/\sigma_c^0 = 0.8$ no crack propagation initiation has been observed at the initial crack-tip. This result aligns with the findings on polycarbonate and steel reported by Ravi-Chandar et. al. [41, 42] and Kalthoff et. [39] respectively. It was argued that relatively low impact velocities do not favour *ductile-to-brittle* transition and result only in the formation of a localized plastic region around the initial crack-tip. Given the limitation of the present model to only brittle deformation this result is interpreted in terms of energy deficiency supplied

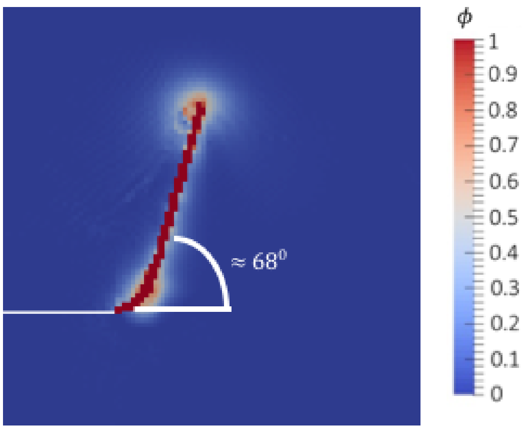

(a) Crack propagation pattern for $\sigma_\infty = 0.83\sigma_c^0$ and $\beta = 9$

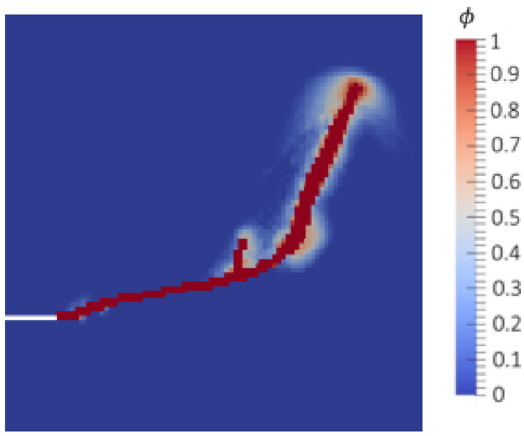

(b) Crack propagation pattern for $\sigma_\infty = 0.95\sigma_c^0$ and $\beta = 9$

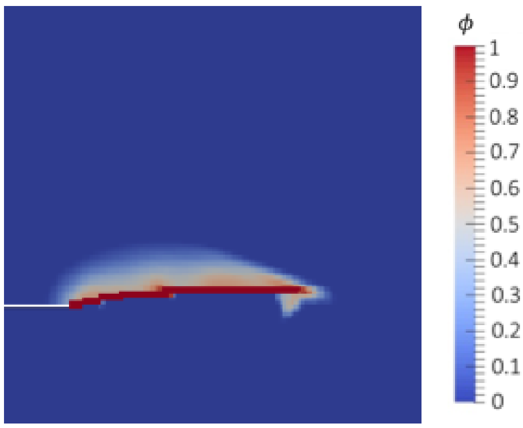

(c) Crack propagation pattern for $\sigma_\infty = 1.1\sigma_c^0$ and $\beta = 9$

Figure 6.2: Crack propagation pattern under increasing loading rate conditions

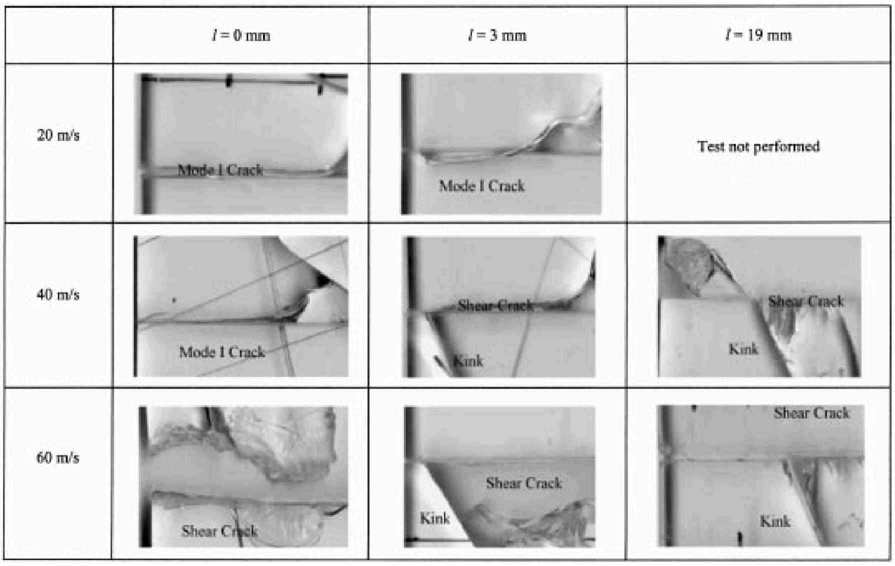

Figure 6.3: Example of mode of failure transition in single edge notched PMMA plates subjected to increasing impact velocity - reprinted from Ravi-Chandar et. al. [41]

to the system to drive the initiation of failure, as can be inferred from the results on PMMA reported by Ravi-Chadar et. al. [41]. At impact velocities corresponding to $\sigma_\infty/\sigma_c^0 = 0.83$ mode-I fracture initiation and propagation is observed and reported in Figure 6.2(a). At this loading regime the mechanical state of the crack-tip field is such that an energetically-favourable tensile opening failure mode arises and crack propagation is governed by the maximum hoop stress criterion of Erdogan and Sih [219]. The crack propagates at an angle of approximately 68^0 in accordance with the linear elasto-dynamic analysis of Lee and Freund [220] which retains its validity over a time-interval of $T < 3a_0/v_d$. This result scales accordingly to that obtained by Borden et.al. [164]. Upon increase of the loading rate up to $\sigma_\infty/\sigma_c^0 = 0.95$ a transition to a mixed-mode crack propagation fashion is registered. The first extends along a path with an angle much lower than the previous case and subsequently diverges towards mode-I-*like* path due to the interaction of the newly formed crack surfaces with the tensile stress waves reflected from the far-right free boundary. The application of a load corresponding to $\sigma_\infty/\sigma_c^0 = 1.1$ leads to a distinct failure mode transition which can be observed in Figure 6.2(c). Under high loading amplitudes, shear-dominant driven crack propagation occurs. Kalthoff [39, 43] and Ravi-Chandar observed this *brittle-to-ductile* transition in materials undergoing shear banding formation at these regimes as a result of increased biaxial-compression at the crack-tip. However, as later argued by Ravi-Chandar [41] on the basis of its finding on PMMA reported in Figure , in the context of brittle materials in which strain localization due to plastic yielding is absent, this transition in the mode of failure has to be interpreted as the result of an increased pressure-driven constraint at the crack tip. In turn, crack opening along the line of maximum circumferential stress is suppressed and instead crack propagation along the direction of maximum shear is favoured. This argument found fertile ground for comparison with the Broberg's conjecture [44] in which failure mode transition in brittle solids subjected to biaxial compression was observed. The original experiment performed by Broberg will serve as a benchmark in the next section. It can be concluded that the model captures the essential features of failure mode transition as observed by Ravi-Chardar [41] whose results are depicted in Figure 6.3.

Moreover, it has to be noted that the progressive transition from mode-I dominant fracture to shear-driven fracture is accompanied by a progressive increase in the energy dissipated associated with the evolution of the phase field parameter, as reported in Figure 6.4. This result supports the argument that for increasing loading rate the triaxiality around the crack-tip increases, therefore leading to the function $\tilde{G}_c$ assuming higher values, *i.e.* corresponding to the critical energy release rate for crack

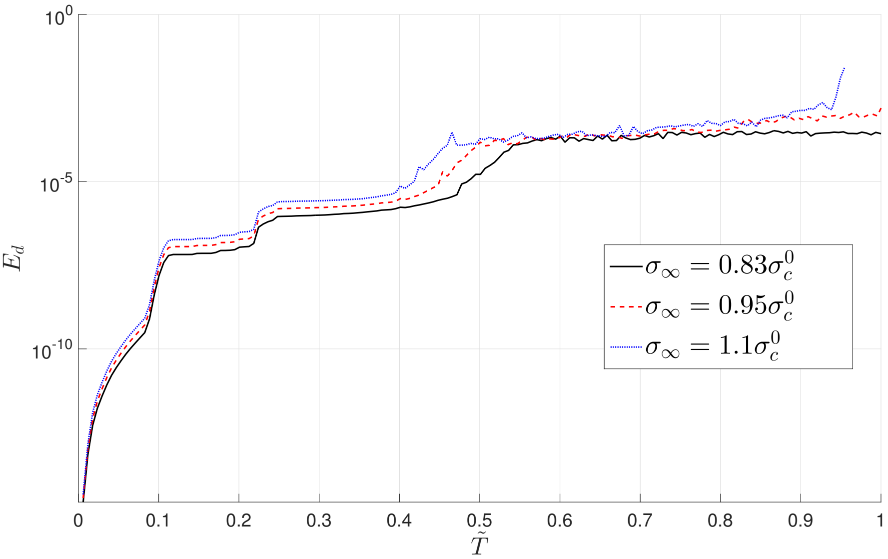

Figure 6.4: Normalized dissipated energy for the case of $\beta = 9$ and increasing impact velocity

propagation under mode-II.

Importantly, it can also be observed that the crack-tip velocity increases as a transition to shear crack propagation occurs, as reported in Figure 6.5. This result aligns with the findings of Rosakis et. al. [221], Ravi-Chandar et. al. [41] and Geubelle and Kubair [222] who showed that if this transition in the mode of failure can be triggered, intersonic crack propagation, *i.e.* $v_{tip} \approx c_r$, can be attained in nominally homogeneous solids.

The effect of the variation of the parameter β is now discussed and results for three different loading rate compared, as summarized in Figure 6.6. It is shown that for low loading rate conditions, with applied $\sigma_\infty/\sigma_c = 0.83$, the crack propagates in a mode-I fashion at an angle of 68^0 with respect to pre-existing crack plane. Moreover, lower values for β results in a rather kinking mode-I path which initiates from a seemingly mixed-mode initial propagation path with low angle. This behaviour is dependent on the dimension of the notch and becomes less pronounced as higher values for β are

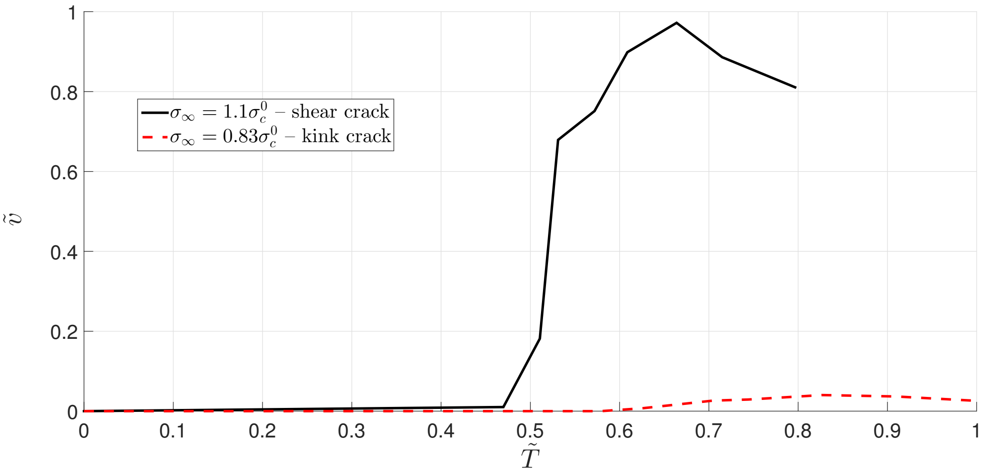

Figure 6.5: Recorded crack-tip velocity for the case of kinked tensile and shear crack propagation

assumed. As the load is increased, up to $\sigma_\infty/\sigma_c = 0.95$ this feature is retained across the whole range of cases considered for β. At this regime, a high value for mode-II crack propagation, *i.e.* $\beta = 25$ leads to a less pronounced decrease in the crack propagation angle along with a widening the of the phase-field localization zone with no-branching occurring. Conversely, assuming $\beta \leq 16$ leads to a more evident mixed-mode crack propagation scenario as well crack branching as observed by Bertram and Kalthoff [223]. At higher loading rates, *i.e.* $\sigma_\infty/\sigma_c = 1.1$, more severe conditions for pure mode-II fracture propagation, *i.e.* $\beta \geq 16$ mixed-mode crack propagation is observed along with multiple branching formation.

Next, results pertaining the model in which the micro-inertia length scale is considered to assume a small, constant value as proposed in Equation 4.38, are compared against the formulation employed so far in which l has been calculated according to the non-trivial law proposed in Equation 4.46. It can be argued that for the rates considered here, the latter form will result in higher values for l. It has to be pointed out that this further implies that the viscosity assumes a constant value $\eta = 10^{-12}$ in

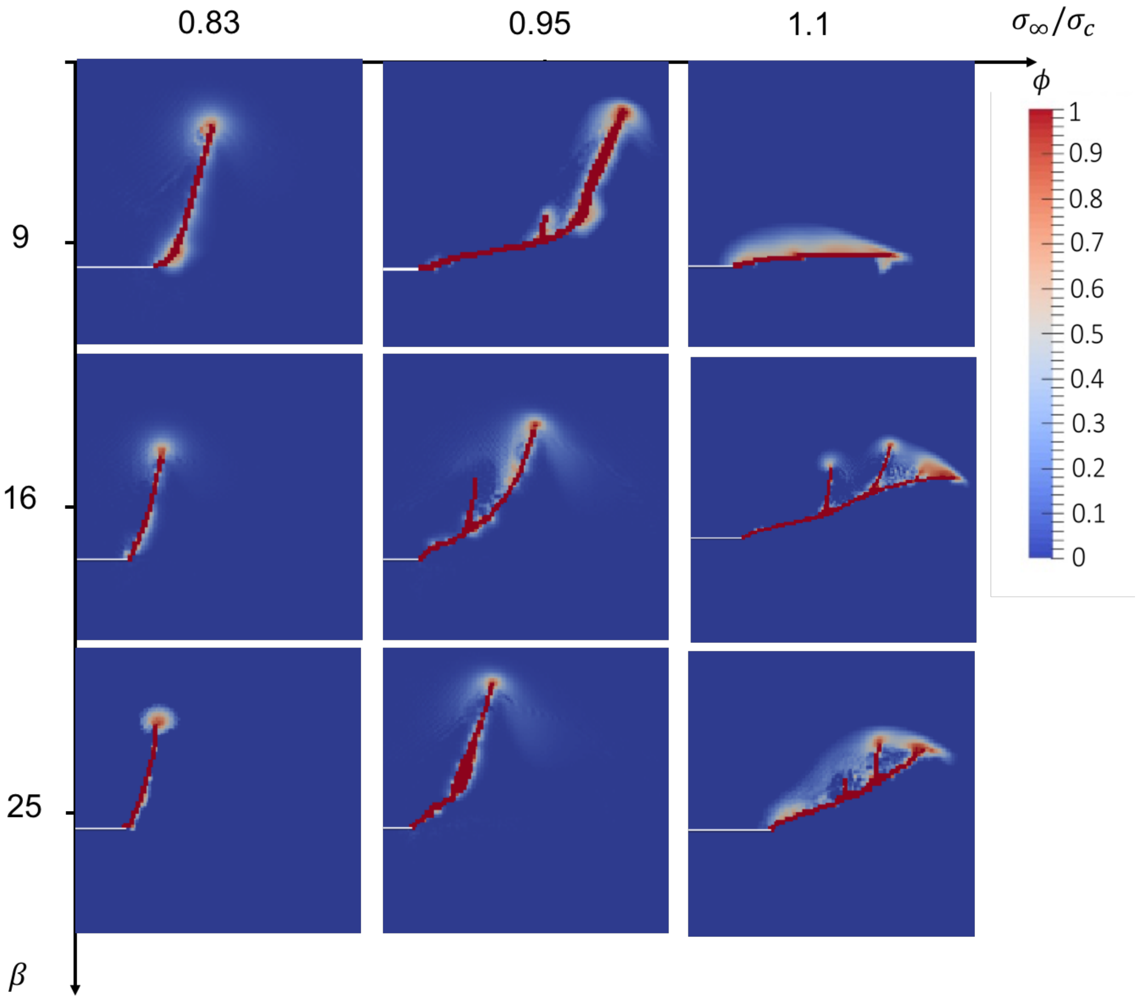

Figure 6.6: Crack patterns for different β at different impact velocities

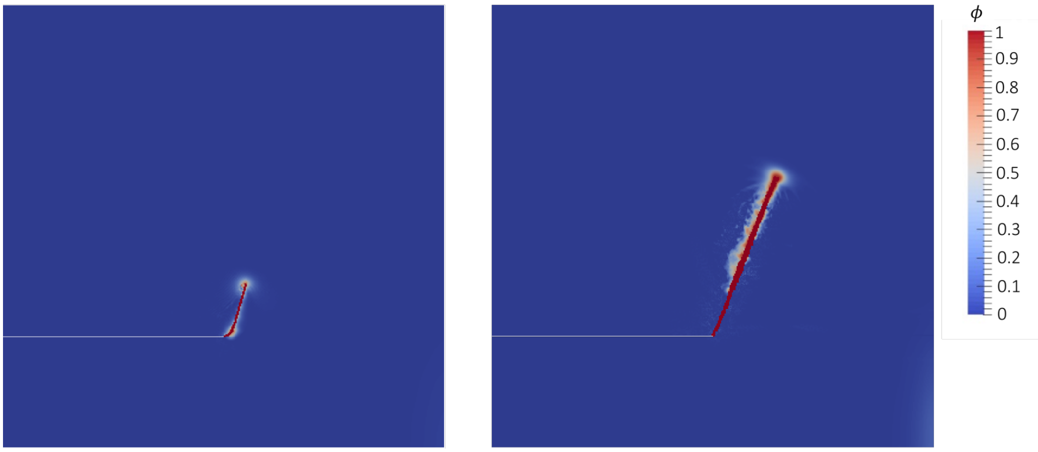

Figure 6.7: Crack propagation pattern for the case of constant (right) and rate-dependent (left) micro-inertia length scale

the former analysis while the rate-dependent law obtained in Equation 4.48 is recalled in the latter case. The crack propagation patterns for the two cases are presented in Figure 6.7. The loading condition and mode-mixity coefficient are assumed to be $\sigma_\infty/\sigma_c = 0.83$ and $\beta = 9$, respectively. It can be seen that assuming $l = l_\phi^0$ results in higher value for the attained crack-tip velocity as opposed to the case in which the scaling depends upon the strain rate (6.8(a)). This is further supported by observing that the energy dissipated due to phase field evolution attains higher values when l scales with the rate, as shown in Figure 6.8(b). This implies that a growing *mass-like* effect, associated with the growth of l from its original lower bound l_ϕ^0, increases the energy to be supplied to the system over time in order to create a fully-developed crack surface. Difference in the crack propagation initiation is also observed and highlighted in Figure 6.9. A rate-dependent form for l results in a rather mixed-mode initiation propagation segment. This can be explained by inferring that the material surrounding the compressive-dominant field at the crack-tip is in a tensile, high rate, stress state to which higher value for l are associated. This in turn implies that the phase field parameter evolution in that region is slowed down. Therefore the crack momentarily finds a more energetic-favourable path to grow along the direction of maximum shear which is under pure-compression. However, as the material at the tip is further loaded, the crack kinks towards the mode-I preferred propagation path. It can be observed that this effect is absent when $l = l_\phi^0$ is constant everywhere in which circumstances the crack propagation initiation path lies along the direction which maximizes the mode-I stress intensity factor. Similarly, as higher applied load conditions are considered with $\sigma_\infty/\sigma_c = 1.1$ no distinct mode of failure transition is observed when $l = l_\phi^0$ as shown in Figure 6.10. In particular, the value for l in the surrounding material under tension does not guarantee the condition for slow evolution of the phase field parameter along the direction of maximum hoop stress as compared to the material element placed along the direction of maximum shear. This result supports the importance of considering the micro-inertia length scale a rate-dependent quantity as needed to obtain a proper characterization of the failure mode transition which occurs under high rates of loading.

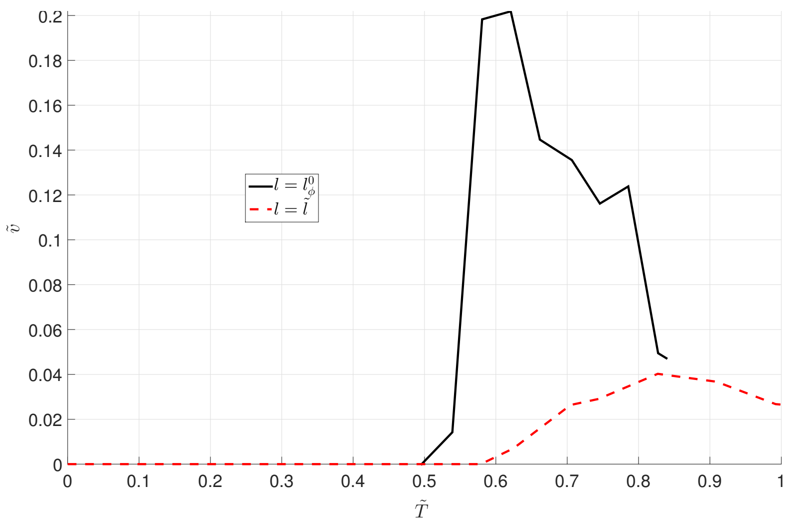

(a) Recorded crack-tip velocity

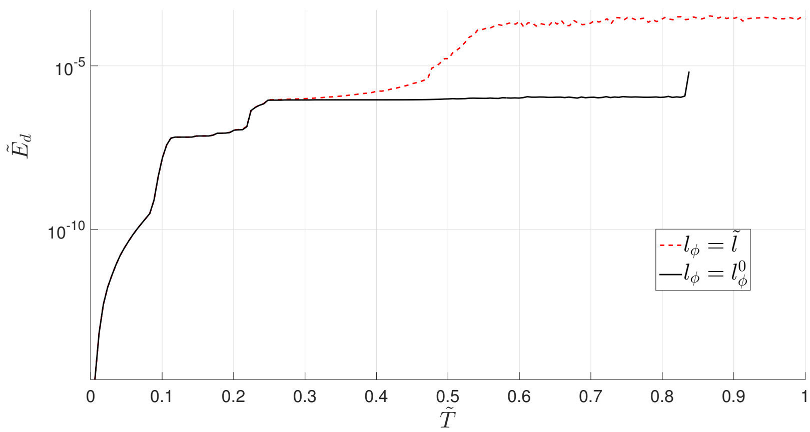

(b) Dissipated energy associated with phase field evolution

Figure 6.8: Comparison between constant and rate-dependent micro-inertia length scale

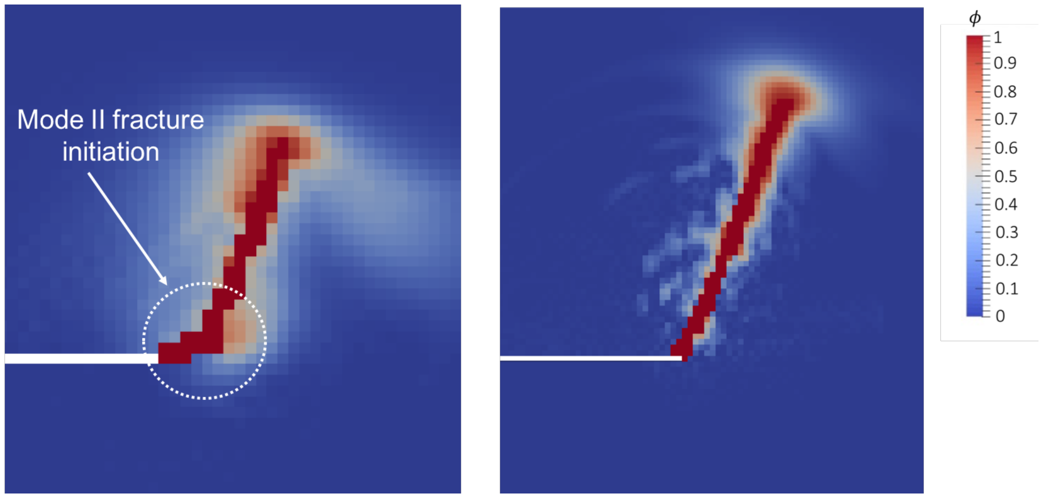

Figure 6.9: Crack initiation for the case of constant (right) and rate-dependent (left) micro-inertia length scale

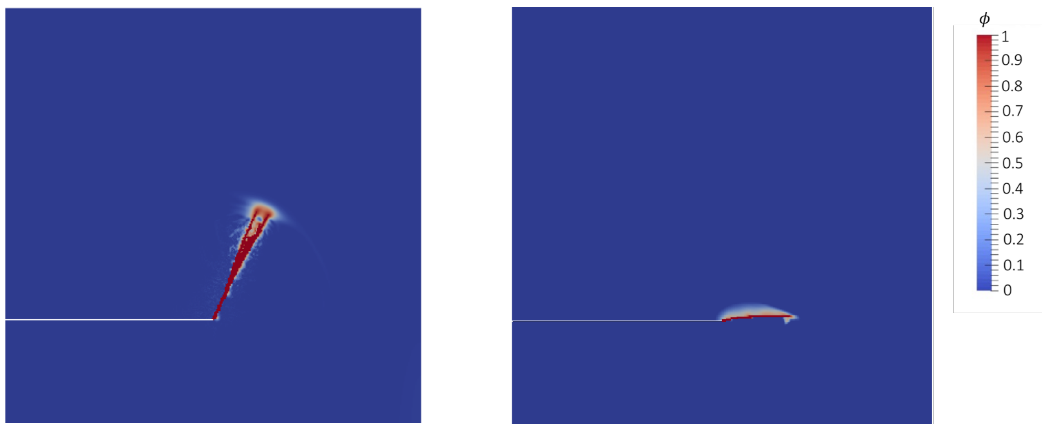

Figure 6.10: Crack pattern at impact velocity, $v = 1.1v_c$ for the case of of constant (left) and rate-dependent (right) micro-inertia length scale

6.3 Plate containing a centred open flaw under bi-axial compression

6.3.1 Boundary value problem

In this section the model is employed to study crack initiation and propagation in a plate containing a single, initial, inclined open flaw, subjected to biaxial compression. As in the previous section, the term crack will be used instead of flaw indistinguish-

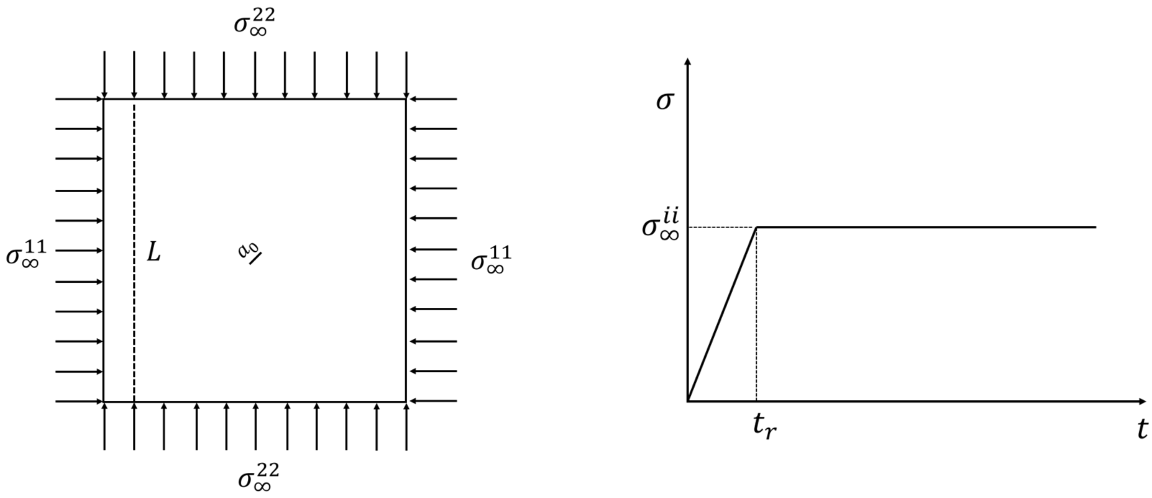

Figure 6.11: Schematic of boundary value problem for center-cracked plate under biaxial compression

ably. The benchmark problem resembles the experimental investigations carried out by Broberg [44] on PMMA plates. A schematic representation of the boundary value problem at hand is presented in Figure 6.11. The plate has a square configuration with $L = 1mm$. The initial crack has length $a_0 = 0.03L$ and is inclined of 45^0 with respect to the direction of the applied remote load. The load is assumed to ramp to a constant amplitude σ_∞^{ii} with rising time $t_r = 7 \cdot 10^{-4}\tilde{T}$. The mesh is designed such that corresponds to $h_e/l_0 = 4$ in the region surrounding the initial crack transitioning towards a coarser, structured, discretization in the proximity of the boundaries. It has to be noted that, the boundary value problem considered in this section closely follows an extensive series of studies proposed in the literature which refer to the investigation of the initiation of primary and secondary cracks from isolated flaws in rock-like materials [224, 225, 226, 227, 228] and brittle polymers such as PMMA [229, 230]. The former type of cracks is also usually refer to as tensile or wing cracks while the latter are described as shear cracks. A schematic representation, summarizing the morphology of types of potential crack patterns, has been provided by Bobet

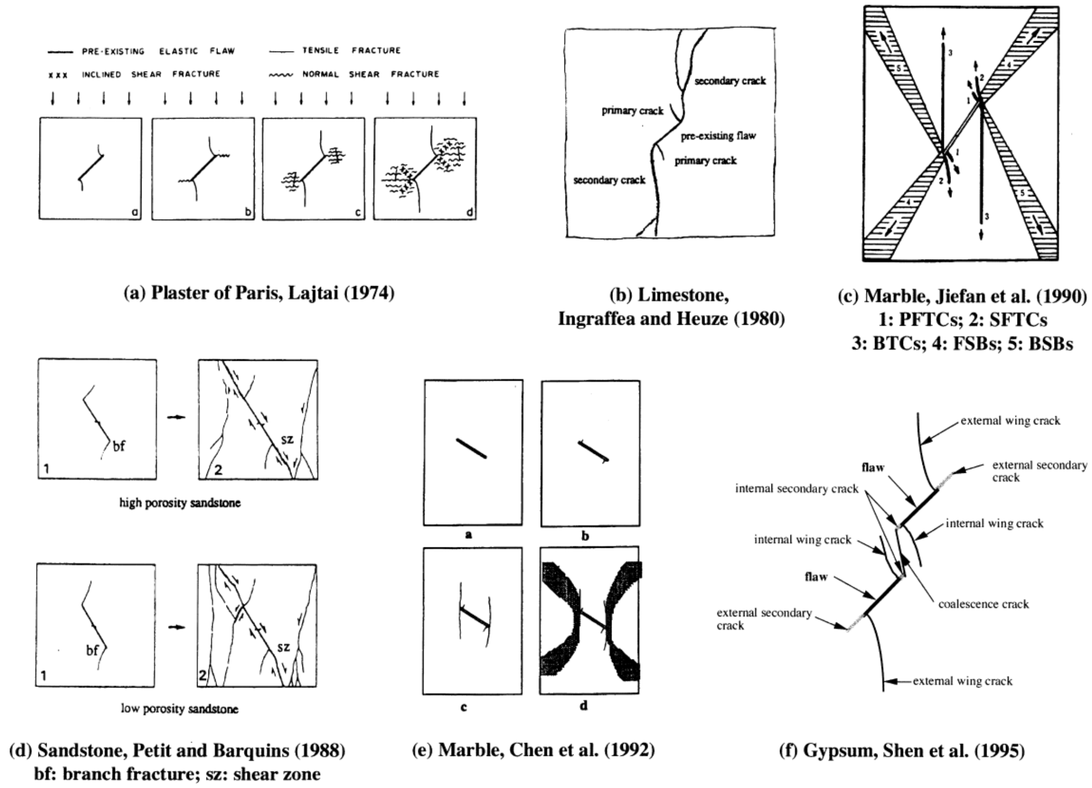

Figure 6.12: Schematic of potential crack patterns arising in brittle solids under remote compression containing isolated flaws - reprinted from Bobet [224].

[224] by collecting experimental evidences from the literature and reported in Figure 6.12.

6.3.2 Results

In the following, results concerning the predicted crack paths under confined and unconfined compressive loading conditions are presented. Firstly, results concerning the case of increasing loading rate without confinement, *i.e.* $\sigma_\infty^{11} = 0$, will be examined. A mode-mixity parameter $\beta = 16$ is assumed unless stated otherwise. It can be seen in Figure 6.13(a) that under moderate loading regimes a tensile, wing crack, is initiated from the tips which tends to align with the principal direction of the applied load. This

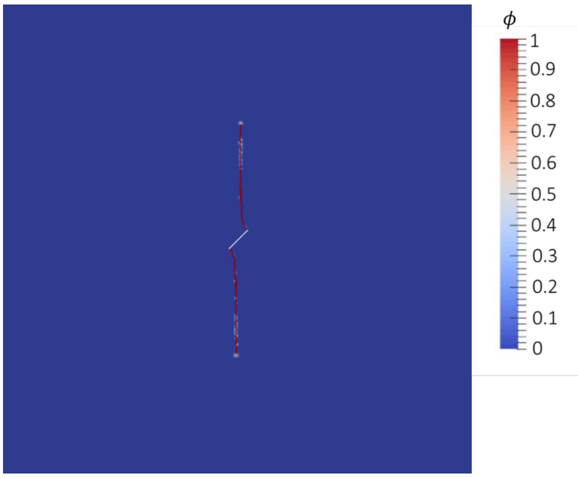

(a) Crack patterns for the case of $\sigma_{\infty}^{22}/\sigma_c^0 = 2.5$

(b) Experimental evidence of wing crack propagation in PMMA samples - reprinted from Ingraffea and Heuze [226]

Figure 6.13: Crack patterns under low rate of compression and without confinement

result aligns with several experimental findings among which those by Ingraffea and Heuze [226] are reported in Figure 6.13(b). As far as theoretical studies are concerned, McClintock and Walsh [231] proposed a modification to the Griffth theory in order to account for the case of single inclined, ideally flat, closed crack under remote compression. Later this model was extended by Ashby and Hallam [232] to account for multiple interacting flaws as well rate-dependent effects by Horii and Nemat-Nasser [48]. It has to be noted that while in the *wing-crack* model the direction of crack propagation is mainly predicted as a result of the frictional conditions between the crack surfaces, here it is dictated by the state of triaxiality at the tip as discussed by Lajtai [225]. As the applied load increases a seemingly mixed-mode crack propagation initiation and growth is observed as shown in Figure 6.14(a). The crack propagation direction tends to align parallel to the direction of the initial crack, implying that the high state of compression at the tips favours the localization and growth of the

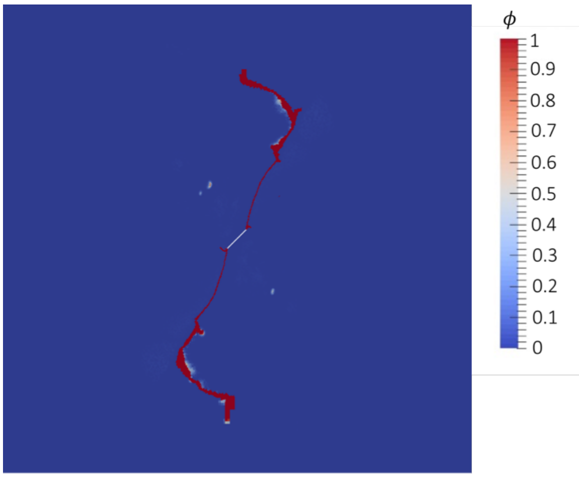

(a) Crack patterns for the case of $\sigma_{\infty}^{22}/\sigma_c^0 = 5.0$

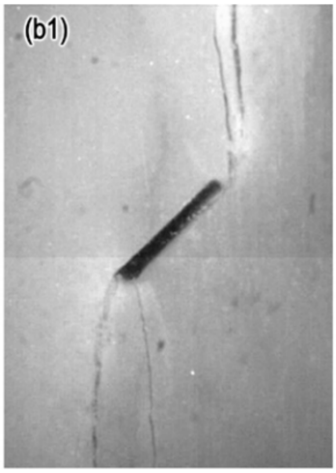

(b) Example of horsetail crack formation in rock sample under increasing loading rate - reprinted from Li and Wong [233]

Figure 6.14: Crack patterns under increasing rate of compression and without confinement

phase field parameter within the material elements closer to the region of maximum shear. As the crack extends and diverges from the original tips, it starts curving and aligning towards the direction of the applied remote load shaping in a horsetail crack as observed by Li and Wong [233] (Figure 6.14(b)). Moreover, the formation of secondary small cracks, as highlighted in Figure 6.15, almost perpendicular to the plane of the initial crack, is registered.

The effect of active confinement, implying that $\sigma_{\infty}^{11} \neq 0$, is now analyzed and results presented in Figure 6.16. The vertical load is assumed to be $\sigma_{\infty}^{22}/\sigma_c^0 = 2.5$. Low level of confinement, with $\sigma_{\infty}^{22}/\sigma_{\infty}^{11} \approx 7.5$, reported in Figure 6.16(a), does not lead to any change in the crack pattern configuration while a decrease in the crack growth speed is observed. This can be inferred by noticing that the length of the ligament is smaller, although at a later stage, than the corresponding unconfined case (Figure 6.13(a)).

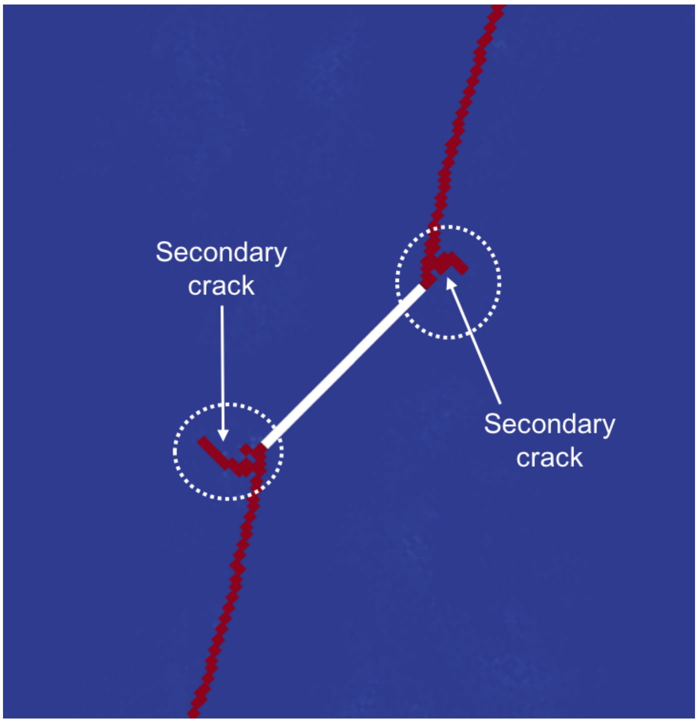

Figure 6.15: Secondary cracks

Moreover, it can be seen in Figure 6.16(b) that for increasing level of confinement a clear transition, from predominant tensile-wing to shear crack growth, is registered at values of $\sigma_\infty^{22}/\sigma_\infty^{11} \approx 5$. Further increase in confinement up to $\sigma_\infty^{22}/\sigma_\infty^{11} = 2$, leads to a distinct shear-driven crack which grows along the direction of maximum shear as depicted in Figure 6.20(b). This result closely follows the findings reported by Broberg [44], here presented in Figure 6.17(b). The development of this crack pattern can be explained by recalling that higher confinement leads to the establishment of a high level of triaxiality, presumably $\chi > \chi_u$. This implies that growth of the phase field parameter is more favourable in the material elements along the direction of maximum shear which possess a higher *driving force* for crack propagation which exceeds the resistance scaled with $\approx \beta Gc$. Moreover, equal biaxial loading conditions, *i.e.* $\sigma_\infty^{22}/\sigma_\infty^{11} = 1$, leads to shear crack initiation and initial propagation with the crack

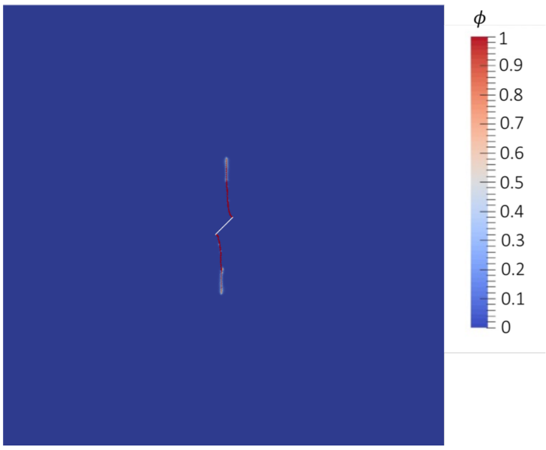

(a) Crack patterns for the case of $\sigma_\infty^{22}/\sigma_c^0 = 2.5$ and $\sigma_\infty^{11}/\sigma_c^0 = 0.35$

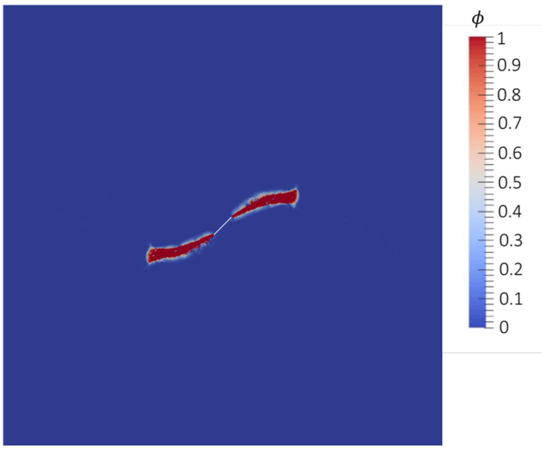

(b) Crack patterns for the case of $\sigma_\infty^{22}/\sigma_c^0 = 5.0$ and $\sigma_\infty^{11}/\sigma_c^0 = 1$

Figure 6.16: Crack patterns under different level of confinement

subsequently splitting in two major branches, presumably because of the interaction between the newly-created crack surfaces and the boundaries; a similar crack pattern was observed in aluminium plates under the same loading configuration by Broberg [44] (Figure 6.18(b)).

Next, the effect of the variation of material parameters governing the mixed mode behaviour of the assumed generic brittle material is examined. In the spirit of the analysis carried out in the previous section, the effect of the variation of β on the resulting crack pattern configuration is presented in Figure 6.19. The plate is considered under biaxial loading conditions such that $\sigma_\infty^{22}/\sigma_\infty^{11} = 2$. It can be seen in Figure 6.19(a) that for materials which have a lower ratio between mode-II and mode-I fracture toughness, *i.e* $\beta = 9$, the model predicts the formation of two distinct pair of secondary cracks. This result can be explained by inferring that lower β does not contribute with enough resistance to phase field growth given the available driving force, therefore establishing the condition for crack propagation before this is reached within

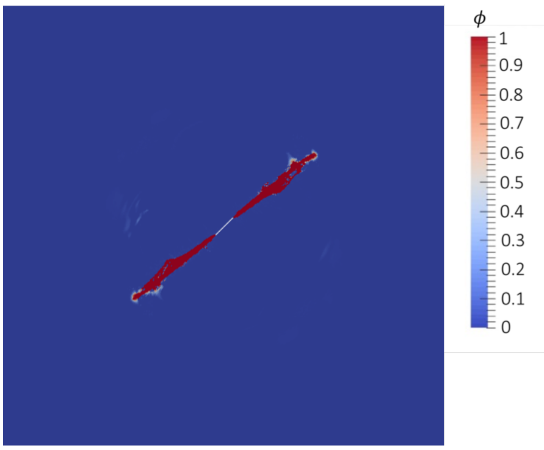

(a) Crack patterns for the case of $\sigma_\infty^{22}/\sigma_c^0 = 5.0$ and $\sigma_\infty^{11}/\sigma_c^0 = 2.5$

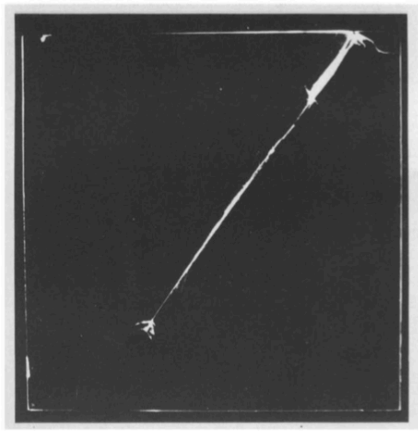

(b) Example of transition to shear-driven crack propagation under increased level of confinement - *e.g.* $\sigma_\infty^{11}/\sigma_c^0 \approx 2.5$ - reprinted from Broberg [44]

Figure 6.17: Crack patterns under critical level of confinement

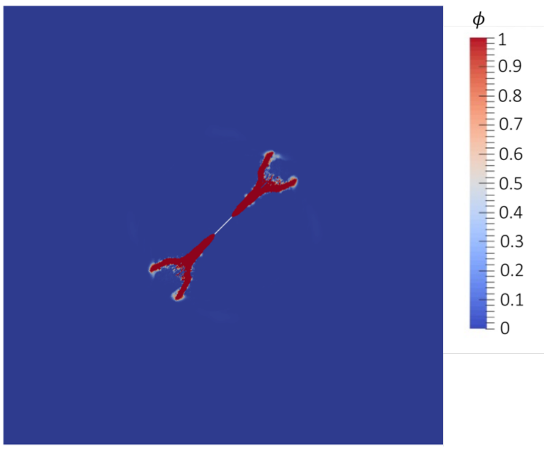

(a) Crack patterns for the case of $\sigma_\infty^{22}/\sigma_c^0 = 5.0$ and $\sigma_\infty^{11}/\sigma_c^0 = 5.0$

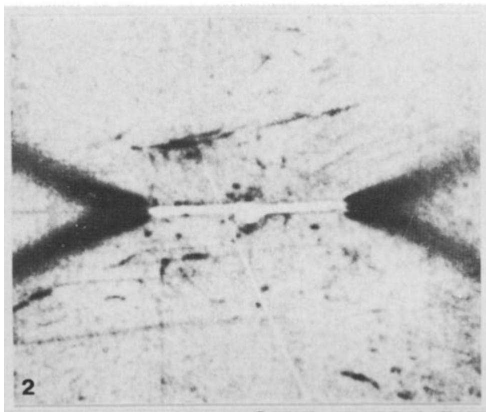

(b) Example of crack splitting under confinement above critical level for transition to shear driven crack propagation- *e.g.* $\sigma_\infty^{11}/\sigma_c^0 > 2.5$ - reprinted from Broberg [44]

Figure 6.18: Crack patterns under confinement above the level for transition to shear-driven crack propagation

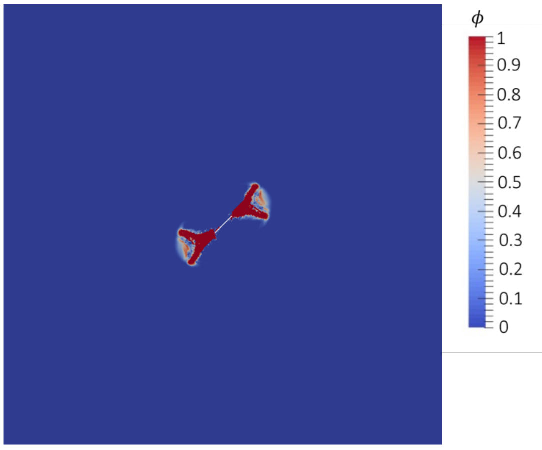

(a) Crack patterns for the case of $\beta = 9$

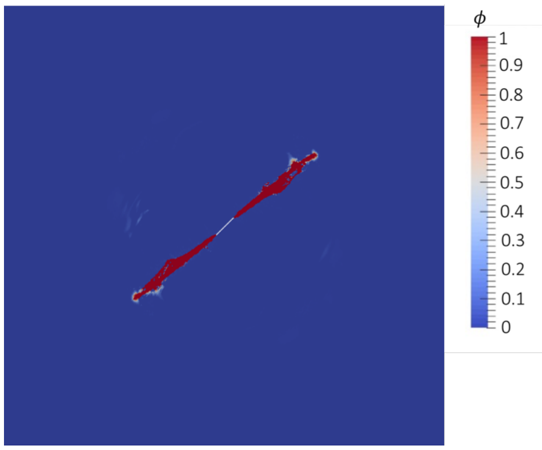

(b) Crack patterns for the case of $\beta = 16$

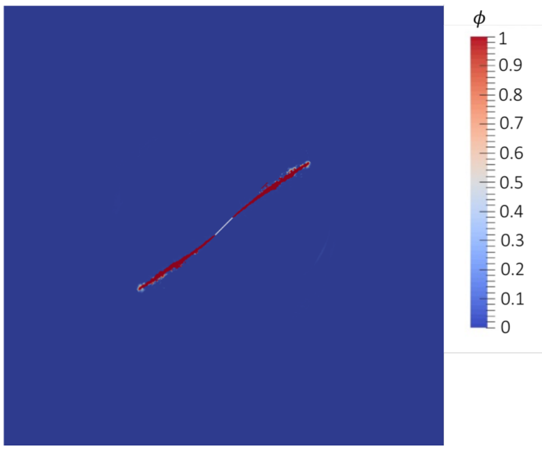

(c) Crack patterns for the case of $\beta = 25$

Figure 6.19: Crack patterns for different β

the theoretical line of maximum shear. As a material with higher mode-II fracture toughness is assumed, $\beta = 25$, a much cleaner and thin shear crack propagates along the same plane of the initial flaw, as it can be observed in Figure 6.19(c). The effect of the variation of the upper limit for mode of fracture transition, χ_u, again under the same loading conditions, is now examined and results reported in Figure 6.20. It

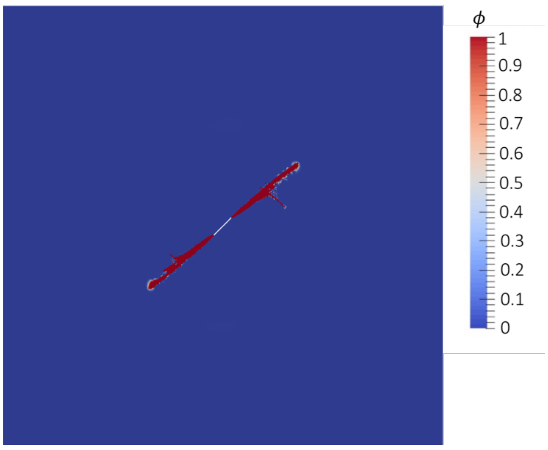

(a) Crack patterns for the case of $\chi_U = \chi_L$

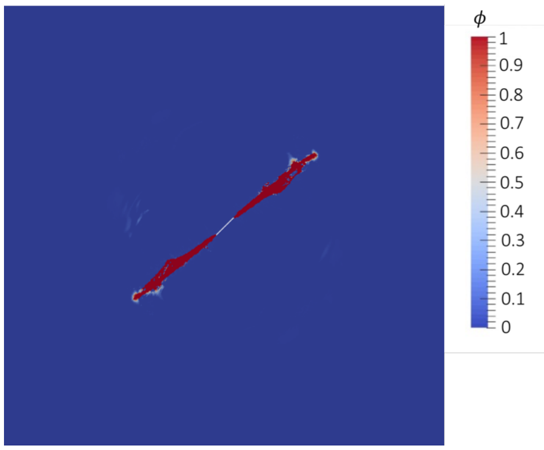

(b) Crack patterns for the case of $\chi_U = 0.6$

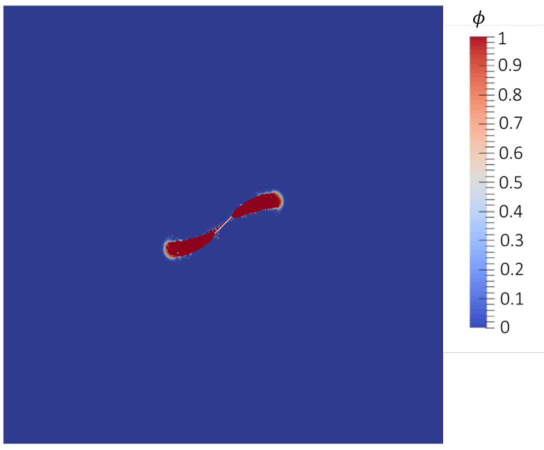

(c) Crack patterns for the case of $\chi_U = 1.4$

Figure 6.20: Crack patterns for different χ_U

can be seen that in the absence of a linear transition between the two modes of failure, which translates into assuming *i.e.* $\chi_U = \chi_L$, no change is observed in the crack pattern (Figure 6.20(a) as compared to the case in which $\chi_U = 0.6$ (Figure 6.20(b).

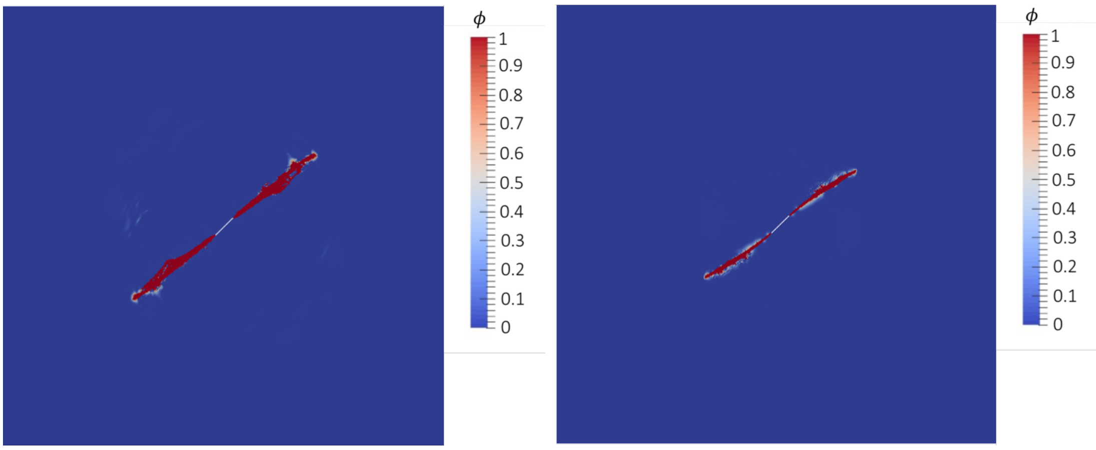

(a) Crack patterns for the case of $\eta_0 = 10^{-10}$ (b) Crack patterns for the case of $\eta_0 = 10^{-8}$

Figure 6.21: Crack patterns for different η_0

As the regime for linear transition in the mode of failure is extended, *i.e.* $\chi_U = 1.4$, the crack propagates as it would have a lower level of remote confinement, departing from having a net propagation path which lays along the plane of the initial crack.

So far, in this section, the sensitivity of the model has been explored only with respect to parameters which mainly refer to the definition of the mode-I-to-mode-II transition law. However, the model does also present rate-dependent features even for those material elements which are under compression. Although the length scale associated with micro-inertia is assumed to be constant, $l = l_\phi^0$, if a state of pure compression exists, the rate-dependency nature of the model is retained in view of a non-zero viscosity η_0 acting on the rate of growth of the phase field parameter. Therefore, results relating to the sensitivity of the crack propagation prediction on the variation of η_0 are presented in Figure 6.21. No-significant difference in the mode of failure is observed although bigger viscosity, *i.e.* $\eta_0 = 10^{-8}$, leads a phase field growth which tends to localize in a narrower zone along a plane seemingly parallel to the initial crack plane. This effect aligns with what has been observed in the case of increasing β (6.19). This suggests that increasing values for η provide a more pronounced resistance to phase field growth, in this case due to deviatoric deformation, needed to trigger shear crack growth.

Future work will focus on the investigation of an appropriate scaling law for l under pure compression. This scaling law might not be associated with any strength quantity but rather accumulated strain. It is envisaged that this will have to account for more complicated mechanisms such as micro-plasticity and shear band formation which goes beyond the scope of this work.

Chapter 7

SHPB optimization for ceramics characterization and phase field simulation

In this chapter the design and optimization of an experimental technique based on the SHPB used in conjunction with high-speed imaging are presented. This research activity has been identified as necessary to achieve a complete calibration and validation of the model presented in the previous chapter. The apparatus has been optimized in order to be able to characterize the extreme case of hard, highly-brittle materials such as ceramics. In the final part, the phase field model predictions for the idealized boundary value problem are compared against the experimental results and its limitation outlined as a basis for future development.

7.1 Introduction

This chapter is dedicated to the development of a split Hopkinson pressure bar (SHPB) technique which will serve as a means to validate and further calibrate the proposed model. In order to achieve this goal, the SHPB has to be designed in order to accommodate the challenges associated with the testing of ceramics. The extensive review provided in 2.4.1 has motivated the need to carry out a detailed assessment of how each feature of the apparatus configuration might affect the measurements. It is aimed to build the foundations for an integrated experimental-numerical platform able to predict the failure behaviour of hard brittle materials such as ceramics subjected to ballistic regimes of compression.

7.2 SHBP Virtual Prototyping

In this section, the effect of the variables involved in the design of the SHPB apparatus will be analysed by means of finite element simulations [234, 235, 236, 237, 238]. Computations have been carried out by means of the commercial suite ABAQUS Explicit.

7.2.1 Design of the ideal incident pulse

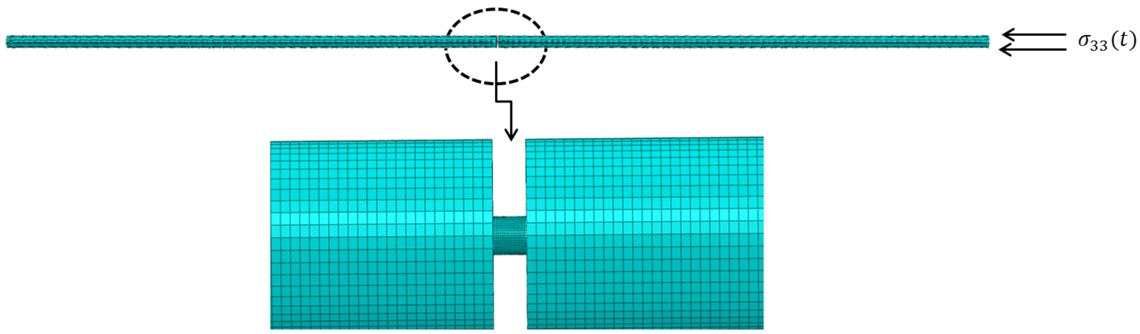

Figure 7.1: SHPB finite element model

The numerical model consists of two loading bars between which a cylindrical specimen is sandwiched. The schematic of the boundary value problem, along with the relevant geometric and material properties are presented in Figure 7.1 and Table 7.1 respectively. The ratio of the bars length over their diameter is 40 according to Davies' [68] analysis reported in Section 2.4.1. The spatial discretization has been chosen such that the longitudinal characteristic length of the element is comparable to the size of a typical strain gauge mounted on the bar. Moreover, the mesh transition is minimized in order to avoid numerical dispersion and any spurious wave reflections as the incident loading pulse travels along the bar.

The specimen design aims to take into account both the desire to achieve the highest strain rate possible and minimize inertia effects. The material is assumed to obey a simple linear elastic constitutive response in which relevant material properties, *i.e.* Young's modulus and Poisson's ratio can be adopted from the literature. The amplitude, σ_B, corresponds to the stress in the bar when the specimen, assumed under equilibrium conditions, has reached its nominal final strength, σ_S. If classical force equilibrium arguments are used, the stress in the bar is calculated through:

$$\sigma_B = \frac{\sigma_s A_S}{A_B} \tag{7.1}$$

The duration of the entire pulse, which comprises a loading and an unloading linear path corresponds to the time needed for the stress wave to complete two entire transits along the striker after the impact with the input bar.

$$t_{tot} = \frac{2l_{str}}{c_{str}} \tag{7.2}$$

In this work, the length of the striker is chosen to be half of that of the bars in order to avoid any overlap between incident and reflected waves in the bar. Also, it should be remarked that since ceramics are mostly brittle, there is no need to have a long duration of the loading pulse as otherwise it would be required for the case of metals with an elastic-plastic response.

The slope of the loading path, which dictates the rising time needed to reach

	Bar	Specimen
E [GPa]	114	400
ν	0.33	0.22
L [mm]	800	3.5
D [mm]	20	4

Table 7.1: Rate-dependent parameters chosen for the simulations

the peak load, can be estimated by using the expression suggested by Frew et. al. [239, 240]. It has to be noted that this expression assumes that the specimen is in equilibrium and that the incident pulse, increases linearly with respect to time:

$$\sigma_t = Mt_r \tag{7.3}$$

$$M = \dot{\varepsilon} E_S \frac{A_S}{A_B}\Big[1 - exp\Big(-\frac{2t_r c_s}{Zl_s}\Big)\Big] \tag{7.4}$$

Based on the discussion carried out in Section 2.4.1, the strain rate, as given by equation 2.19, can be chosen as initial reference value and the corresponding slope is indicated with M_0. The ideal trapezoidal incident pulse, shown in Figure 7.2, is used as the time history for the pressure boundary condition applied on the end of the input bar with $\sigma_B = 0.12$ GPa. Simulations have been performed in order to investigate the effect of the variation of M on the measured strain rate.

The plot presented in Figure 7.3 shows the strain rate history as measured at the middle of the bar by means of equation 2.11b. The strain rate is normalized by its ideal value as calculated by means of equation 7.4 for the corresponding M; the time is normalized by the time required to establish dynamic equilibrium according to equation 2.13. It can be noticed that as M increases, the equilibrium, which ideally corresponds to a normalized strain rate value of 1, is not reached, *e.g* for M=5. Moreover for those cases which satisfy the requirement for equilibrium, the normalized

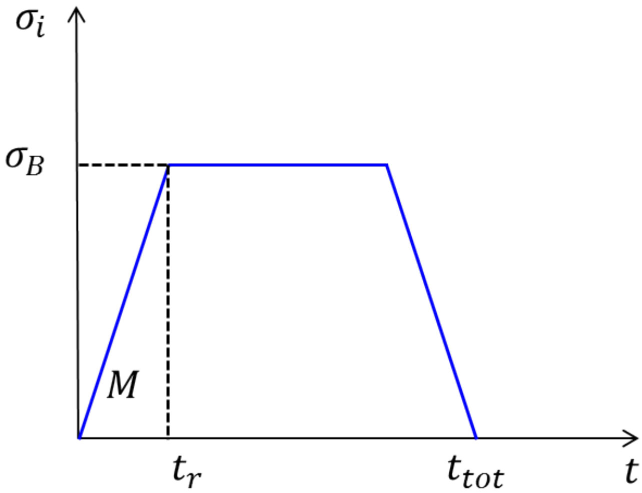

Figure 7.2: Ideal trapezoidal incident pulse

time exceeds unitary value meaning that several reverberations occurred within the specimen prior reaching the peak load. Furthermore, for M smaller than 2, the results

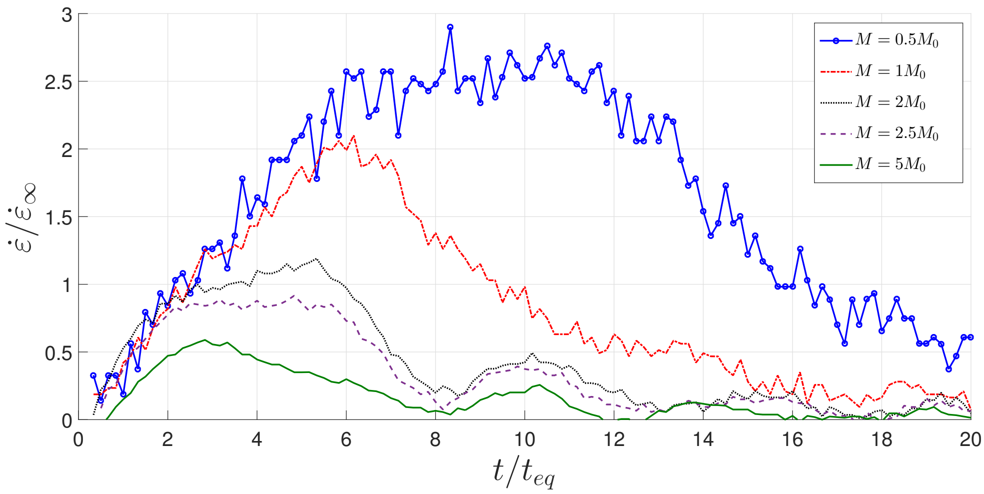

Figure 7.3: Normalized strain rate for a range of incident pulses with different slope

do not show a constant strain rate plateau after have reached the equilibrium. This is due to the normalization chosen in this work; the expression derived by Frew et. al. (7.4), given an incident pulse, provides an estimate for a steady state strain rate at equilibrium without accounting for further variations. Furthermore, it can be seen that the presence of oscillations around the constant value becomes more prominent as the rise time increases. Based on these results, it is concluded that for the specific material chosen in this study, the slope of the loading path should assume a value close to $2M_0$. However, the approach described above can be easily adopted for any elastic-brittle material by simply using its relevant mechanical properties and specimen dimensions.

7.2.2 Effect of pulse shaper geometry

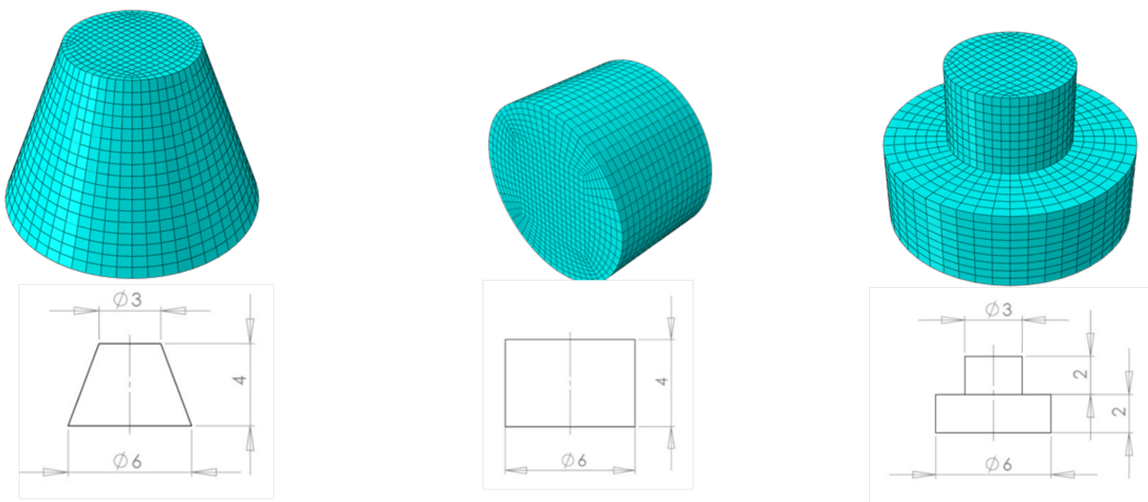

Figure 7.4: Proposed pulse shaper geometries

In the following, finite element simulations are carried out to investigate how the incident pulse can be shaped to meet the requirements described in the previous sections, namely stress equilibrium and wave dispersion minimization. Specifically, it is aimed to qualitatively investigate the effect of the pulse shaper geometry configuration on the incident stress wave. The material considered is annealed copper as suggested by Subhash and Ravichandran [241]. The model consists of two bars of the same material and diameter, *i.e.* the striker and the input bar, with a pulse shaper placed in between. The boundary conditions consist in nodal velocity applied on the striker corresponding to the value of stress assumed in the previous section which by means of Equation 2.14 results in $v_{str} = 10[mm/ms]$. The same considerations, made in the previous section, regarding the length of the striker apply here; a schematic of the different pulse shaper geometries in Figure 7.4. The contact between the pulse shaper and the bars is idealized as frictionless which can be achieved in reality through an accurate use of lubricants. The constitutive response adopted for the copper is that one proposed by Johnson and Cook [242] for the strain rate dependent behaviour of hardening ductile metals and with relevant parameters taken from the literature [243]. The stress and the time have been normalized with respect to the stress in the bar as calculated though equation 2.14 for a given striking velocity and the rise time estimated as optimal in the previous section, respectively. Moreover simple discs of different thicknesses have been investigated.

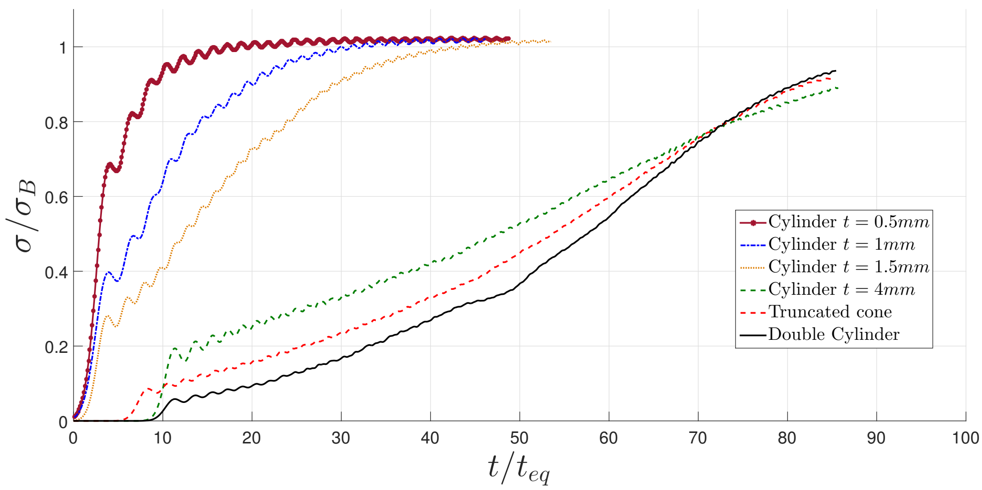

Figure 7.5: Normalized stress-time history for different pulse shapers

Results in Figure 7.5 show that the amplitude of the stress wave, generated after the impact, increases fairly linearly with respect to time. A reduction in the thickness results in a steeper pulse while choosing a varying cross section, *i.e.* truncated cones or double cylinders, leads to a significant increase in the rise time as well as a lower stress value. It has to be remarked that the results rely on the choice of the constitutive model for the copper as well as on the resolution of the spatial discretization. However, they are not intended to provide a quantitative measure of the pulse shaper parameters but rather to serve as general comparative guideline.

7.2.3 Effect of anvils configuration

Different types of anvils and installation strategies are proposed in Figure 7.6 and their effects on the strain rate discussed next. It is common belief that as long

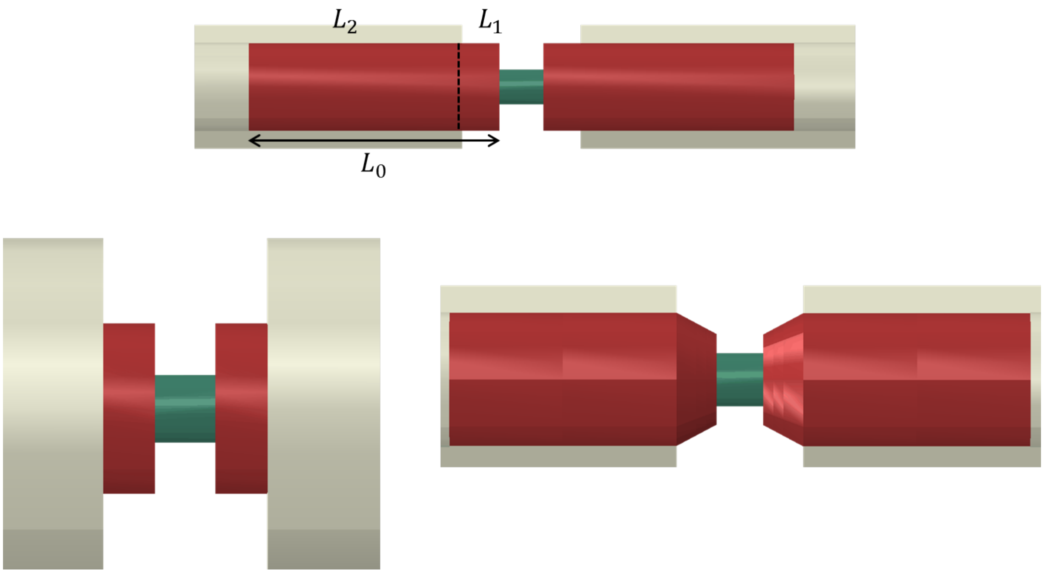

Figure 7.6: Proposed anvils configurations

as the diameter of the anvil meets the requirement of impedance matching on the anvil/input bar interface, the effect of its longitudinal extension could be considered almost negligible. This issue is somehow related to the difficulties of installing the anvils in a way which would guarantee their correct placement during the duration of the experiment. Other concerns refer to the possibility of reducing the stress concentration on the specimens by using a truncated-cone configuration as discussed in section 2.4.1. Moreover, inserting the anvil directly into the bar could cause lateral indentation during the application of the loading; the re-use of the anvil with damaged or rough lateral surface might be responsible for friction effect resulting in oscillations of the signal. Finite element simulations of the different configurations have been

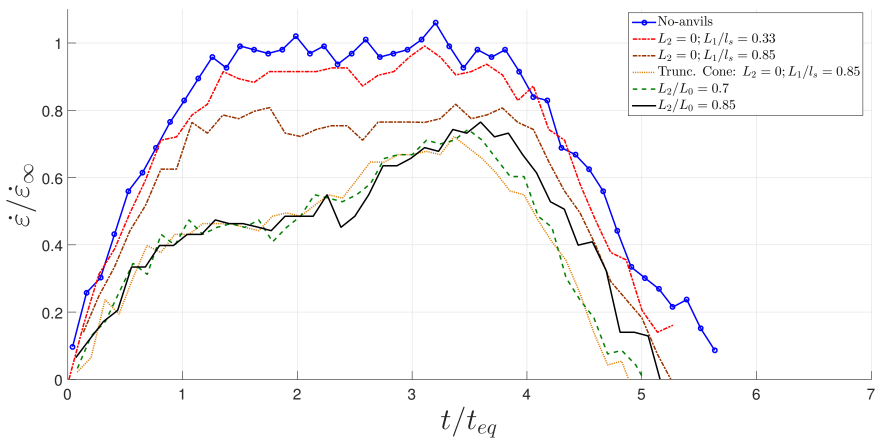

Figure 7.7: Normalized strain-rate history for different anvils configurations

carried out; the ideal pulse extrapolated in section 7.2.1 has been used as a pressure boundary and results are reported in Figure 7.7. The strain rate has been normalized with respect to that one corresponding to the ideal case in which anvils are not employed while the time normalization follows closely that one of Figure 7.3. It can be seen that as the length of insertion of the anvil inside the bar increases, a significant decrease in the strain rate is registered. This reveals that, although the anvils are impedance matched, their presence affects the percentage of the wave which reflects into the input bar. Part of the momentum contributes to deform *elastically* the anvil and this contribution increases as the volume of the anvil increases. Therefore, a design which avoids the placement of the anvil as a bar insertion and reduce its longitudinal length as much as possible, has to be pursued.

7.2.4 Effect of specimen design

The following discussion concerns the investigation of the effect of specimen geometry on the measured compressive final strength. The material constitutive response is now described by means of the JH2 [89] model which has been extensively employed throughout the years to predict the failure of ceramic materials at the continuum scale. It has to be remarked that at this point, it is not the aim of the authors to provide a quantitative prediction of the material behaviour. Three different cases, schematically presented in Figure 7.8 are considered: cylinders and cubes designed according to the requirements discussed in section 2.4.1 and a dumb-bell-shaped sample as proposed by Tracy [84].

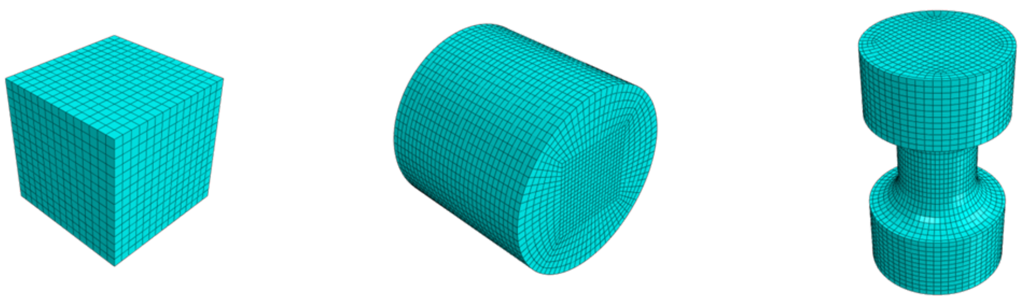

Figure 7.8: Proposed specimen configurations

The results presented in Figure 7.9 report the ratio between the maximum compressive stress as measured on the output bar by means of equation 2.11a and the average value of the stress along the loading direction in the gauge length of the specimen prior to damage initiation. An unitary ratio represents the optimum case in which the bar measurement, as a consequence of specimen equilibrium and absence of wave dispersion, accurately describes the material stress state. It can be seen that the two quantities are quite different for the case of cubes with a discrepancy of around 35%. The dogbone and the disc present similar features with a less pronounced mismatch, accounting to almost 15%. These results reveal that cubic samples suffer of premature failure because of stress concentration at the corners. Moreover, the ma-

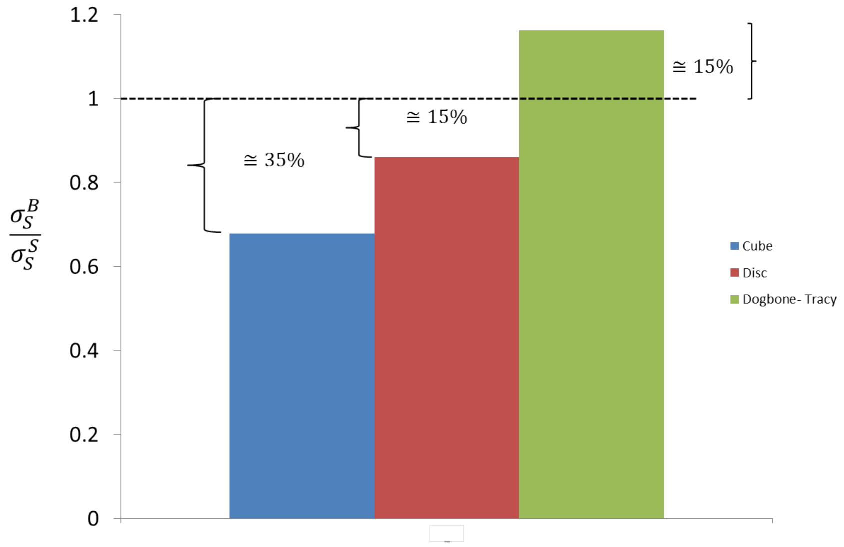

Figure 7.9: Normalized peak stress for different specimens

terial state is affected by lateral material acceleration which leads to a multi-axial state of stress favourable for early tensile-induced fracture. However, the cylindrical and dogbone-shaped specimens guarantee a more uniform stress distribution of stress which is an essential requirement for stress equilibrium. The dogbone provides an overestimate because, although the material fails in the cross section, the end cups act as an additional temporary confinement which inhibits a sudden drop in the stress.

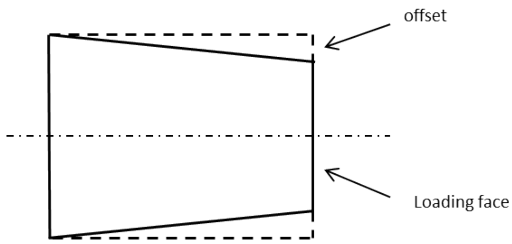

(a) Specimen with end-faces perfectly perpendicular to loading direction

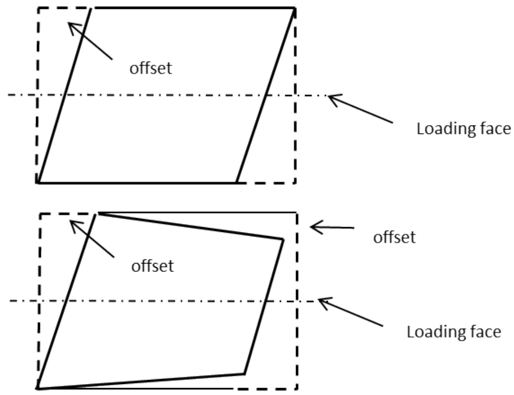

(b) Specimen with end-faces not perpendicular to loading direction

Figure 7.10: Schematic representation of possible geometrical imperfections in a cylindrical specimen

.

7.2.5 Specimen geometry imperfections

In this section the effect of specimen geometrical imperfections is investigated. It is aimed to estimate the manufacturing tolerances that should be pursued such that the measured strength is not affected by the specimen pre-existing configurational defects such as lack of orthogonality, faces parallelism or misalignment with respect to the loading direction. Specimens with different types of manufacturing imperfections are proposed in Figure 7.10. Results are presented as the averaged stress to failure measured in the specimen, σ_S for each of the proposed cases, normalized with respect to the one obtained for an ideal configuration with no defects, σ_S^0. Results pertaining to a configuration in which the loading faces are parallel to each other and to the loading bars end faces are presented in Figure 7.11. The sensitivity study considers different values of the *offset* of the face on which the load is applied (loading face) with respect to the ideal configuration. It can be seen that as the offset increases, *i.e* the ratio between the loading face and the other end face of the specimen decreases,

Figure 7.11: Results pertaining to configuration in Figure 7.10(a)

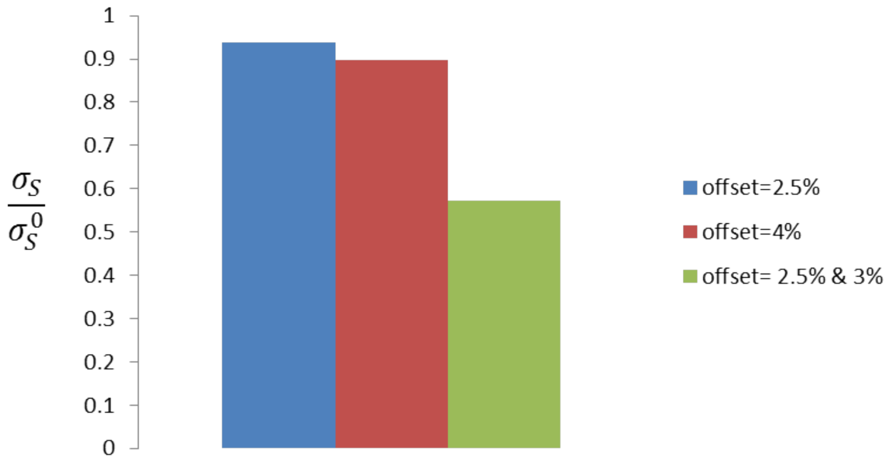

Figure 7.12: Results pertaining to configuration in Figure 7.10(b)

the measured stress to failure obtained in the specimen decreases. Similarly, the case proposed in Figure 7.12 (top) shows decreasing values of the normalized stress to failure as the offset along the loading direction increases. A combination of the two offsets - bottom schematic in Figure 7.10(b) (down), drastically reduces the value of the normalized stress-to-failure. It can be inferred that the manufacturing tolerances, $i.e$ 30 - 50 μm for a 3 mm diameter cylindrical specimen, proposed over the course of the project, should be ensured. Moreover it should be considered that such "defected"

Figure 7.13: Effect of interface frictional conditions

configurations favour premature failure due to stress localization at corners and or asperities located at the anvil/specimen interfaces therefore promoting a non-uniform three-dimensional stress distribution prior to failure.

7.2.6 Effect of specimen-anvils interface friction conditions

The effect of the frictional conditions at the specimen-anvils interface is examined next. The frictional effects due to size mismatch between the anvils and the specimen can be minimized by controlling the ratio between the diameter and length of specimen such that the following constraints are met [77] (equation 2.25) However, further frictional effects can be related to the state of surface finishing of the specimen (and anvils) as well as to the distribution of lubricants generally used to place the specimen between the anvils. The results are presented in the same form as before in Figure 7.13. It can be seen that a rough interface, *i.e* infinite friction, results in overestimating the compressive strength of the material as it leads to a prolonged contact between the specimen and anvils even if the material has started failing far

Figure 7.14: Effect of loading rate on stress measurements

from the interface along with a mode of fracture similar to local buckling. As the friction decreases the measurements seem to underestimate the average stress to failure since the material starts failing at the interface due to high Poisson's effect, *i.e.* the specimen is ideally free to slide over the anvil, therefore loosing contact with the anvil and causing a drop in the recorded signal.

7.2.7 Effect of loading rate

The effect of loading rate on the measurements is discussed in the following. The ideally remote applied strain rate, which depends upon the striking velocity as well as on the rise time of the applied pulse, is indicated with $\dot{\varepsilon}_\infty$. The results are presented as the ratio of the stress calculated by means of equation 2.11a, σ_B, over the averaged stress in the specimen, σ_S, both taken at a simulation time close to the one in which failure occurs. Results reported in Figure 7.14 show that as the loading rate increases an increase in the measurements dispersion is observed. Moreover a refinement of the spatial discretization, expressed as the ratio between the element size on the bar, l_e, and the length of the strain gauge used in the experiment, l_{SG}, does not significantly

Figure 7.15: SHPB apparatus at IEL

improve the reliability of the data. It is, therefore, suggested that at higher rates wave dispersion might result in underestimating the compressive strength of the material.

7.3 Improved SHPB experimental characterization

This section discusses the SHPB experiments carried out on Alumina samples (provided by Morgan Advance Ceramics). The SHPB apparatus configuration has been designed according to the modifications/improvements motivated by the results of the sensitivity analysis performed by means of the numerical simulations.

7.3.1 SHPB configuration

The apparatus employed at the Impact Engineering Laboratory (IEL) is shown in Figure 7.15. The configuration consists of striker, input and output bars all in titanium and with length of 2700 mm and 20 mm in diameter. A set of three 2mm in length strain gauges is installed as in previously shown in Figure 2.3. The data

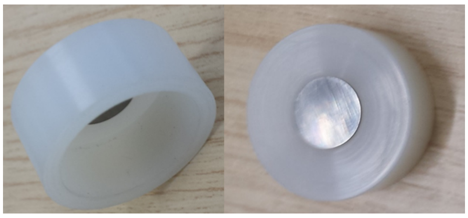

Figure 7.16: Anvils: tungsten cores inserted into nylon cups

analysis relies on an algorithm able to decouple the three waves, incident, reflected and transmitted such that the equations 2.11a–2.11c can be used to characterize the specimen mechanical response. A set of anvils is employed in order to avoid bar indentation which would lead to misleading results. The anvils consist of tungsten disks designed according to impedance matching requirements, inserted into a nylon cup which facilitates installation and alignment 7.16. Experiments have been performed on 99.5 % alumina samples provided by Morgan, although certainty about the compliance with the requested tolerances for surface roughness, close to $0.3Ra$, and parallelism-orthogonality, within $0.003mm$, could not be ensured. The specimens have a characteristic cross section of $3.5mm$. The specimens design relies both on the requirement to minimize friction effects as well the minimize both axial and radial inertia effects for the case of cylinders. The experiments have been conducted at a striking velocity of $\approx$ 10 m/s while the strain rate has been varied by changing the specimen length and/or the pulse shaper.

7.3.2 Results

Figure 7.17 shows a typical plot of the equilibrium and strain rate attained over the course of the loading of the specimen. It is assumed that equilibrium is established if the difference between the input force and the output force, measured from the signal recorded on the SG2 and SG3 stations respectively, falls within the range of 10 % difference. Given this condition, along with a regime of fairly constant, not excessively oscillating, strain rate prior to the peak-load, Equations 2.11a and 2.11c can be employed to calculate the stress/strain-to failure. Moreover it has been proposed to employ digital image correlation (DIC) analysis to overcome some of the drawbacks associated with the use of strain gauge measurements. As previously discussed, high loading rates, resulting in increasing wave dispersion, and variable friction conditions at the anvils/specimen interface affect the reflected and transmitted wave signals on the bar, leading to a wrong quantification of the failure properties of the testing material. It is possible to carry out DIC analysis by using the images acquired from the high-speed camera (Kirana) with sampling capabilities up to 10^6 frames/s. Each specimen has been previously speckled such that a *computational grid* can be generated during the images post-processing in the software ARAMIS. The displacement between two points of the grid can be mapped at each recorded stage and strain, strain rate and stress calculated. Figure 7.18 shows an example of such an analysis. It is observed that the material exhibits a linear elastic response up to failure which occurs at a realistic limit, for this material, of $\approx 1.15\%$. It is assumed that the Young's modulus is rate-independent allowing to calculate the stress-to-failure as:

$$\sigma_f = E_s \varepsilon_f \tag{7.5}$$

Moreover, the DIC can be employed to assess the equilibrium condition in the material, here interpreted as the degree of strain homogeneity on the specimen surface. Denser collocation of points on the grid would also provide an insight on the process of strain localization prior failure. Results relating to experiments at different

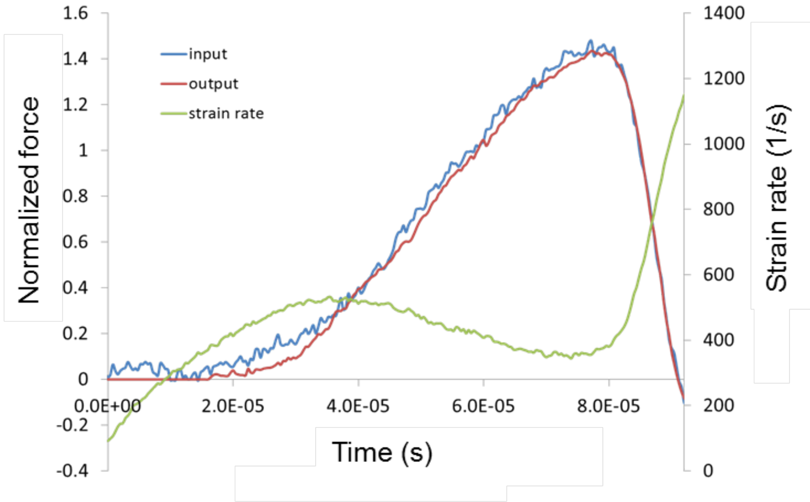

Figure 7.17: Equilibrium and strain rate

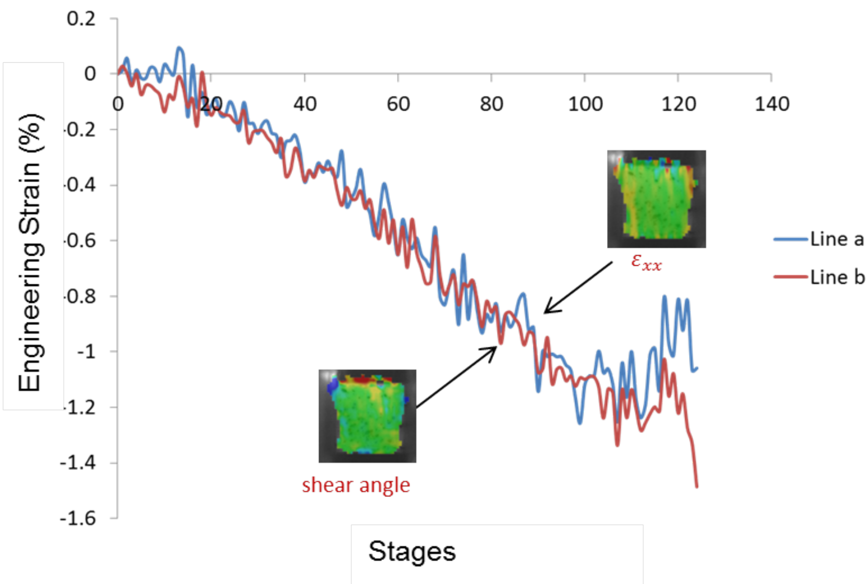

Figure 7.18: Recorded stages versus engineering strain

strain rates are presented in Figure 7.19 where measurements from the strain gauges have been compared against those obtained by means of DIC. It has been possible to carry out the DIC correction only on those experiments whose recorded images ensured enough resolution. It can be seen that strain gauges measurements suffer of wave dispersion effects at higher rates as well as, most presumably, distortion due to premature failure associated with low manufacturing on the contact faces. Correcting these results by means of DIC enables to register the expected rate-dependent strength behaviour as originally observed by Lankford [244, 245] who presumably relied on installing the strain gauge directly on the specimen. The strain rate-dependent strength results follow closely the law proposed by Kimberley et. al. [246] in which the time and length scales associated with micro-distributed defects and their interaction were taken into account leading to the following scaling:

$$\sigma_c = \sigma^0_{c,e,comp}\left(1 + \left(\frac{\dot{\varepsilon}}{\dot{\varepsilon}_{0,c}}\right)^{\frac{2}{3}}\right) \tag{7.6}$$

where the quasi static compressive strength, $\sigma^0_{c,e,comp} = 3.050$ GPa and the interacting transition rate $\dot{\varepsilon}_{0,c} = 9000s^{-1}$ have been taken from the work of Staehler et. al. [247].

In conclusion, it is suggested that this technique, if used in conjunction with an optimized SHPB configuration, could provide the ability to characterize the mechanical response of ceramics under dynamic compressive load.

7.4 SHPB experiment simulation

In the next section the model developed in this work is employed to simulate the dynamic failure behaviour of the alumina-based material used in the previous section as a baseline to optimize the SHPB apparatus.

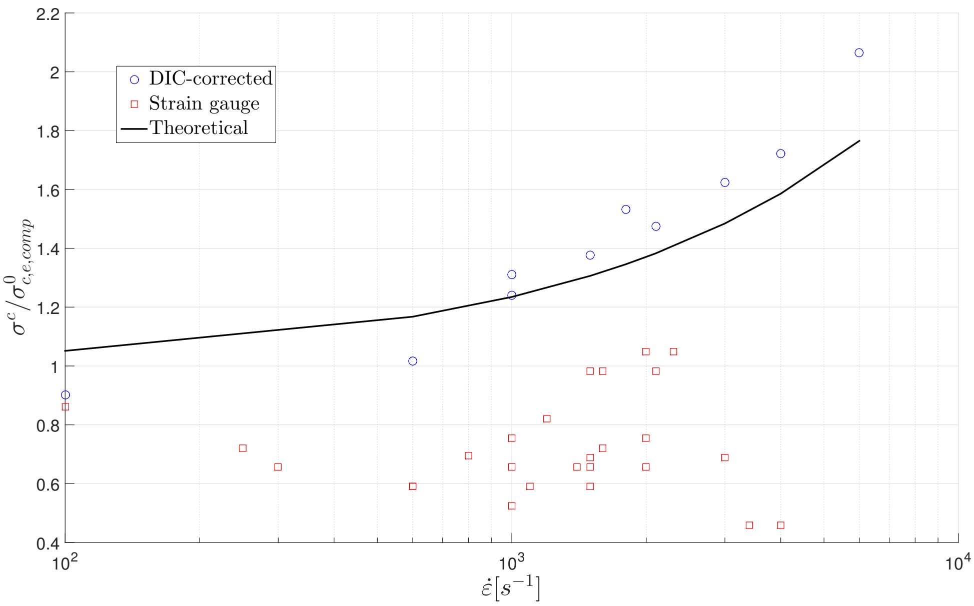

Figure 7.19: Strain rate-dependent compressive strength

7.4.1 Boundary value problem idealization

A schematic representation of the boundary value problem is provided in Figure 7.20. Although in the experiments cylindrical specimens were employed, it can be assumed that under the condition of minimal radial inertia effects, *i.e.* the relation in equation 2.21 is satisfied, the problem can be reduced to only considering the middle cross section of the sample. Therefore, plane strain conditions are assumed. This choice enables to reduce the computational costs associated with the need for a fine discretization dictated by the chosen value for l_0. Under these assumptions, the model consists of a squared plate with dimension of $L = 0.5[mm]$. The sample is thought to have an ideal population of micro-cracks as it would be in the case of most of ceramics containing pre-existing distributed flaws. Two ideal configurations are considered as reported in Figure 7.20. An ideal case of equally distributed micro-cracks, with an angle of $\pm 45^0$ with respect to the longitudinal cross section is considered in Figure 7.20(a). Concurrently, a case of randomly distributed micro-cracks with inclination 0^0, $\pm 45^0$ and 90^0 is presented in Figure 7.20(b). These sets of heterogeneities have been created by removing elements from an original hexa-based structured mesh. It has to be pointed out that this is an approximation of a real micro-cracks configuration as the resulting crack surfaces geometries are not flat and characterized by sharp features. However, within the limited pre-processing capabilities here at disposal, this idealization allows to study the effect of a random defects configuration on the rate-dependent failure behaviour of the material. The material properties are listed in table 7.2. It has to be noted that the critical energy release rate, G_c has been scaled according to the choice of the regularization zone l_0. The latter has been chosen such that the smallest characteristic length scale of the problem, here identified as the averaged spacing between the micro-cracks, is properly resolved. By further assuming that the critical stress at softening corresponds to the tensile strength of the material [248], *i.e.* $1.81\sigma_c^0 \approx \sigma_{c,e}^0$. By employing equation 4.41a the correspondent G_c can be calculated. Moreover the parameter $\gamma_2 = 5$ has been assumed, in contrast to the cases discussed in the previous chapter. It has been observed that as the ratio $\sigma_{c,e}^0/\sigma_c^0 \to 1.81$ also γ_2 decreases nonlinearly. In this limiting case, the scaling law for l might reduce to only defining the parameters γ_1, γ_3, γ_4, γ_5, γ_6, which are associated with the assumed transition strain rate $\dot{\varepsilon}$. The load corresponds to a ramped prescribed velocity on the top boundary whilst the lower boundary is fixed along the loading direction. The rise time is chosen according to equation 2.13 such that dynamic equilibrium conditions and an averaged homogeneous strain rate in the specimen are established. The mesh is designed such that $l_0/h = 4$ where h is the

Material Parameter	Value
E	370 [GPa]
ν	0.2
ρ	$3.88 \cdot 10^{-6}$ [$\mathrm{Kg} \cdot \mathrm{mm}^{-3}$]
G_c	$3 \cdot 10^{-6}$ [$\mathrm{J} \cdot \mathrm{mm}^{-2}$]
l_0	$5 \cdot 10^{-3}$ [mm]
$\sigma^0_{c,e}$	$2.5 \cdot 10^{-1}$ [GPa]
n_2	0.33
$\dot{\varepsilon}_0$	1000 [s^{-1}]
s	0.01
γ_1	0.55
γ_2	5
γ_3	4.25
γ_4	0.35
γ_5	1.3
γ_6	0.45
χ_L	0.3
χ_U	0.6

Table 7.2: Material parameters used in the SHPB simulations of a ceramic specimen

characteristic element size.

7.4.2 Results

Results pertaining the measured compressive rate-dependent strength are reported in Figure 7.21. This quantity is calculated as the maximum reaction force over area ratio attained during the simulations and measured at the lower, fixed boundary. This approach resembles closely the measurement strategy employed in classical SHPB experiments without the correcting procedure based on the DIC presented in the previous section. It is envisaged that this is the closest estimate obtainable as the specimen is defect-free at the boundaries with an imposed level of perfect parallelism/orthogonality along with experiencing minor wave dispersion effects. A series of simulations under different loading rates and values for β have been carried

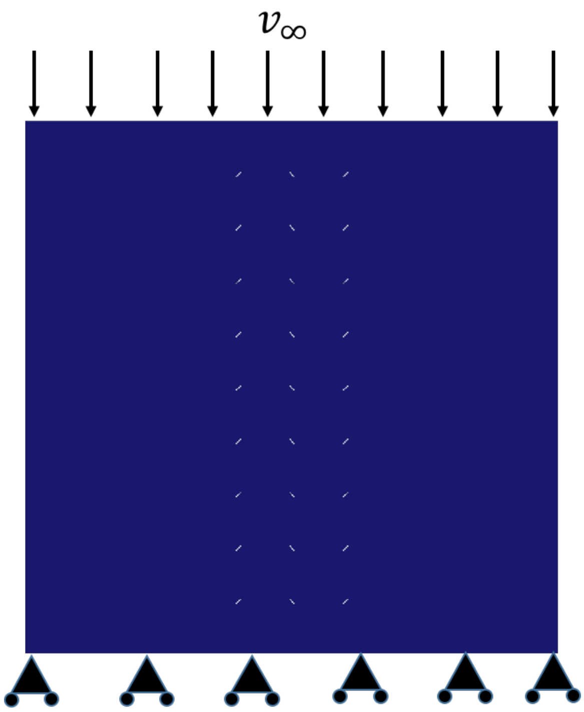

(a) Ideal ceramic sample with array of pre-existing micro-cracks

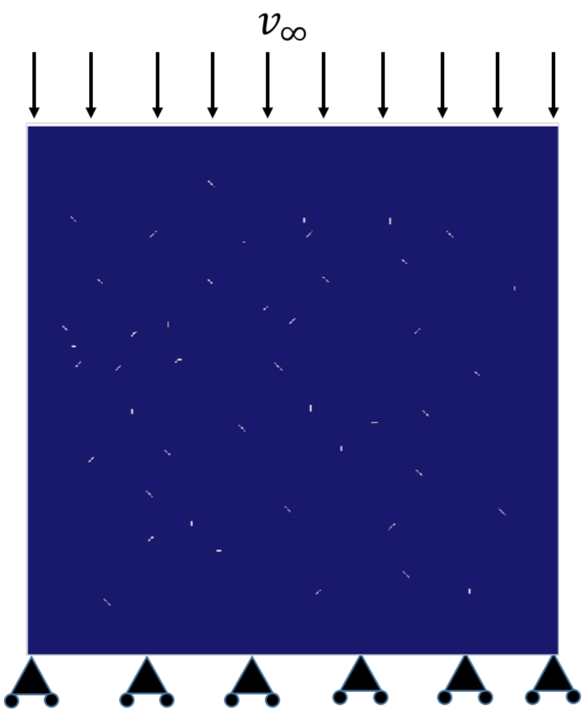

(b) Ideal ceramic sample with randomly distributed pre-existing micro-cracks

Figure 7.20: Ideal SHPB boundary value problem for ceramic samples

out. Results are compared against the baseline scaling law proposed by Kimberly et. al. [246] as recalled in the previous section. The smallest value for $\beta = 4$ has been chosen based on the results of Singh and Shetty [249] on polycrystalline alumina ceramics who reported values of $K_{II_c}/K_{I_c} = 2$ under quasi-static conditions. However, since the critical energy release rate has been scaled in order to meet the condition on l_0 given the constraint on the tensile strength, the value of β - presumably higher than 4 - has to be calibrated accordingly. It can be seen in Figure 7.21 that for increasing values of β the compressive strength increases. This also leads to a more pronounced rate-dependent response. However, the response does not match the baseline for any unique value of β. This result suggests that β itself should be considered to be a rate-dependent quantity in accordance with the notion that the dynamic critical energy release is dependent upon the crack velocity and therefore on the rate [250]. Moreover, it is observed that a different rate-dependent strength behaviour is observed between the two defects configuration considered here. A random distribution of pre-existing defects leads to a more distinct rise in the strength as the rate increases, while for the case of an equally distributed array the change with the rate, although registered, is somewhat less pronounced across all the variation of β [109]. This observation suggests that the microstructure features of the material have to be accounted. Therefore, a more effective numerical calibration has to be performed on a series of statistically representative volume elements (RVEs). Nevertheless a rate-dependent distribution of the crack patterns can be observed for both the configuration as presented in Figures 7.22 and 7.23. These results correspond to values for β that closely follow the baseline at a given rate. As a general trend, it can be observed that lower rates promote the activation of a smaller num-

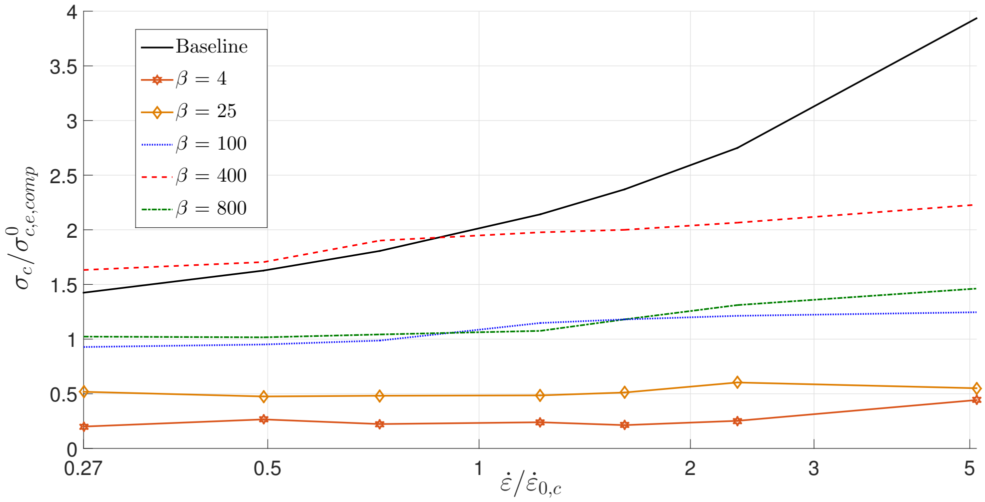

(a) Ideal ceramic sample with array of pre-existing micro-cracks

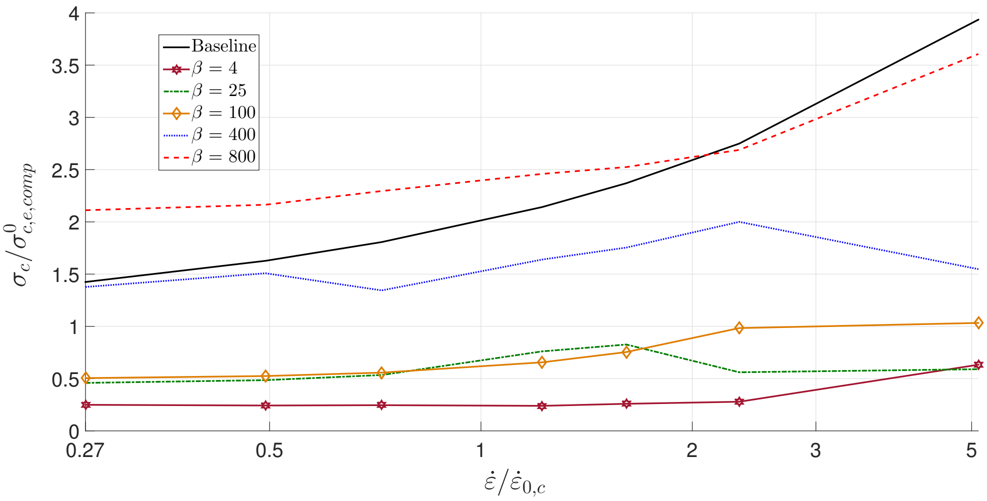

(b) Ideal ceramic sample with randomly distributed pre-existing micro-cracks

Figure 7.21: Compressive strain rate-dependent strength behaviour for different β

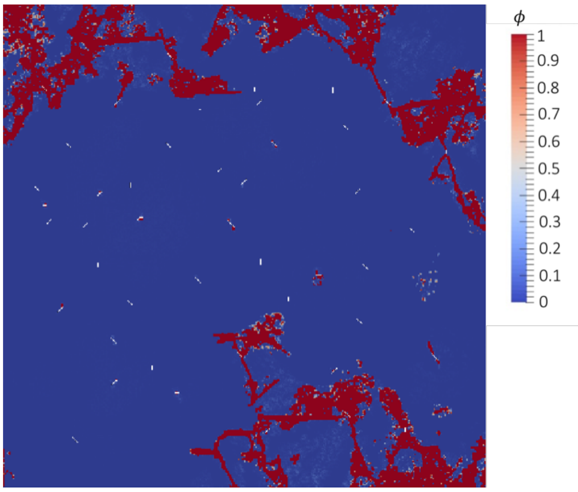

(a) Crack patterns for $\beta = 400$ and $\dot{\varepsilon} = 0.5$

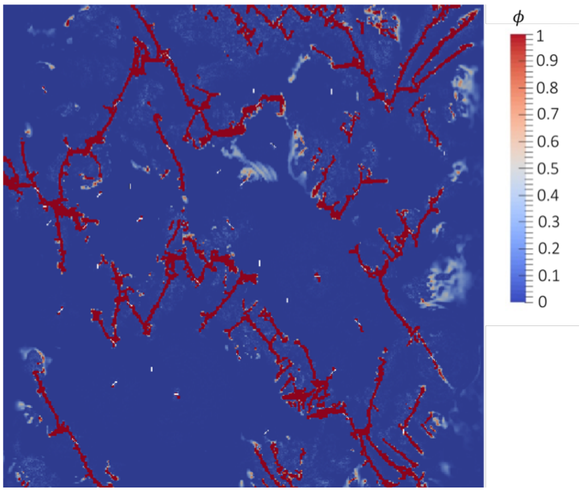

(b) Crack patterns for $\beta = 800$ and $\dot{\varepsilon} = 5.1$

Figure 7.22: Crack patterns for the case of randomly distributed pre-existing micro-cracks

ber of micro-cracks which tend to propagate in a region closer to the boundaries as shown in Figures 7.23(a) and 7.22(a). Upon the increase of the loading rate more micro-cracks are activated and the crack propagation patterns are spread out in the material more extensively (Figures 7.23(b) and 7.22(b)). Results for lower values of β at a strain rate $\dot{\bar{\varepsilon}} = 0.9$ for the two configurations are presented in Figure 7.24. It can be seen that a specimen which contains equal, regularly-spaced micro-cracks fails by the coalescence of a series of wing cracks which emanates from the pre-existing crack

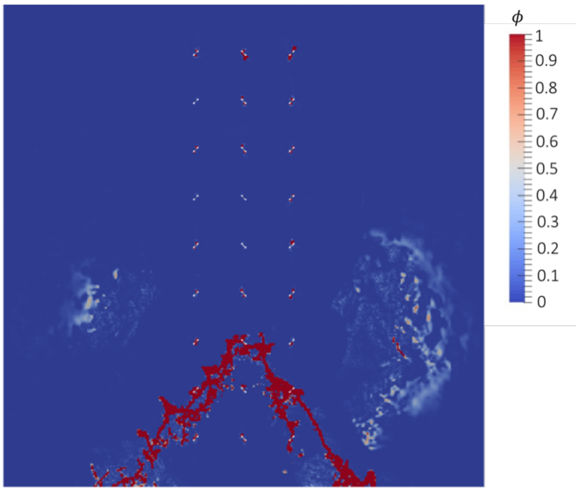

(a) Crack patterns for $\beta = 800$ and $\dot{\varepsilon} = 0.27$

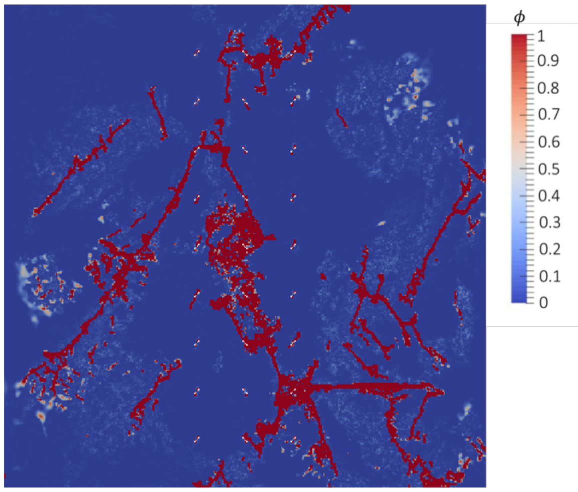

(b) Crack patterns for $\beta = 800$ and $\dot{\varepsilon} = 0.9$

Figure 7.23: Crack patterns for the case of an array of distributed pre-existing micro-cracks

tips. Conversely, a random distribution does not result in the activation of several micro-cracks and failure occurs due to the propagation of rather macroscopic diffusive secondary cracks inside the medium. As discussed in Chapter 6, β is the main parameter responsible for the mode of failure transition and for the scaling of the crack resistance force under states of pure-deviatoric deformation. Although a local state of tension is established ahead of the tips of the micro-cracks, which therefore drives the evolution of the length scale associated with micro-inertia effects, the absence of a

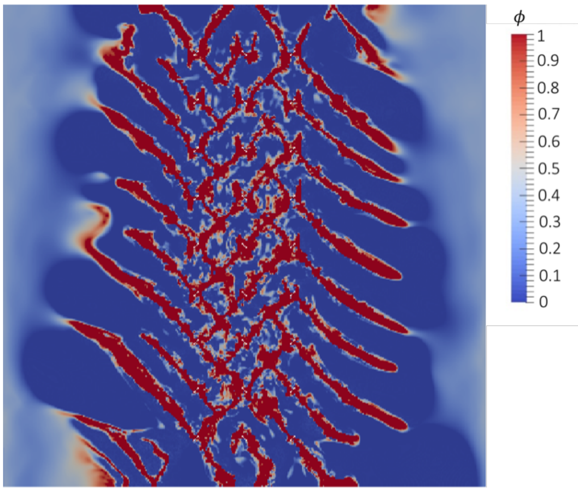

(a) Array of micro-cracks

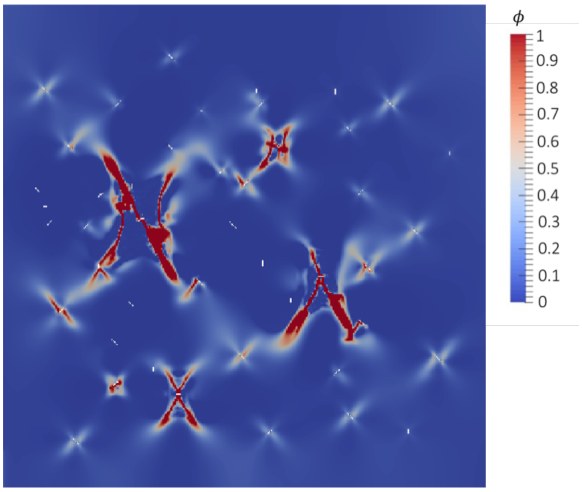

(b) Randomly distributed micro-cracks

Figure 7.24: Crack patterns for $\beta = 25$ and $\dot{\varepsilon} = 0.9$

contact detection feature between the micro-crack surfaces does not allow to sustain this mechanical state. Therefore, β becomes the only parameter able to provide a rate-dependent effect, in view of the absence of evolution of both l_0 and η. Moreover, for a more accurate description of the crack surfaces contact conditions, a different split for the stress components upon which the damage function would act selectively, might be required [251]. The current model does not take into account the potential generation of plastic deformation which have been shown to play an important role in the failure mechanism evolution at the micro-crack level. The investigation of these issues and consequent development of new features in the model will be objective of future work. However, the experimental procedure developed here has shown promising contribution in the validation of the current model and will serve as a means of calibration for the future. It has to be pointed out that these effects have not arisen, at early stages as in here, in the benchmarks presented in chapter 6. In that context the pre-existing crack was isolated and with a bigger notch size which allows for a delay in the condition for crack surface contact.

A qualitative comparison of the model predictions with other well-established models, such as the JH2 (Section 2.5.1), can be carried out. The boundary value problem is modified to idealize the sample completely defects-free and subjected to dynamic compression as it would be in the case of a SHPB experiment. The failure patterns for the two different models are presented in Figure 7.25 for the case of average rate of loading in the specimen, $\dot{\varepsilon} \approx \dot{\varepsilon}_{o,c}$. It can be seen that there is an overall qualitative agreement between the JH2 prediction (Figure 7.25(a)) and the model (Figure 7.25(b)), where $\beta = 25$ has been assumed. In both cases, failure is initiated by a series of shear cracks in a Mohr-Coulomb-sense [252, 253] although a difference in the crack plane inclination among the two cases can be observed. It has to be noted that although β is assumed constant, its effect relates only to crack initiation. After the correspondent peak stress is attained due to only deviatoric deformation in a state of pure compression, a crack surface starts to form. This establishes the condition to have a local state of tension which favours the evolution of the micro-inertia length scale l as dictated by the rate. The sensitivity of the solution on β can be assessed in Figure 7.26. It can be seen that although the general

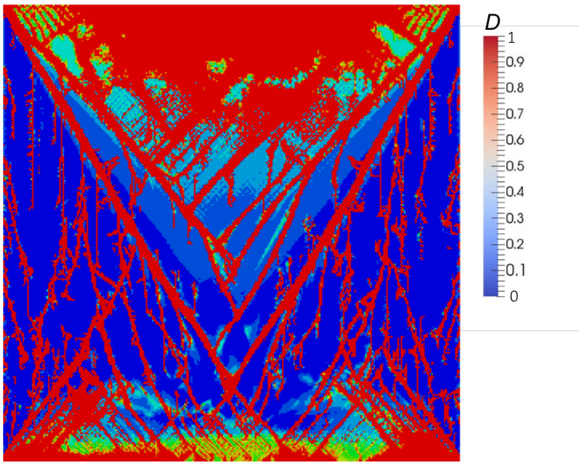

(a) JH2–crack patterns prediction

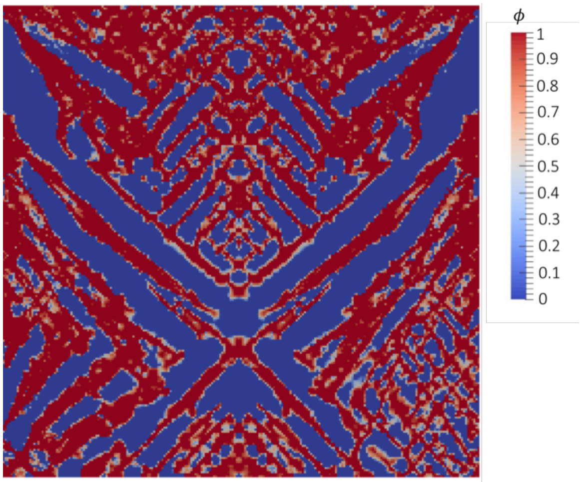

(b) Phase field model–crack patterns prediction for $\beta = 25$

Figure 7.25: Comparison between JH2 and phase field model, for $\dot{\varepsilon} \approx \dot{\varepsilon}_{o,c}$ at $\tilde{T} = 0.3$

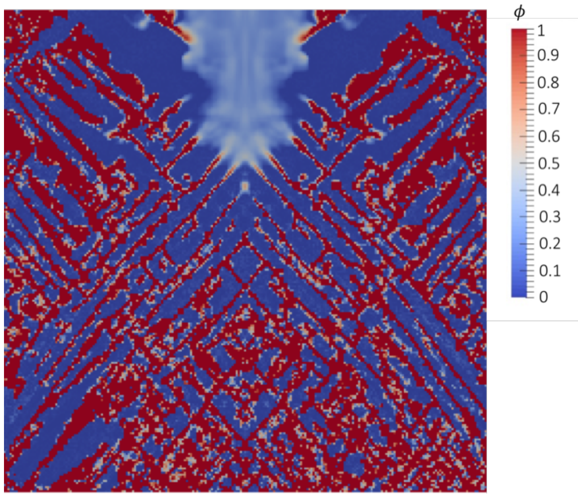

(a) Crack patterns for $\beta = 100$ at $\tilde{T} = 0.45$

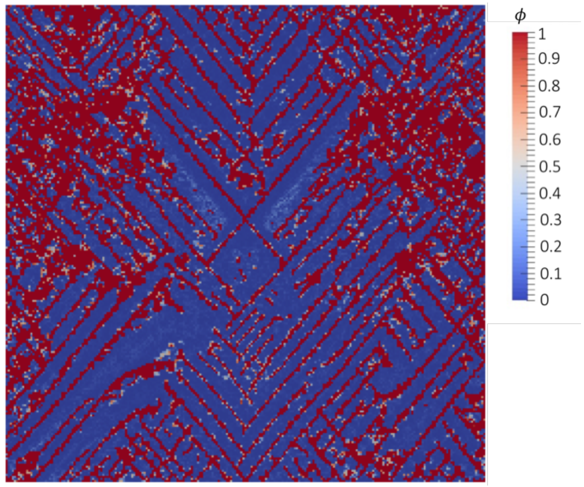

(b) Crack patterns for $\beta = 400$ at $\tilde{T} = 0.7$

Figure 7.26: Crack patterns for different β and loading rate $\dot{\varepsilon} \approx \dot{\varepsilon}_{o,c}$

shear cracks configuration is retained, extended cracking occurs at later stages, *i.e.* higher load, for increasing β with thinner diffusive zones. As the stress for softening initiation under pure compression increases with β this result confirms the importance of defining a rate-dependent scaling for its definition.

Chapter 8

Conclusion and recommendation for further work

In conclusion, a discussion summarizing the contents presented in this work is provided in this chapter. The background and associated contributions proposed to tackle some of the research challenges identified in the literature are reviewed. Based on the results achieved within the current framework a list of proposed future development efforts is suggested.

8.1 Summary

The objective of this work has been to study the pressure-rate-dependent failure characteristics of failure in nominally brittle materials.

The fracture mechanics principles which have been proposed throughout the last few decades to describe the dynamics of crack initiation and propagation have been outlined in Section 2.2. This foundation has served as a basis and link to the discussion in Section 2.3 in which evidences of rate-pressure-dependent failure in brittle materials have been provided as motivation for the subsequent development of an integrated experimental and modelling framework able to describe these phenomena. The split Hopkinson bar has been presented as the main technique to characterize rate-dependent failure behaviour and its design has been extensively reviewed in Section 7.19. In particular, the operational conditions needed to employ the apparatus for the characterization of hard-brittle ceramics, later used as a model material for its optimization, have been discussed.

As far as the computational modelling is concerned, a review of the main frameworks found in the literature has been provided in Section 2.5. These classes of models have been divided into three main branches based on the scale and physics of the failure mechanisms which the aim to capture as well as on the methodology which they rely on in order to model the configuration of the associated heterogeneities. Advantages and drawbacks of phenomenological damage-based, micromechanical-based and cohesive zone models have been identified. This has inspired the investigation of a newly-introduced class of models, namely *phase field models*, which have received great attention for their ability to describe dynamic fracture in the context of continuum diffusive interfaces. Chapter 3 has been devoted to a detailed appraisal of how this set of theories can be employed to develop governing equations and constitutive relations which describe fracture phenomena in a rather classical Griffith-sense. The main features and associated advantages of this approach can be summarized as follows:

- There is no need to introduce any explicit topological descriptor for the initiation and propagation path of a crack. The crack is rather described by a continuous, diffusive field whose evolution is described by a scalar parameter, *i.e.* the phase field parameter ϕ, which interpolates between two reference states and localise within a narrow zone l_0.

- The governing equations for the evolution of the state of deformation and ϕ, along with the constitutive relation which coupled the two *physics*, can be derived by means of a variational approach given a reference strain energy functional and a suitable choice for the damage function associated with material degradation;

- The solution to the fracture problem is therefore obtained in terms of a revised minimization procedure within which ϕ is computed as part of the solution to the derived Euler equation of motion. This advantage allows to avoid the development of ad-hoc criteria for the initiation and propagation of cracks in the medium.

- The framework enables for a flexible numerical implementation strategy which does not suffer instabilities due to loss of ellipticity and complex parameter calibration that could arise in classical continuum models. Moreover, difficulties associated with the explicit tracking of the discrete interface, as it would be required in cohesive zone type of models, are substantially reduced.

Despite the remarkable successes of these type of models, gaps in their ability to predict rate-pressure-dependent failure have been identified and addressed by means of the improved formulation presented in Chapter 4. The model has been developed in a consistent thermodynamics framework where the phase field parameter has been supplemented by its own micro-force balance law. The major proposed improvements to existing theories have relied on the formulation of a newly-introduced rate-dependent length scale associated with high-inertia near-crack tip effects as well as on the introduction of a triaxiality-based mode of failure transition to include pressure-dependent effects. It has been derived that the boundary value problem is governed by a set of coupled hyperbolic partial differential equations (4.18). This result has enabled to implement the model within an updated Lagrangian finite element framework with explicit time integration scheme, in contrast to previous contribution in the field. Hence, the progression in the development as well as the main results can be summarized as below:

- The transition law, based on local material triaxiality, has been defined in accordance with experimental evidences which have shown that a mode of failure transition occurs as the material is subjected to increasing confinement. These observations motivated the postulation of a linear scaling law for the critical energy release rate by means of a calibrating parameter β;

- The model response under uniaxial loading conditions has been analysed for different formulation of the damage function $g(\phi)$ and it has been shown that a cubic form (4.42) with small scaling parameter s reproduces a linear elastic response up to the peak stress at which softening due to material degradation and phase field evolution starts.

- A sensitivity analysis of the model on the rate of loading has shown that the mechanical response exhibits a rate-dependent nature which varies according to the choice of l.

- The stress at softening has been assumed to represent the tensile strength of the material. Therefore, a scaling law for this quantity has been employed (4.45) as a basis to obtain a correspondent rate-dependent evolution law for the micro-inertia length scale and the dynamic viscosity (4.46 - 4.48).

The model has been employed to study crack nucleation and propagation in a series of classical benchmarks in which various dynamic loading conditions have been considered and results could be compared against the experimental evidence. The main findings are listed below:

- In Chapter 5 the model has been used to study crack initiation and propagation under remote dynamic tensile loading conditions. Results on a dogbone-shaped specimen have shown that the model captures the rate-dependent response of the fracture strength as dictated by equation 4.45. A rate-dependent configuration of the fracture patterns has been observed. Subsequently a single-edge notched specimen has been analysed to assess the ability of the model to predict crack branching as induced by inertia-instabilities at increasing rates. It has been shown that, as the loading rate increases, the crack pattern configuration changes from no-branching, resembling the propagation of a seemingly quasi-static straight crack path, to single macroscopic branching and then to increasing early-stage frustrated branching. Moreover, it has been pointed out that a small, constant value for l does not capture the progressive branch formation at high rates, as a rate-dependent scaling law otherwise ensures.

- Crack propagation under remote dynamic compressive loading conditions in solids containing macroscopic pre-existing notches has been investigated in Chapter 6. Firstly symmetric impact on a single-edge notched plate has been considered. It has been shown that the model is able to capture the transition from mode-I dominant kinked to shear-driven crack propagation as the loading and the associated confinement at the initial crack-tip increases. A plate under biaxial compressive load has been examined subsequently. It has been observed that, under the absence of confinement, the model is able to capture the formation of a wing crack whose propagation path aligns with the direction of the maximum principal stress. Upon the increase of the loading rate, mixed-mode crack patterns, which include the formation of secondary cracks, have been registered. As the confinement increases the crack pattern configuration transitions from a wing crack with lower propagation speed to a macroscopic mode-II shear crack. Both the benchmarks have been subjected to a sensitivity analysis of the effect of the parameters defining the transition law for $\tilde{G}_c$.

- It has been aimed to investigate the model prediction on a real-case scenario involving the failure under dynamic compression of a ceramic alumina-based material. In order to obtain an experimental procedure which could serve as a validation/calibration baseline for the model prediction, a detailed virtual optimization of the SHPB technique had to be carried out. The study has focused on the investigation of the effect of all the variables involved in the design of the apparatus. These results have enabled to build an ad-hoc experimental setup which has been employed to characterize the material provided by the project collaborators. Simulations of the experimental conditions as applied to an ideal ceramic containing pre-existing defects have shown that a further calibration for the β parameter is required. It has been acknowledged that, to be effective, this should be performed only if the condition for crack surfaces contact can be taken into account.

8.1.1 Competitive advantages of current framework

In the following discussion, a summary of the advantages associated with the framework presented in this thesis is provided. To the best of the author's knowledge they represent a major contribution to the field of diffusive interfaces, employed for the modelling dynamic brittle fracture, and can be considered as an advancement upon which existing methodologies could be extended.

- The model presents an inherent rate dependency as a result of the addition of a newly-introduced length scale, associated with micro-inertia effects, to the phase field micro-force balance equation 4.7b. This feature enables a direct calibration as well as validation of the rate-dependent response of the model through ready-available rate-dependent strength experimental data (equation 4.45). Previous models have relied on either quasi-static or viscosity-dominant phase field equations without the capability of predicting the rate-dependent failure response, as naturally arising from the growth of the phase field parameter. In this work, the dynamic scaling law driving the evolution of l (equation 4.46) allows for a quantitative prediction of the rate-dependent stress at softening, without having to include this dependency explicitly in the constitutive equations. Material degradation is performed by a monotonic damage-like function (equation 4.42) which ensures stiffness irreversibility, in the case of oscillations induced by waves reflection, and interaction which result in stress unloading/reloading over the softening path.

- The pressure-dependency of the mode of failure has been included by postulating a transition law (equation 4.6) for the critical energy release rate based on the material triaxiality. In particular, this new feature allows to take into account the effect of material confinement on the mode of crack propagation. It can be also noted that the main scaling parameter β can be itself a function of the rate and microstructure configuration therefore allowing for the model response to be calibrated under varying regime of pure compression by means of the SHPB technique as discussed in Section 7.4.1.

- The rate dependency, as dictated by the evolution of l, in conjunction with the trialixity-dependent law, allows for the prediction of the mode of failure transition upon increasing loading rates. This result aligns with the several experimental findings on brittle amorphous polymers and would not be obtainable if otherwise these features were not included as reported in Figure 6.10.

- The model development has resulted in a set of coupled hyperbolic equations which have allowed its implementation within an updated Lagrangian framework, with explicit time integration. This implementation strategy is particularly suitable for applications involving impact and highly nonlinear loading conditions, such as impact, which would otherwise provide major complexities, if implicit numerical strategies had to be pursued.

In addition, the enhanced phase field methodology presents advantages over other modelling techniques, such as those discussed in section 2.5:

- The number of constitutive parameters and experiments associated with their calibration has reduced when compared to those required in the case of classical phenomenological models such as the JH2, although it has been shown in section 7.4.2 that both the models lead to comparable results.

- Although micro-mechanical models succeed in taking into account the effect of microscopic features such as flaws size, distribution and interaction; this is achieved at the expense of weakening the numerical stability which instead appears to be more robust in the proposed model. Reduced computational costs are also associated with the proposed model, if employed in large scale simulations, provided that l_0 is properly resolved. Moreover, the calibration of the rate-dependency micro-mechanical methods relies on assuming a rate-dependency of the dynamic stress intensity factor upon the crack-tip velocity, which is hard to measure at low scales and in the presence of multiple cracks propagating in the medium. More advanced versions, such as the one proposed by Bhat et. al. [118], include the crack-tip velocity at branching, which is challenging to quantify precisely given the highly oscillatory nature of the measurements. The model developed in this work, overcomes this limitation by incorporating this feature though a macroscopic strength measurement. On the other hand, micro-mechanical models allow to take into account the effect of crack surface interaction which, if considered, might reveal additional insights into the main mechanisms of crack propagation.

- Despite the remarkable success of discrete-interfaces model such the CZM, their main drawback associated with requirement of defining a priori the crack path is absent in the phase field method. Phase field methods have shown promising capability in predicting crack nucleation without pre-defined, ad-hoc, criterion as demonstrated in section 5.2. Moreover, the continuum formulation at the basis of the present work, does not lead to time discontinuity and traction locking problems which would otherwise arise in cohesive elements when the activation condition is computed on the basis of an interpolation of the mechanical state of neighbouring bulk elements.

8.2 Future work

Although this thesis has examined in some detail the applicability of a newly developed rate-pressure-dependent phase field mode for the modelling of dynamic brittle fracture, when used in more complex impact scenarios, more work is needed to support its proposed extended usage. Throughout the thesis, some common methodological problems in the field have been encountered that merit further work in this area. It is aimed that the research and results presented in this thesis will stimulate further interest and research studies in the field. Suggested improvements and complementary investigations which will be addressed in the future are outlined below:

- Implementation of a contact detection algorithm which can resemble the condition of closed crack surfaces to avoid element interpenetration and allows for frictional sliding. This should be developed in conjunction with an *anisotropic* split for the deviatoric component of the strain energy resulting in an adaptive degraded of the stress components.

- The simulations have not employed any technique to remove the fully degradated elements which do not contribute with any stiffness to material. It is envisaged that computational techniques based on element splitting/debonding would better resemble conditions for fragmentation and material comminution.

- Future development will include the ability to account for plastic deformation, which might arise under high level of confinement at lower scales.

- In order to reduce the computational costs due to the requirement to resolve the extrinsic length scales of the problem, *i.e.* l_0 and l, a concurrent-adaptive multi-grid refinement strategy should be explored.

References

[1] M.A. Meyers. *Dynamic behavior of materials.* John Wiley & Sons, Inc, New York, 1994.

[2] Ramanjaneyulu K. Balakrishna Bhat T. Madhu, V. and Gupta N.K. An experimental study of penetration resistance of ceramic armour subjected to projectile impact. *Int. J. Impact Eng.*, 32:337–350, 2005.

[3] Cordeiro da Silva A.R. Hild, F. Single and multiple fragmentation of brittle geomaterials. *Rev. Fr. Genie Civil*, 7:973–1002, 2003.

[4] A.J. Hsieh and J.w. Song. Measurements of ballistic impact response of novel coesxtruded PC/PMMA multilayered-composites. *J. Reinf. Plast. Compos.*, 20(3):239–254, 2001.

[5] P. Forquin. Brittle materials at high-loading rates: an open area of research. *Phil. Trans. R. Soc. A*, 375, 2017.

[6] L. B. Freund. *Dynamic fracture mechanics.* Cambridge University Press, Cambridge, 1990.

[7] A.J. Rosakis, C. Liu, and L.B. Freund. A note on the asymptotic stress field of a non-uniformly propagating dynamic crack. *Int. J. Fract.*, pages R39–R45, 1991.

[8] L.B. Freund and A.J. Rosakis. The structure of the near-tip field during transient elastodynamic crack growth. *J. Mech. Phys Solids*, 40:699–719, 1992.

[9] C. Liu and A.J. Rosakis. On the higher order asymptotic analysis of a nonuniformly propagating dynamic crack along an arbitrary path. *J. Elasticity*, 35:27–60, 1994.

[10] K. Ravi-Chandar. Dynamic fracture of nominally brittle materials. *Int. J. Fract.*, 90:83–102, 1998.

[11] M. Marder. New dynamical equation for cracks. *Phys. Rev. Lett.*, 66(19), 1991.

[12] M. Marder and S. Gross. Origin of Crack Tip Instabilities. *J. Mech. Phys. Solids*, 43(1):1–48, 1994.

[13] J. Fineberg and E. Bouchbinder. Recent developments in dynamic fracture: some perspectives. *Int. J. Fract.*, 196(1-2):33–57, 2015.

[14] E. Bouchbinder, J. Fineberg, and M. Marder. Dynamics of Simple Cracks. *Annu. Rev. Condens. Matter Phys.*, 1:371, 2010.

[15] E. Bouchbinder, A. Livne, and J. Fineberg. Weakly nonlinear fracture mechanics: Experiments and theory. *Int. J. Fract.*, 162(1-2):3–20, 2010.

[16] J.R. Rice. *Fracture.* Academic Press, London, 1968.

[17] J.S. Langer and A.E. Lobkovsky. Critical examination of cohesive-zone models in the theory of dynamic fracture. *J. Mech. Phys. Solids*, 46(9):1521–1556, 1998.

[18] F. Murnaghan. *Finite deformationof anelastic solid.* Wiley, New York, 1951.

[19] E. Bouchbinder, T. Goldman, and J. Fineberg. The dynamics of rapid fracture: instabilities, nonlinearities and length scales. *Rep. Prog. Phys.*, 77(4):046501, 2014.

[20] K Ravi-Chandar and W G Knauss. An experimental investigation into dynamic fracture: I. Crack initiation and arrest. *Int. J. Fract.*, 25(4):247–262, 1984.

[21] W. Bradley and A. Kobayashi. Fracture dynamicsâĂŤa photoelastic investigation. *Eng. Fract. Mech.*, 3:317–332, 1971.

[22] K. Ravi-Chandar and W.G. Knauss. An experimental investigation into dynamic fracture: II. Microstructural aspects. *Int. J. Fract.*, 26:65–80, 1984.

[23] M. Ramulu and A. S. Kobayashi. Mechanics of crack curving and branching - a dynamic fracture analysis. *Int. J. Fract.*, 27(3-4):187–201, 1985.

[24] J. Dempsey and P. Burgers. Dynamic crack branching in brittle solids. *Int. J. Fract.*, 27:203–213, 1985.

[25] E. Sharon, S. Gross, and J. Fineberg. Local Crack Branching as a Mechanism for Instability in Dynamic Fracture, 1995.

[26] E. Sharon and J. Fineberg. Microbranching instability and the dynamic fracture of brittle materials. *Phys. Rev. B. Condens. Matter*, 54(10):7128–7139, sep 1996.

[27] K. Ravi-Chandar and W.G. Knauss. An experimental investigation into dynamic fracture: III. On steady-state crack propagation and crack branching. *Int. J. Fract.*, 26:141–154, 1984.

[28] J. Fineberg, S.P. Gross, M. Marder, and H.L Swinney. Fast Cracks. 45(10), 1992.

[29] E.H. Yoffe. LXXV. The moving griffith crack. *London, Edinburgh, Dublin Philos. Mag. J. Sci.*, 42(330):739–750, 1951.

[30] A. Livne, G. Cohen, and J. Fineberg. Universality and Hysteretic Dynamics in Rapid Fracture. *Phys. Rev. Lett.*, 94(22):224301, 2005.

[31] T.G. Boue, G. Cohen, and J. Fineberg. Origin of the Microbranching Instability in Rapid Cracks. *Phys. Rev. Lett.*, 114(February):054301, 2015.

[32] P. D. Washabaugh and W. G. Knauss. A reconciliation of dynamic crack velocity and Rayleigh wave speed in isotropic brittle solids. *Int. J. Fract.*, 65:97–114, 1994.

[33] A J Rosakis, O Samudrala, and D Coker. Intersonic shear crack growth along weak planes. *Mater. Res. Innov.*, 3(4):236–243, 2000.

[34] H. Gao. Surface roughening and branching instabilities in dynamic fracture. *J. Mech. Phys. Solids*, 41(3):457–486, 1993.

[35] H. Gao. A theory of local limiting speed in dynamic fracture. *J. Mech. Phys. Solids*, 44(9):1453–1474, 1996.

[36] M.J. Buehler and H. Gao. Dynamical fracture instabilities due to local hyperelasticity at crack tips. *Nature*, 439(7074):307–310, 2006.

[37] M.J. Buehler, F.F. Abraham, and H. Gao. Hyperelasticity governs dynamic fracture at a critical length scale. *Nature*, 426(6963):141–146, 2003.

[38] R.S. Karedla and J. N. Reddy. Modeling of crack tip high inertia zone in dynamic brittle fracture. *Eng. Fract. Mech.*, 74(13):2084–2098, 2007.

[39] J.F. Kalthoff. Modes of dynamic shear failure in solids. *Int. J. Fract.*, 101(14):1–31, 2000.

[40] J.F. Kalthoff and S. Winkler. Failure mode transition of high rates of shear loading. In *Proceedings of the International Conference on Impact Loading and Dynamic Behavior of Materials*, pages 185–95. In: Chiem CY, Kunze H-D, Meyer L.W., 1988.

[41] Lu J. Yang B. Ravi-Chandar, K and Z. Zhu. On the failure mode transitions in polycarbonate under dynamic mixed-mode loading. *Int. J. Fract.*, 101:33–72, 2000.

[42] K. Ravi-Chandar. On the failure mode transitions in polycarbonate under dynamic mixed-mode loading. *Int. J. Solids. Struc.*, 32(6/7):925–938, 1995.

[43] J. F. Kalthoff and A. Bürgel. Influence of loading rate on shear fracture toughness for failure mode transition. *Int. J. Impact Eng.*, 30(8-9):957–971, 2004.

[44] K.B. Broberg. On crack paths. *Eng. Fract. Mech.*, 28(5-6):663–679, 1987.

[45] D. Rittle and H. Maigre. On mixed-mode dynamic crack initiation in brittle solids. In *Proceedings of the 9th International Conference on Fracture*, pages 2941–2948. Pergamon, 1997.

[46] C. Renshaw and E. Schulson. Universal behaviour in compressive failure of brittle materials. *Nature*, 412:897–900, 2001.

[47] W.E. Brace and E.G. Bombolakis. A note on brittle crack growth in compression. *J. Geophys. Res.*, 68:3709–3713, 1963.

[48] H. Horii and S. Nemat-Nasser. Brittle Failure in Compression : Splitting, Faulting and Brittle-Ductile Transition. *Philos. Trans. R. Soc. London*, 319(1549):337–374, 1986.

[49] H.B. Frost and M.F. Asbhy. *Deformation-Mechanism Maps.* Pergamon Press, Oxford, 1982.

[50] Walley S.M. Field, J.E., W.G. Proud, H.T. Goldrein, and C.R. Sivior. Review of experimental techniques for high rate deformation and shock studies. *Int. J. Imp. Eng.*, 30, 2004.

[51] K.T. Ramesh. High strain rate and impact experiments.

[52] J. Hopkinson. On the rupture of iron wire by a blow (1872), Article 38. *Orig. Pap. late John Hopkinson*, 2:316–320, 1901.

[53] J. Hopkinson. Further experiments on the rupture of iron wire(1872), Article 39. *Orig. Pap. late John Hopkison*, 2:316–320, 1901.

[54] B. Hopkinson. A method of measuring the pressure produced in the detonation of high explosives or by the impact of bullets. *Philos. Trans. R. Soc. London*, 213, 1913.

[55] B. Hopkinson. The Effects of Momentary Stresses in Metals. *Proceeding R. Soc. London, Ser. A.*, 74:498–506, 1914.

[56] R. M. Davies. A Critical Study of the Hopkinson Pressure Bar. *Phylosophical Trans. R. Soc. London*, 240(821):375–457, 1948.

[57] L. Pochhammer. Ueber die Fortpflanzungsgeschwindigkeiten kleiner Schwingungen in einem unbegrenzten isotropen Kreiscylinder. *J. für die reine und Angew. Math.*, 81, 1876.

[58] Chree C. The Equations of an Isotropic Elastic Solid in Polar and Cylindrical Coordinates, Their Solutions and Applications. *Trans. Cambridge Philos. Soc. Math. Phys. Sci.*, 14:251–369, 1889.

[59] H Kolsky. An investigation of the mechanical properties of materials at very high rates of loading. *Proc. Phys. Soc. Sect. B*, 62, 1949.

[60] U.S. Lindholm and L.M. Yeakley. High strain-rate testing: Tension and compression. *Exp. Mech.*, 8(1):1–9, 1968.

[61] T. Nicholas. Tensile testing of materials at high rates of strain. *Exp. Mech.*, 21(5):177–185, may 1981.

[62] Int ASM. *High strain rate shear testing*. ASM Int, 2000.

[63] A. Gilat. *Torsional Kolsky bar testing*. ASM Int, 2000.

[64] S. Nemat-Nasser, Jon B. Isaacs, and J. Rome. *Triaxial Hopkinson tecniques*. ASM Int, 2000.

[65] Weinong W. Chen and Bo Song. *Split Hopkinson (Kolsky) Bar Design, Testing and Applications*. Springer, 2011.

[66] G. Ravichandran and G. Subhash. Critical Appraisal of Limiting Strain Rates for Compression Testing of Ceramics in a Split Hopkinson Pressure Bar. *J. Am. Ceram. Soc.*, 77(1):263–267, jan 1994.

[67] P.S. Follansbee and C. Frantz. Wave Propagation in the Split Hopkinson Pressure Bar. *J. Eng. Mater. Technol.*, 105(1):61–66, 1983.

[68] Hunter S.C. Davies, R.M. The Dynamic Compression Testing of Solids by the Method of the Split Hopkinson Pressure Bar. *J. Mech. Phys Solids*, 11:375–457, 1963.

[69] S. Nemat-Nasser, J.B. Isaacs, and J.E. Starrett. Hopkinson Techniques for Dynamic Recovery Experiments. In *Math. Phys. Sci. Vol.*, volume 435, pages 371–391. The Royal Society, 1991.

[70] G. Sunny, F. Yuan, V. Prakash, and J. Lewandowski. Design of Inserts for Split-Hopkinson Pressure Bar Testing of Low Strain-to-Failure Materials. *Exp. Mech.*, 49(4):479–490, may 2008.

[71] S. Ellwood, L.J. Griffiths, and D. J. Parry. Materials testing at high constant strain rates. *J. Phys. E Sci. Instrum*, 15:1–4, 1982.

[72] F. Benassi and Marcilio Alves. Pulse shaping in the split hopkinson pressure bar test. 2006.

[73] R. Naghdabadi, M.J. Ashrafi, and J. Arghavani. Experimental and numerical investigation of pulse-shaped split Hopkinson pressure bar test. *Mater. Sci. Eng. A*, 539:285–293, mar 2012.

[74] R. Gerlach, S.K. Sathianathan, C. Siviour, and N. Petrinic. A novel method for pulse shaping of Split Hopkinson tensile bar signals. *Int. J. Impact Eng.*, 38(12):976–980, dec 2011.

[75] W. Chen, G Subhash, and G. Ravichandran. Evaluation of ceramic specimen geometries used in split Hoplinson pressure bar. *DYMAT J.*, 1:193–210, 1994.

[76] J.W. Mccauley and G.D. Quinn. Special Workshop : Kolsky / Split Hopkinson Pressure Bar Testing of Ceramics. Technical Report September, Army Research Laboratory, 2006.

[77] D.A. Gorham. Specimen inertia in high strain-rate compression. *Phys. D Nonlinear Phenom.*, 22:1888–1893, 1989.

[78] Effect of Specimen Size in the Kolsky Bar. *Procedia Eng.*, 10:2663–2671, 2011.

[79] Yubin Lu. Determination of the radial inertia-induced transition strain-rate in split Hopkinson pressure bar tests. *J. Mech. Sci. Technol.*, 25(11):2775–2780, 2011.

[80] L.D. Bertholf and C.H. Karnes. Two-dimensional analysis of the split Hopkinson pressure bar system. *J. Mech. Phys. Solids*, 23, 1975.

[81] P.S. Follansbee. The Hopkinson bar, 1985.

[82] I.W. Halll and M. Gurden. Split Hopkinson pressure bar compression testing of an aluminum alloy: effect of lubrificant. *J. Mater. Sci. Lett.*, 22:1533–1535, 2003.

[83] M. Alves, D. Karagiozova, G.B. Micheli, and M.A.G. Calle. Limiting the influence of friction on the split Hopkinson pressure bar tests by using a ring specimen. *Int. J. Impact Eng.*, 49:130–141, nov 2012.

[84] C.A. Tracy. A Compression Test for High Strength Ceramics. *J. Test. Eval.*, 15:14–19, 1987.

[85] W.R. Blumenthal. High Strain Rate Compression Testing of Ceramics and Ceramic Composites. In *High Strain Rate Compression Test. Ceram. Ceram. Compos.*, Cocoa Beach, FL, 2005.

[86] W.A. Dunlay, C.A. Tracy, and P.J. Perrone. A Proposed Uniaxial Compression Test for High Strength Ceramics. Technical report, Us Army Materials Technology Laboratory, 1989.

[87] A. Gilat, T.E. Schmidt, and A.L. Walker. Full Field Strain Measurement in Compression and Tensile Split Hopkinson Bar Experiments. *Exp. Mech.*, 49(2):291–302, aug 2008.

[88] J. Lemaitre and R. Desmorat. *Engineering damage mechanics*. Springer, Berlin-Verlag, 2005.

[89] G.R. Johnson and T.J. Holmquist. An improved computational constitutive model for brittle materials. *AIP Conf. Proc.*, 309:981–984, 1994.

[90] T.J. Holmquist and G.R. Johnson. A Computational Constitutive Model for Glass Subjected to Large Strains, High Strain Rates and High Pressures. *J. Appl. Mech.*, 78(5), 2011.

[91] G.R. Johnson, T.J. Holmquist, and S.R. Beissel. Response of aluminum nitride (including a phase change) to large strains, high strain rates, and high pressures. *J. Appl. Mech.*, 94(3):1639, 2003.

[92] C.E. Anderson. A review od computational ceramic armor modeling. In *Advances in ceramic armor II*, volume 27. Ceramic Engineering and Science Proceedings, 2007.

[93] X. Zhang, N. Zhang, and Y. Li. Numerical study on anti?penetration process of alumina ceramic (AD95) to tungsten long rod projectiles. *Int. J. Mod. Phys. B*, 15:2091–2103, 2011.

[94] D.W. Templeton, T.J. Holmquist, H.W. Meyer, D.J. Grove, and B. Leavy. A comparison of ceramic material models. In *AProceedings of the Ceramic Armor by Design Symposium*, pages 299–308. eramic Engineering and Science Proceedings, 2001.

[95] D.C. Drucker and W. Prager. Soil mechanics and plastic analysis or limit design. *Q. Appl. Math.*, 10:157–162, 1952.

[96] C.H.M. Simha, S.J. Bless, and A. Bedford. Computational modeling of the penetration response of a high purity ceramic. *Int. J. Impact Eng.*, 27(1):65–86, 2002.

[97] R.M. Brannon, J.M. Wells, and O.E. Strack. Validating theories for brittle damage. *Metall. Mater. Trans. A*, 2007.

[98] V.S. Deshpande and A.G. Evans. Inelastic deformation and energy dissipation

in ceramics : A mechanism-based constitutive model. *J. Mech. Phys. Solids*, 56:3077–3100, 2008.

[99] B. Budiansky and R.J. O'Connell. Elastic moduli of a cracked solid. *Int. J. Solids Struct*, 12:81–97, 1976.

[100] K. Huang, K.X. Hu, and A. Chandra. A generalized self?consistent mechanics method for microcracked solids. *J. Mech. Phys. Solids*, 42(8):1273–1291, 1994.

[101] P. Tapponnier and W. Brace. Development of stress-induced microcracks in Westerly Granite. *Int. J. Rock Mech. Min. Sci. Geomech. Abstr*, 13(4):103–112, 1976.

[102] M.F. Ashby and S.D. Hallam. The failure of brittle solids containing small cracks under compressive stress states. *Acta Metall.*, 34(3):497–510, 1976.

[103] M. Jeyakumaran and J.W. Rudnicki. The sliding wing crack – Again! *Geophys. Res. Lett*, 22(21):2901–2904, 1995.

[104] S. Nemat-Nasser and H. Horii. Compression-induced nonplanar crack extension with application to splitting, exfoliation, and rockburst. *J. Geophys. Res.*, 87(B8):6805, 1982.

[105] H. Horii and S. Nemat-Nasser. Elastic fields of interacting inhomogeneities. *Int. J. Solids Struct.*, 21(1):731–745, 1985.

[106] M. Kachanov. Elastic solids with many cracks: A simple method of analysis. *Int. J. Solids Struct.*, 23(1):731–745, 1987.

[107] I. Sevastianov and M. Kachanov. On elastic compliances of irregularly shaped cracks. *Int. J. Solids Struct.*, 23(1):245–257, 2002.

[108] M.F. Asbhy and C.G. Sammis. The damage mechanics of brittle solids in compression. *Pure Appl. Geophys.*, 133(3):489–521, 1990.

[109] S. Nemat-Nasser and H. Deng. Strain-rate effect on brittle failure in compression. *Acta Metall.*, 42(3):1013–1024, 1994.

[110] G. Ravichandran and G. Subhash. A micromechanical model for high strain rate behavior of ceramics. *Int. J. Solids Struct.*, 3(94):2627–2646, 1995.

[111] C. Huang, G. Subhash, and S.J. Vitton. A dynamic damage growth model for uniaxial compressive response of rock aggregates. *Mech. Mater.*, 34(5):267–277, 2002.

[112] D.E. Grady and Lipkin. Criteria for impulsive rock fracture. *Geophys. Res. Lett.*, 7(4):255–258, 1980.

[113] B. Paliwal and K.T. Ramesh. An interacting micro-crack damage model for failure of brittle materials under compression. *J. Mech. Phys. Solids*, 56(3):896–293, 2008.

[114] X.H. Xu, S.P. Ma, M.F. Xia, F.J. Ke, and Y.L. Bai. Damage evaluation and damage localization of rock. *Theor. Appl. Fract. Mech.*, 42(2):131–138, 2004.

[115] B. Paliwal, K.T. Ramesh, and J.W. McCauley. Direct observation of the dynamic compressive failure of a transparent polycrystalline ceramic (AlON). *J. Am. Ceram. Soc.*, 42(2):2128–2133, 2006.

[116] R. Hill and J.R. Rice. Elastic potentials and the structure of inelastic constitutive laws. *SIAM J. Appl. Math.*, 25(3):448–461, 1973.

[117] R.J. Charles. Dynamic fatigue of glass. *J. Appl. Phys.*, 29(12):1657–1662, 1958.

[118] H.S. Bhat, A.J. Rosakis, and C.G. Sammis. A micromechanics based constitutive model for brittle failure at high strain rates. *J. Appl. Mech.*, 79(3), 2012.

[119] D.S Dugdale. Yielding of steel sheets containing slits. *J. Mech. Phys. Solids*, 8(2):100–104, 1960.

[120] G. Barenblatt. The formation of equilibrium cracks during brittle fracture. General ideas and hypotheses. Axially-symmetric cracks. *J. Appl. Math. Mech.*, 23(3):622–636, 1959.

[121] R. De Borst, M.A. Gutierrez, G.N. Wells, J.J.C. Remmers, and H. Askes. Cohesive-zone models, higher-order continuum theories and reliability methods for computational failure analysis. *Int. J. Numer. Methods Eng.*, 60(1):289–315, 2004.

[122] A. Needleman. An analysis of tensile decohesion along an interface. *J. Mech. Phys. Solids*, 38(3):289–324, 1990.

[123] J.L. H́ogberg. Mixed mode cohesive law. *Int. J. Fract*, 141(3–4):549–559, 2006.

[124] K. Keller, S. Weihe, T. Siegmund, and B. Kŕoplin. Generalized Cohesive Zone Model: incorporating triaxiality dependent failure mechanisms. *Comput. Mater. Sci.*, 16(1–4):267–274, 1999.

[125] F. Zhou, J-F Molinari, and T. Shioya. A rate-dependent cohesive model for simulating dynamic crack propagation in brittle materials. *Eng. Fract. Mech.*, 72(9):1393–1410, 2005.

[126] L. Liu and S. Li. A Finite Temperature Multiscale Interphase Zone Model and Simulations of Fracture. *J. Eng. Mater. Technol.*, 134(3), 2012.

[127] J. Qian and S. Li. Application of Multiscale Cohesive Zone Model to Simulate Fracture in Polycrystalline Solids. *J. Eng. Mater. Technol.*, 133(1):1393–1410, 2011.

[128] X. Zeng and S. Li. A multiscale cohesive zone model and simulations of fractures. *Comput. Methods Appl. Mech. Eng.*, 133(1):547–556, 2010.

[129] A. Needleman. Some Issues in Cohesive Surface Modeling. *Procedia IUTAM*, 10:221–246, 2014.

[130] M. Elices, G.V. Guinea, J. Gómez, and J. Planas. The cohesive zone model: advantages, limitations and challenges. *Eng. Fract. Mech.*, 69(2):137–163, 2002.

[131] A. Turon, C.G. Dávila, P.P. Canahno, and J. Costa. An engineering solution for mesh size effects in the simulation of delamination using cohesive zone models. *Eng. Fract. Mech.*, 74(10):1665–1682, 2007.

[132] X.P. Xu and A. Needleman. Numerical simulations of fast crack growth in brittle solids. *J. Mech. Phys. Solids*, 42(9):253–275, 1994.

[133] X.P. Xu and A. Needleman. Numerical simulations of dynamic interfacial crack

growth allowing for crack growth away from the bond line. *Int. J. Fract.*, 74:253–275, 1995.

[134] H.D. Espinosa, P.D. Zavattieri, and K.D. Sunil. A finite deformation continuum/discrete model for the description of fragmentation and damage in brittle materials. *J. Mech. Phys. Solids*, 46(10):1909–1942, 1998.

[135] H.D. Espinosa. On the dynamic shear resistance of ceramic composites and its dependence on applied multiaxial deformation. *Int. J. Solids Struct.*, 32(21):3105–3128, 1995.

[136] H.D. Espinosa and N.S. Brar. Dynamic failure mechanisms of ceramic bars : Experiments and numerical simulations. *J. Mech. Phys. Solids*, 43(10):1615–1638, 1995.

[137] P.D. Zavattieri, P.V. Raghuram, and H.D. Espinosa. A computational model of ceramic microstructures subjected to multiNaxial dynamic loading. *J. Mech. Phys. Solids*, 49(1):27–68, 2001.

[138] P.D. Zavattieri and H.D. Espinosa. Grain level analysis of crack initiation and propagation in brittle materials. *Acta Mater.*, 49(20):4291–4311, 2001.

[139] P.G. Nittur, S. Maiti, and P.H. Geubelle. Grain-level analysis of dynamic fragmentation of ceramics under multi-axial compression. *J. Mech. Phys. Solids*, 56(3):993–1017, 2008.

[140] M. Ortiz and G.T. Camacho. Computational modelling of impact damage in brittle materials. *Int. J. Solids Struct.*, 33(2):2899–2938, 1996.

[141] M. Ortiz and G.T. Camacho. Adaptive Lagrangian modelling of ballistic penetration metallic targets. *Comput. Methods Appl. Mech. Eng*, 96, 1997.

[142] A. Pandolfi, P. Krysl, and M. Ortiz. Finite element simulation of ring expansion and fragmentation: The capturing of length and time scales through cohesive models of fracture. *Comput. Methods Appl. Mech. Eng.*, 95:279–299, 1999.

[143] A. Pandolfi and M. Ortiz. An Efficient Adaptive Procedure for Three?Dimensional Fragmentation Simulations. *Eng. Comput.*, 18(2):148–159, 2002.

[144] R.C. Yu, G. Ruiz, and A. Pandolfi. Numerical investigation on the dynamic behavior of advanced ceramics. *Eng. Fract. Mech.*, 71(4–6):897–911, 2004.

[145] R.C. Yu, G. Ruiz, and A. Pandolfi. Extrinsic cohesive modelling of dynamic fracture and microbranching instability in brittle materials. *Int. J. Numer. Methods Eng.*, 72:893–923, 2007.

[146] K. Ravi-Chandar and B. Yang. On the role of microcracks in the dynamic fracture of brittle materials. *J. Mech. Phys. Solids*, 72(4):535–563, 1997.

[147] R.H. Kraft and J.F. Molinari. A statistical investigation of the effects of grain boundary properties on transgranular fracture. *Acta Mater.*, 56(17):4739–4749, 2008.

[148] R.H. Kraft, J.F. Molinari, K.T. Ramesh, and D.H. Warner. Computational micromechanics of dynamic compressive loading of a brittle polycrystalline material using a distribution of grain boundary properties. *J. Mech. Phys. Solids*, 56(8):2618–2641, 2008.

[149] S. Levy and J.F Molinari. Dynamic fragmentation of ceramics, signature of defects and scaling of fragment sizes. *J. Mech. Phys. Solids*, 58(1):12–26, 2010.

[150] K.D. Papoulia, C.H. Sam, and S.A. Vavasis. Time continuity in cohesive finite element modeling. *Int. J. Numer. Methods Eng.*, 58(5):679–701, 2003.

[151] J.R. Rice. *Statistical Physics.* Pergamon Press, Oxford, 1980.

[152] G.A. Francfort and J.-J. Marigo. Revisiting brittle fracture as an energy minimization problem. *J. Mech. Phys. Solids*, 46(8):1319–1342, 1998.

[153] B. Bourdin, G.a. Francfort, and J-J. Marigo. Numerical experiments in revisited brittle fracture. *J. Mech. Phys. Solids*, 48(4):797–826, apr 2000.

[154] M. Ambati, R. Kruse, and L. De Lorenzis. A review on phase field models of brittle fracture and a new fast hybrid formulation. *Comput. Mech.*, 55(2):383–405, 2016.

[155] I.S. Aranson and Vinokur V.M. Kalatsky, V.A. Continuum field description of crack propagation. *Phys. Rev. Lett.*, 85:118–121, 2000.

[156] K.N.G. Fuller, P.G. Fox, and J.E. Field. The Temperature Rise at the Tip of Fast-Moving Cracks in Glassy Polymers. *Proc. R. Soc. London*, 341(2):537, 2016.

[157] A. Karma, D.A. Kessler, and H. Levine. The Temperature Rise at the Tip of Fast-Moving Cracks in Glassy Polymers. *Phys. Rev. Letter*, 87, 2001.

[158] V. Hakim and A. Karma. Laws of crack motion and phase-field models of fracture. *J. Mech. Phys. Solids*, 57(2):342–368, feb 2009.

[159] H. Henry and Levine H. Dynamic instabilities of fracture under biaxial strain using a phase field model. *Phys. Rev. Letter*, 93, 2004.

[160] J.M Ball and R.D. James. Fine phase mixtures as minimizers of energy. *Arch. Rat. Mech. Anal.*, 100:13–52, 1987.

[161] G.A. Francoft and J.J. Marigo. Fine phase mixtures as minimizers of energy. *Eur. J. Mech. A/Solids*, 12(2):149–189, 1987.

[162] B. Bourdin, G.A. Francfort, and J.J. Marigo. The Variational Approach to Fracture. *J. Elast.*, 3:5–148, 2008.

[163] B. Bourdin, C. J. Larsen, and C. L. Richardson. A time-discrete model for dynamic fracture based on crack regularization. *Int. J. Fract.*, 168(2):133–143, nov 2010.

[164] M.J. Borden, C.V. Verhoosel, M.A. Scott, T.J.R. Hughes, and C.M. Landis. A phase-field description of dynamic brittle fracture. *Comput. Methods Appl. Mech. Eng.*, 217-220:77–95, apr 2012.

[165] C. Miehe, F. Welschinger, and M. Hofacker. Thermodynamically consistent phase-field models of fracture : Variational principles and multi-field FE implementations. *Int. J. Numer. Methods Eng.*, 83(March):1273–1311, 2010.

[166] C. Hofacker, M. Miehe. Continuum phase field modeling of dynamic fracture: variational principles and staggered FE implementation. *Int. J. Fract.*, 178(2):113–129, 2012.

[167] C.J. Larsen. Existance of solutions to a regularized model of dynamic fracture. *Math. Models Methods. Appl. Sci.*, 20(2):133–143, 2010.

[168] A. Schl´uter, A. Willenb´ucher, C. Kuhn, and R. M´uller. Existance of solutions to a regularized model of dynamic fracture. *Comput. Mech.*, 54(2):1141–1161, 2014.

[169] D. Munford and J. Shah. Optimal approximation by piecewise smooth functions and associated variational problems. *Commun. Pur. Appl. Math.*, 42(2):577–685, 1989.

[170] L. Amrbosio and V.M. Tortorelli. Approximation of functional depending on jumps by elliptic functional via Γ-convergence. *Commun. Pur. Appl. Math.*, 43(8):577–685, 1990.

[171] A. Giovanni. Variational models for phase transition. an approach via γ-convergence. In G. Buttazzo, A. Marino, and M.K.V. Murthy, editors, *Calculus of variation and partial differential equations. Topics on geometrical evolution problems and degree theory*, pages 95–114. Springer-Verlag, Berlin, 2004.

[172] A. Chambolle. An approximation result for special functions with bounded deformation. *J. Math. Pures Appl.*, 50(2):2513–2537, 2004.

[173] R. de Borst and C. V. Verhoosel. Gradient damage vs phase-field approaches for fracture: Similarities and differences. *Comput. Methods Appl. Mech. Eng.*, 2016.

[174] M.J. Borden, T.J.R. Hughes, C.M. Landis, and C.V. Verhoosel. A higher-order phase-field model for brittle fracture: Formulation and analysis within

the isogeometric analysis framework. *Comput. Methods Appl. Mech. Eng.*, 273(0704):100–118, may 2014.

[175] M.N. da Silva, F.P. Duda, and E. Fried. Sharp-crack limit of a phase-field model for brittle fracture. *J. Mech. Phys. Solids*, 61(11):2178–2195, nov 2013.

[176] M.E. Gurtin and P. Podio-Guidugli. Configurational forces and the basic laws for crack propagation. *J. Mech. Phys. Solids*, 44(6):905–927, jun 1996.

[177] L. Amrbosio and V.M. Tortorelli. On the approximation of free discontinuity problems. *Boll. Un. Mat. Ital. B*, 6(1):577–685, 1992.

[178] G. Bellettini and A. Coscia. Discrete approximation of a free discontinuity problem. *Numer. Func. Anal. Opt.*, 15(3-4):201–224, 1994.

[179] B. Bourdin. Image segmentation with a finite element method. *M2AN Math. Model. Numer. Anal.*, 33(2):229–244, 1999.

[180] B. Bourdin. Numerical implementation of the variational formulation of quasi-static brittle fracture. *Interfaces Free Bound.*, 33(2):411–430, 2007.

[181] G. Del Piero, G. Lancioni, and R. March. A variational model for fracture mechanics: Numerical experiments. *J. Mech. Phys. Solids*, 55(12):2513–2537, 2007.

[182] A. Giacomini. Ambrosio-Tortorelli approximation of quasi-static evolution of brittle fractures. *Calc. Var. Partial Differ. Equ.*, 22(2):129–172, 2005.

[183] G. Lancioni and G. Royer-Carfagni. The variational approch to fracture mech-

anics: A practical application to the French Panthéon in Paris. *J. Mech. Phys. Solids*, 55(12):2513–2537, 2007.

[184] S. Burke, C. Ortner, and S'uli. An adaptive finitel element approximation of a variational model of brittle fracture. *SIAM J. Numer. Anal.*, 48(3):2513–2537, 2010.

[185] A. Braides. *Approximation of Free-Discontinuity Problems.* Springer, Berlin, 1998.

[186] C. Miehe, M. Hofacker, and F. Welschinger. A phase field model for rate-independent crack propagation: Robust algorithmic implementation based on operator splits. *Comput. Methods Appl. Mech. Eng.*, 199(45-48):2765–2778, nov 2010.

[187] C. Miehe, L.M. Sch'anzel, and H. Ulmer. Phase field modeling of fracture in multi-physics problems. Part I. Balance of crack surface and failure criteria for brittle crack propagation in thermo-elastic solids. *Comput. Method. Appl. Mech. Eng.*, 294:489–495, 2001.

[188] M. Hofacker and C. Miehe. A phase field model of dynamic fracture : Robust field updates for the analysis of complex crack patterns. *Int. J. Numer. Methods Eng.*, 93(July 2012):276–301, 2013.

[189] F.P. Duda, A. Ciarbonetti, P.J. Sánchez, and A.E. Huespe. A phase-field/gradient damage model for brittle fracture in elasticâĂŞplastic solids. *Int. J. Plast.*, 65:269–296, 2015.

[190] C. McAuliffe and H. Waisman. A unified model for metal failure capturing shear banding and fracture. *Int. J. Plast.*, 65:131–151, 2015.

[191] C. McAuliffe and H. Waisman. A coupled phase field shear band model for ductile-brittle transition in notched plate impacts. *Comput. Methods Appl. Mech. Eng.*, 305:173–195, 2016.

[192] M.J. Borden, T.J.R. Hughes, C.M. Landis, A. Anvari, and I.J. Lee. A phase-field formulation for fracture in ductile materials: Finite deformation balance law derivation, plastic degradation, and stress triaxiality effects. *Comput. Methods Appl. Mech. Eng.*, 2016.

[193] C. Miehe, M. Hofacker, L.-M. Schänzel, and F. Aldakheel. Phase field modeling of fracture in multi-physics problems. Part II. Coupled brittle-to-ductile failure criteria and crack propagation in thermo-elasticâĂŞplastic solids. *Comput. Methods Appl. Mech. Eng.*, pages 1–37, 2015.

[194] M. Ambati, R. Kruse, and L. De Lorenzis. A phase-field model for ductile fracture at finite strains and its experimental verification. *Comput. Mech.*, 57(1):149–167, 2016.

[195] Z. Wilson, M.J. Borden, and C.M. Landis. A phase-field model for fracture in piezoelectric ceramics. *Int. J. Fract.*, 183(2):135–153, oct 2013.

[196] Z. Wilson and C.M. Landis. Phase-field modeling of hydraulic fracture. *J. Mech. Phys. Solids*, 96:264–290, 2016.

[197] H. Amor, J. Marigo, and C. Maurini. Regularized formulation of the variational

brittle fracture with unilateral contact: Numerical experiments. *J. Mech. Phys. Solids*, 57(8):1209–1229, 2009.

[198] Ramsey J.M. and Chester F.M. Hybrid fracture and the transition from extension fracture to shear fracture. *Nature*, 428:2482–2499, March 2004.

[199] E. Fried and M. E. Gurtin. Dynamic solid-solid transitions with phase characterized by an order parameter. *Phys. D Nonlinear Phenom.*, 72, 1993.

[200] E. Fried. The configurational and standard force balances are not always statements of a single law. *Proceeding R. Soc. London, Ser. A.*, 2002.

[201] E. Fried and M.E. Gurtin. Dynamic solid-solid transitions with phase characterized by an order parameter. *Phys. D Nonlinear Phenom.*, 72(4):287–308, may 1994.

[202] Capriz. *Continua with microstructures*, volume 37. 1989.

[203] M.A. Goodman and S.C. Cowin. A continuum theory for granular materials. *Arch. Rational Mech. Anal.*, 44:249–266, 1972.

[204] B.D. Coleman and W. Noll. Material symmetry and thermostatic inequalities in finite elastic deformations. *Arch. Rational Mech. Anal.*, 15:87–11, 1964.

[205] X. Zhou and K. K. Tamma. On the applicability and stress update formulations for corotational stress rate hypoelasticity constitutive models. *Finite Elem. Anal. Des.*, 39(8):783–816, 2003.

[206] H. Stolarski and T. Belytschko. Large deformation, rigid-plastic dynamics by an extreme principle. *Comput. Methods Appl. Mech. Eng.*, 21:217–230, 1980.

[207] C. Kuhn, A. Schlüter, and R. Müller. On degradation functions in phase field fracture models. *Comput. Mater. Sci.*, 108:374–384, 2015.

[208] D. Gregoire, L.B. Rojas-Solano, and G. Pjaudier-Cabot. Failure and size effect for notched and unnotched concrete beams. *Int. J. Numer. Anal. Meth. Geomech.*, 37:1434–1452, 2013.

[209] F.J. Gomez, M. Elices, and J. Planas. The cohesive crack concept: application to PMMA at -60^0 C. *Eng. Fract. Mech.*, 72:1268–1285, 2005.

[210] Z.P. Bažant. Scaling laws in mechanics of failure. *J. Eng. Mech.*, 121(1):679–701, 2003.

[211] J.S. Archer and A.J. Lesser. Shear Band Formation and Mode II Fracture of Polymeric Glasses, volume = 49, year = 2011. *Poly. Phys.*, (2):103–114.

[212] Klepaczko J.R., Y.V. Petrov, S.A. Atroshenko, P. Chevrier, G. D. Fedorovsky, S. I. Krisosheev, and A. A. Utkin. Behavior of particle-filled polymer composite under static and dynamic loading. *Eng. Fract. Mech.*, 75:136–152, 2008.

[213] T. Gomez del Rio and J. Rodriguez Perez. Elastic wave propagation in cylindrical bars after brittle failures: Application to spalling tests. *Int. J. Impact Eng.*, 34:377–393, 2007.

[214] A. Shukla, H. Nigam, and H. Zervas. Effect of stress field parameters on dynamic crack branching. *Eng. Fract. Mech.*, 36(3):429–438, 1990.

[215] E. Katzav, M. Adda-Bedia, and R. Arias. Theory of dynamic crack branching in brittle materials. *Int. J. Fract.*, 143(3):41, 2006.

[216] N. Murphy, M. Ali, and A. Ivankovic. Dynamic crack bifurcation in PMMA. *Eng. Fract. Mech.*, 73:2569–2587, 2006.

[217] A. Schluter, A. Willenbucher, C. Kuhn, and R. Muller. Phase field approximation of dynamic brittle fracture. *Comput. Mech.*, 54:1141–1161, 2014.

[218] J.J. Mason, J. Lamros, and A.J. Rosakis. The use of a coherent gradient sensor in dynamic mixed- mode fracture mechanics experiments. *J. Mech. Phys. Solids*, 40:641–661, 1992.

[219] F. Erdogan and G.C Sih. On the crack extension in plates under plane loading and transverse shear. *J. Basic Eng.*, 85D:519–527, 1963.

[220] Y. Lee and L.B. Freund. Fracture initiation due to asymetric impact loading of an edge cracked plate. *J. Appl. Mech*, 57:104–11, 1990.

[221] A.J. Rosakis, O. Samudrala, and D. Coker. Cracks faster than shear wave speed. *Science*, 284:1337–1340, 1999.

[222] P.H. Geubelle and D.V. Kubair. Intersonic crack propagation in homogeneous media under shear-dominated loading: numerical analysis. *J. Mech. Phys. Solids*, 49:571–587, 2001.

[223] A Bertram and J F Kalthoff. Fracture Toughness of fast propagating cracks in rocks. 2000.

[224] A. Bobet. The initiation of secondary cracks in compression. *Eng. Fract. Mech.*, 66:187–219, 2000.

[225] E.Z. Lajtai. Brittle fracture in compression. *Int. J. Fract.*, 10(4):525–536, 1974.

[226] A.R. Ingraffea and F.E. Heuze. Finite element models for rock fracture mechanics. *Int. J. Num. Anal. Met.*, 4:25–43, 1980.

[227] Kemney J. Chen, G. and S. Harpalani. Fracture propagation and coalescence in marble plates with pre-cut notches under compression. In *Symposium on Fractured and Jointed Rock Mass*, pages 443–448, 1992.

[228] J. Petit and M. Barquins. Can natural faults propagate under mode II conditions. *Tecnonics*, 7(6):1243–1256, 1988.

[229] O.M. Reyes. *Experimental study and analytical modeling of compressive fracture in brittle materials*. Doctoral of philosophy, Massachusetts Institute of Technology, 1991.

[230] H. Lee and S. Jeon. An experimental and numerical study of fracture coalescence in pre-cracked specimens under uniaxial compression. *Int. J. Solids Struct.*, 48:979–999, 2011.

[231] F.A. McClintock and J. Walsh. Friction of Griffith cracks in rock under pressure. In *Proceeding of the Fourth U.S Congress on Applied Mechanics*, pages 1015–1021. American Society of Mechanical Engineers, 1962.

[232] M.F. Ashby and S.D. Hallam (Née Cooksley). The failure of brittle solids containing small cracks under compressive stress states. *Acta Metall.*, 34(3):497–510, mar 1986.

[233] H. Li and Wong L.N.Y. Influence of flaw inclination angle and loading condition on crack initiation and propagation. *Int. J. Solids. Struc.*, pages 2482–2499, 2012.

[234] C.E Anderson, P.E.O Donoghue, J. Lankford, and J.D. Walker. Numerical simulations of SHPB experiments for the dynamic compressive strength and failure of ceramics. *Int. J. Fract.*, 55:193–208, 1992.

[235] H. Ramírez and C. Rubio-Gonzalez. Finite-element simulation of wave propagation and dispersion in Hopkinson bar test. *Mater. Des.*, 27(1):36–44, jan 2006.

[236] M. Sasso, G. Newaz, and D. Amodio. Material characterization at high strain rate by Hopkinson bar tests and finite element optimization. *Mater. Sci. Eng. A*, 487(1-2):289–300, jul 2008.

[237] B.A. Gama and J.W. Gillespie. Numerical Hopkinson Bar Analysis : Uni-Axial Stress and Planar Bar-Specimen Interface Conditions by Design. Technical Report September, Army Research Laboratory, 2004.

[238] M. Zhang, H.J. Wu, Q.M. Li, and F.L. Huang. Further investigation on the dynamic compressive strength enhancement of concrete-like materials based on split Hopkinson pressure bar tests. Part I: Experiments. *Int. J. Impact Eng.*, 36(12):1327–1334, 2009.

[239] D.J. Frew, M.J. Forrestal, and W. Chen. A Split Hopkinson Pressure Bar Technique to Determine Compressive Stress-strain Data for Rock Materials. *Exp. Mech.*, 41, 2000.

[240] D.J. Frew, M.J. Forrestal, and W.W. Chen. Pulse shaping techniques for testing brittle materials with a split Hopkinson pressure bar. *Exp. Mech.*, 42(1):93–106, 2002.

[241] G. Subhash and G. Ravichandrani. Split-Hopkinson Pressure Bar Testing of Ceramics.

[242] G.R. Johnson and W.H. Cook. Fracture characteristics of three metals subjected to various strain, strain rates, temperatures and pressures. *Eng. Fract. Mech.*, 21(I), 1985.

[243] B. Banerjee. An evaluation of plastic flow stress models for the simulation of high-temperature and high-strain-rate deformation of metals. 2005.

[244] J. Lankford. Temperature-strain rate dependance of compressive strength and damage mechanisms in aluminium oxide. *J. Mater. Sci.*, 16(6):1567–1578, jun 1981.

[245] J. Lankford. Mechanisms Responsible for Strain-Rate-Dependent Compressive Strength in Ceramic Materials. *J. Am. Ceram. Soc.*, (February):5–6, 1981.

[246] J. Kimberley, K.T. Ramesh, and N. P. Daphalapurkar. A scaling law for the dynamic strength of brittle solids. *Acta Mater.*, 61(9):3509–3521, 2013.

[247] J.M. Staehler, W.W. Predebon, B.J. Pletka, and G. Subhash. Micromechanisms of deformation in high-purity hot-pressed alumina. *Mater. Sci. Eng. A*, 291(1–2):37–45, 200.

[248] K.H Pham, K. Ravi-Chandar, and C.M. Landis. Experimental validation of a phase-field model for fracture. *Int. J. Fract.*, 205(1):83–101, 2017.

[249] D. Singh and D.K. Shetty. Fracture toughness of polycrystalline ceramics in combined mode I and mode II loading. *J. Am. Ceram. Soc.*, 72(1):78–84, 2017.

[250] C.M. Landis, T. Pardoen, and J.W. Hutchinson. Crack velocity dependent toughness in rate dependent materials. *Mech. Mater.*, 32:663–678, 2000.

[251] M. Strobl and T. Seelig. On constitutive assumption in phase field approaches to brittle fracture. *Proc. Struc. Integrity*, 2:3705–3712, 2016.

[252] E. Hoek and C.D. Martin. Francture initiation and propagation in an intact rock – A review. *J. Rock Mech. Geot. Eng.*, 6:287–300, 2014.

[253] W. Chen and G. Ravichandran. Failure mode transition in ceramics under dynamic multiaxial compression. *Int. J. Fract.*, 101:141–159, 2000.